Evaluation of NDT Technologies to Assess Presence and Extent of Delamination of HMA Airfield Pavements

Volume II: Supporting Information

March 2010

Center for Transportation Infrastructure Systems
The University of Texas at El Paso
El Paso, TX 79968
(915) 747-6925

Evaluation of NDT Technologies to Assess Presence and Extent of Delamination of HMA Airfield Pavements

Volume II: Supporting Information

by

Manuel Celaya, MSCE, EIT
Dante Mejía, BSCE
Selcan Ertem, MSCE
Soheil Nazarian, Ph.D., PE
Chetana Rao, Ph.D., PE
Harold Von Quintus, PE
Parisa Shokouhi, Ph.D.

DISCLAIMER

The contents of this report reflect the views of the authors, who are responsible for the facts and the accuracy of the data presented within. The contents do not necessarily reflect the official views and polices of the Federal Aviation Administration. The report does not constitute a standard, specification or regulation.

TABLE OF CONTENTS

LIST OF FIGURES

LIST OF TABLES

NDT METHODS FOR DELAMINATION DETECTION

Electromagnetic Methods

Ground Penetrating Radar

Ground Penetrating Radar (GPR) is a geophysical nondestructive technique that uses electromagnetic pulses to test, characterize, or detect subsurface materials based on changes in electrical and magnetic properties of the subsurface layers. Its first use can be traced in Austria in 1929. A typical equipment setup for typical GPR surveys is shown in Figure A.1 for air-launched and ground coupled systems. The setup typically includes a GPR Horn (air-launched) or ground antenna together with a survey wheel and a GPS unit for measuring distance and recording the location of test survey lines.

Figure A.1 – Equipment Setup for Air Launched (Left) and Ground Coupled (Right) GPR

Units

GPR works using short electromagnetic pulses radiated by an antenna which transmits these pulses and receives reflected returns from the pavement layers, as shown in Figure A.2a. The reflected pulses are received by the antenna and recorded as a waveform, as shown in Figure A.2b. As the equipment travels along the pavement, it generates a sequence of waveforms as

shown in Figure A.2c. These waveforms are digitized and interpreted by computing the amplitude and arrival times from each main reflection. The reflections of these waves at interfaces and objects within the material are analyzed to determine the location or depth of these interfaces and buried objects, and to determine the properties of material. Whenever applicable, GPR can be employed as a rapid nondestructive tool for evaluation of geometrical and material properties of structural components. Unfortunately, claims about the capability of the technology have sometimes been overstated, leading to unrealistic expectations and disappointment in the results (Maser 1996). The main advantage of the GPR is the speed of the operation and almost full-coverage of the airfield. Some of the traditional limitations of GPR have been the cost and complexity of the equipment, the need for interpretive expertise, and the requirement for office data processing. However, recent developments with GPR hardware have yielded systems which are less expensive and easier to operate, and could overcome the equipment complication. On the data processing side, prototype software for automated on-site processing has been developed (Maser et al., 2002) which may overcome some of the processing issues.
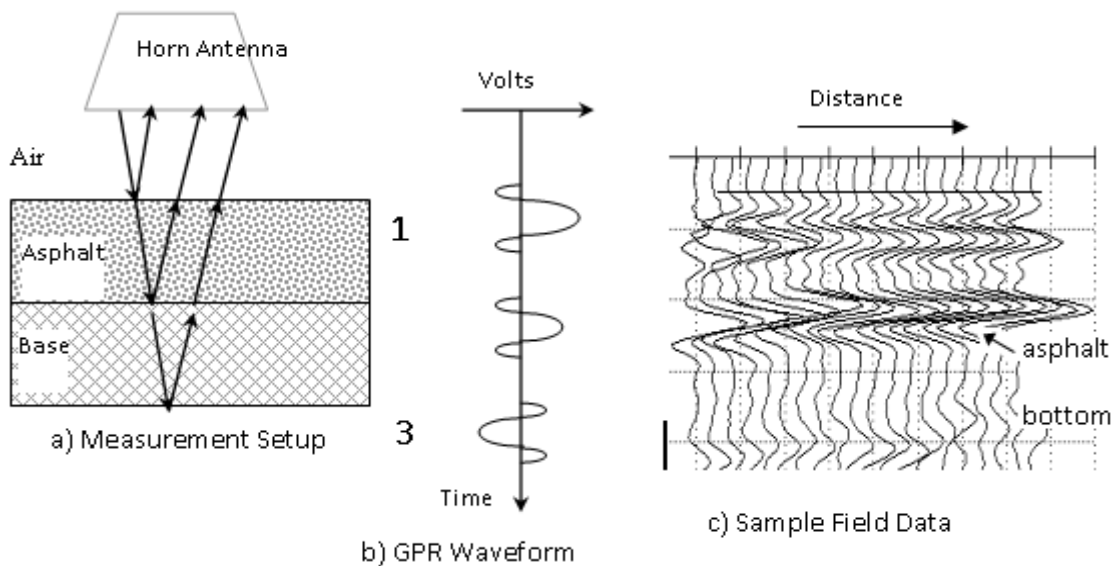
Figure A.2 – Principle of GPR for Pavement Layer Thickness Evaluation

2

GPR has been extensively used for measuring pavement layer thicknesses (ASTM D4748), locating changes and anomalies in pavement structures, detecting voids under concrete slabs, locating reinforcement and dowels in jointed concrete pavements, and moisture damage (stripping) in asphalt pavements. GPR technology has proven effective in detecting layer thicknesses and identifying areas where non-uniform electromagnetic properties indicate changes in physical properties such as moisture damage, stripping, or other subsurface anomalies (Hammonds et al., 2005). For example, a combination of GPR survey of the roadway followed by seismic tests in selected areas and validation with ground truth data has been successfully used to identify areas with various levels of moisture damage, stripping or other forms of distress.

However, the application of GPR in detection of delamination may require further evaluation. To directly detect the delamination, the reflections from the top and bottom surfaces of the delaminated area should be distinguishable in GPR radagrams. Even at 1 GHz the GPR wavelength in construction material (concrete or HMA) is much too long to resolve the 1-2 mm wide delamination cracks (Maser, 1996). As such, the direct detection of the onset of delamination may be difficult. As the delamination-induced debonding grows, it maybe more likely to be detectable by a GPR. The changes in GPR waveforms as a result of separation (air-filled or water-filled) between HMA layers have been investigated in a multi-phase theoretical, experimental, and field study (Smith and Scullion, 1993). They developed a theoretical model to describe the changes in the input pulse as it travels through the pavement layer system and reflects at each interface. The model incorporated a linear-mixture model, in which the dielectric constant of a mixture was taken as the summation of the dielectric constants of its constituents

3

weighted by the corresponding volumetric ratios. The dielectric constant of the asphalt mixture (ε_{ac}) can be expressed as follows:

$$\varepsilon_{ac} = \varepsilon_s \, V_s + \varepsilon_{as} \, V_{as} + \varepsilon_a \, V_a \tag{A.1}$$

where ε_{ac} is the dielectric constant of the asphalt mixture, ε_s, ε_{as}, ε_a are the dielectric constants of the aggregate, asphalt, and air, respectively, *and V_s, V_{as}, V_a* denote the volumetric ratios of aggregate, asphalt, and air, respectively. Assuming layer thicknesses, dielectric constants, and mix characteristics, the radar traces were modeled to simulate the radar response to the pavement distresses of interest. Changes in the dielectric constants were shown to affect both the amplitude and the travel time of the reflected signals. For example, the simulated reflections as a result of an air gap in asphalt are depicted in Figure A.3 as the gap thickness was increased from 0.1 to 2.0 cm. As the gap grows thicker, both shape and amplitude of the reflected waves change. Similar results were obtained when the gap was assumed to be filled with water, but the changes in the signal were more significant due to the high dielectric constant of water. The reflection coefficient versus the gap thickness for the air and water filled gaps are shown in Figure A.4. The simulated results were compared to real-world data and a good agreement was reported.

a) Gap thickness : 0.1 cm

b) Gap thikness: 0.2 cm

c) Gap thickness: 0.6 cm

d) Gap thickness: 2.0 cm
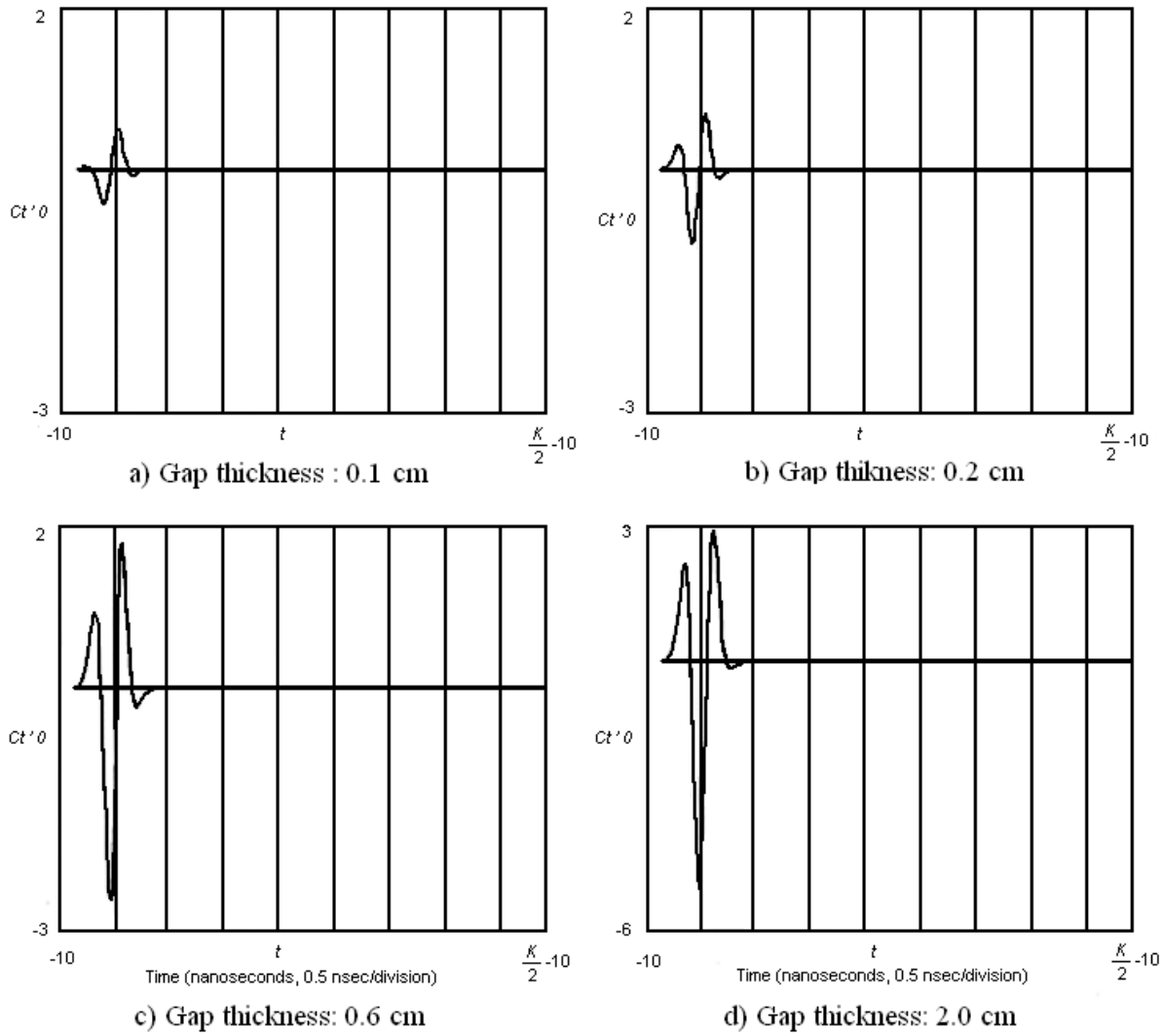
Figure A.3 – Reflections Due to Air-filled Delamination in Asphalt (Smith and Scullion, 1993)

5
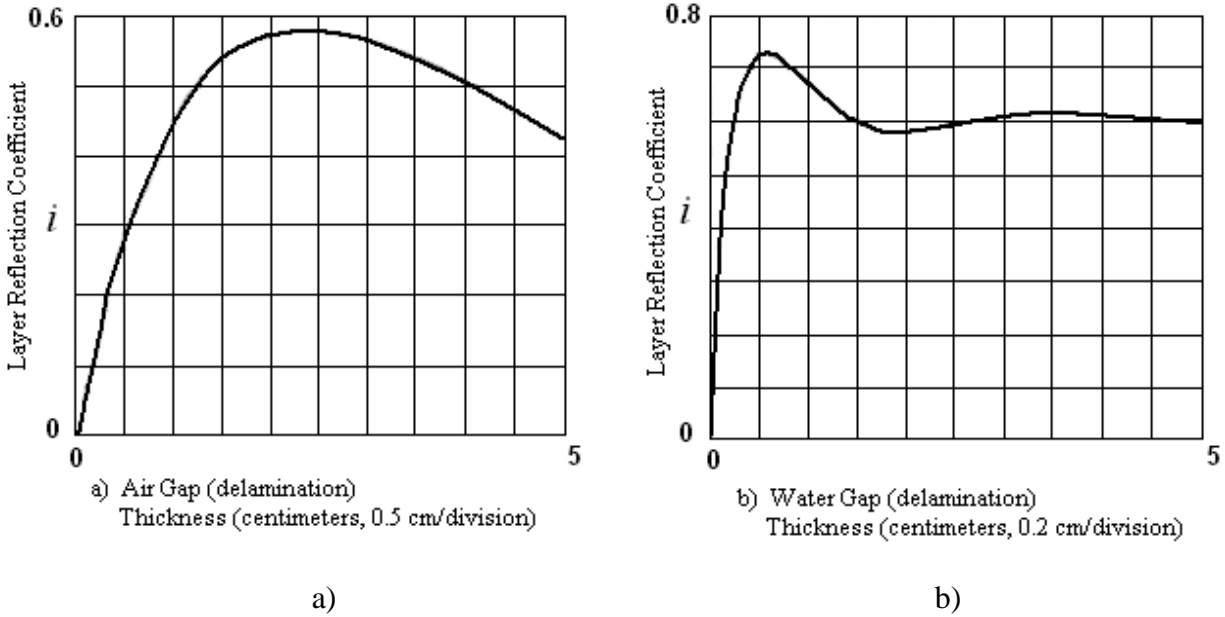
Figure A.4 – Reflection Coefficient Due to Air-filled and Water-filled Delamination (from

Smith and Scullion, 1993)

Based on the results of that study, air-filled delamination of 0.5 cm (0.2 in.) or larger at a minimum depth of 5 cm (2 in.) and water-filled delamination of 0.25 cm (0.1 in.) or larger at a minimum depth of 5 cm (2 in.) may be detected by a 2.5-GHz horn antenna. The above tentative guidelines are valid when a dual 1 and 2.5-GHz antenna system is used provided that the maximum data acquisition speed does not exceed 10 mph.

As a part of that study, several field test sections were evaluated using the GPR. The laboratory and field tests did produce promising results. GPR proved to be useful for estimating the layer thicknesses, the moisture content of flexible base course, and the presence of moisture-filled voids. However, in that field testing, the potential of GPR to detect air-filled voids, overlay delamination and stripping in the asphalt could not be fully evaluated and it was recommended that more testing was necessary (Smith and Scullion, 1993).

Other field investigations have reported that GPR survey can provide useful information which may indicate delamination between asphalt layers. For example, the much larger

6

amplitudes in GPR radargram shown in Figure A.5 mark the location of delaminated zones. This observation was confirmed by the core taken at the perceived location of delamination (GBG Australia).

Based on the available literature, detection of delamination between HMA lifts, especially at its early stage of development, is highly challenging and demands further systematic investigation. More likely, the successful results may be achieved indirectly by using the technology to measure the condition that is associated with the presence or development of delamination in HMA. For example, given the high sensitivity of GPR signals to the changes in moisture, the penetration of moisture within the delaminated region may be detected and assist in identifying delamination. However, the identification of emulsion-rich interfaces from the wet interfaces may be also difficult (Maser, 1996). A combination of GPR with other NDT technique(s) which provide a direct method of detection of delamination may yield the best outcome.
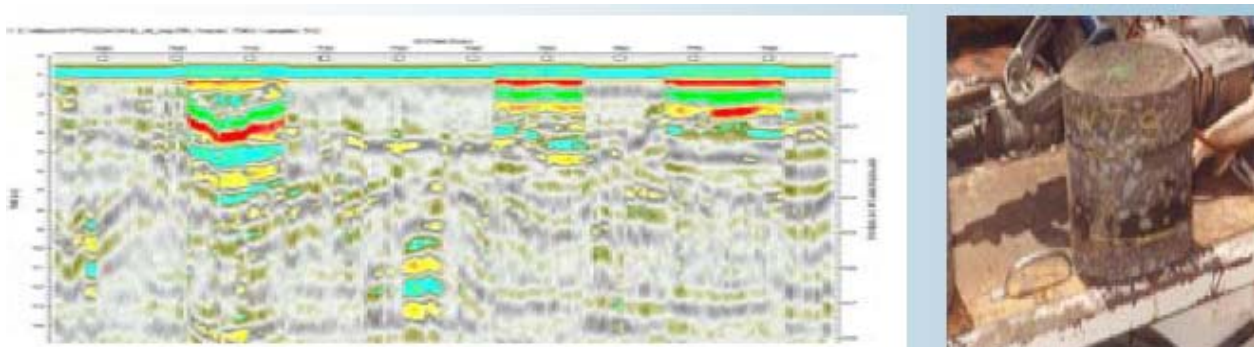
Figure A.5 – Radar Profile and Core Retrieved Showing Asphalt Delamination (GBG Australia)

Impulse Methods

The impulse methods work on the principle of measuring the pavement response (deflection) to a known load. Theoretically, if delamination occurs within an HMA layer, the

deflection of the pavement system should increase. As such, the impulse methods may be utilized in relative terms to detect the delamination. The Falling Weight Deflectometer (FWD), the Light-Weight Deflectometer (LWD) and the Impulse Response method are examples of impulse methods. The potential application of these techniques in detection of interlayer delamination is described below.

Falling Weight Deflectometer (FWD)

The FWD device consists of an impact loading mechanism and a set of sensors to measure vertical surface displacements at the load location and at specified offsets from the load. The loading component delivers a transient load to the pavement surface and the sensors measure the surface deflection at the specified locations. The entire system is typically trailer mounted as shown in Figure A.6. The loading device consists of a load plate that can apply an impulse load of different magnitudes ranging from1500 to 27000 lb. The load can be applied from standard drop heights resulting in a load pulse of 25 to 60 msec. The load plate is circular and has a standard diameter of 6 in.

Figure A.6 – Trailer Mounted FWD

The pavement response to the applied load in terms of a deflection basin is measured at several radial locations, as shown in Figure A.7. Estimating the best set of pavement properties to fit the measured deflections is then carried out in a process known as backcalculation. The FWD backcalculation results are in-situ effective stiffness of the bituminous layers at the site temperature. Higher deflections are expected if poor bond exists, since the layers will act independently in the absence of shear continuity at the interfaces. In such cases, lower stiffness is usually obtained from FWD test results. Therefore, the FWD backcalculated stiffness may provide some indications of poor bonding between HMA layers.
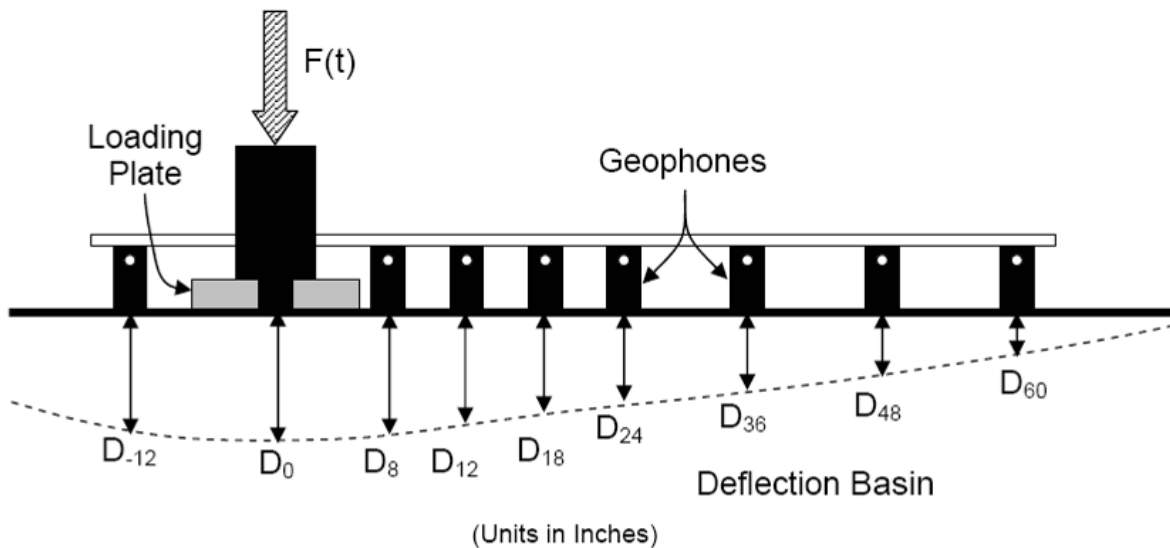
Figure A.7 – Typical Deflection Basin Measured From FWD

Earlier studies concluded that deflection measurements devices such as deflect graph and FWD were not found promising for assessing interface debonding condition (Lepert et al., 1992). A new backcalculation process for assessing the bond condition between the HMA layers using FWD deflections has shown some promise (Al Hakim et al., 1997, 1998, 2000). This new algorithm involves the calculation of an additional parameter called "shear reaction modulus" or K_s from the deflection basin that provides an indication of the bond condition over a relatively

large area. To calculate K_s, the interface between two pavement layers is assumed as a thin layer with a shear modulus G and a thickness t. The shear stress τ at the interface can be expressed as:

$$\tau = (G/t) \cdot \gamma = K_s \cdot \Delta u \qquad\qquad (A.2)$$

where γ is the shear strain of the thin interface material, Δu is the relative horizontal displacement between the two sides of the interface and K_s is the shear bonding stiffness or shear reaction modulus at the interface.

Al Hakim et al. (2000) performed a sensitivity analysis to investigate the theoretical influence of bonding stiffness on surface deflections and backcalculated layer stiffness in multilayer pavement systems. During the backcalculation process, the interface bond stiffness was considered as a variable and was backcalculated similar to a layer stiffness. First, a constant bond stiffness of 1000 MN/m^3 between layers was assumed and then, the HMA layer stiffness was slightly adjusted. Finally, the bond stiffness between layers (K_s) varied from complete de-bonding (10 MN/m^3) to full adhesion (10^5 MN/m^3) to find the optimum fit for the deflection basin. To calibrate and verify the proposed theoretical method, FWD was used on several newly-constructed pavements to estimate bonding stiffness. Tests were conducted before sections were opened to traffic and repeated after six months. It was found that a combination of traffic loading and higher temperature during testing improved the bonding between layers. However, sections with very poor bond did not improve with traffic or time. The backcalculated interface stiffness from FWD deflection basis was found not to be successful for assessment of bond condition between thin layers of asphalt (Al Hakim et al., 1997; Kruntcheva et al., 2005).

FWD measurements have also been used to detect debonding between lifts of airport pavements (Gomba, 2004). Data obtained from the Federal Aviation Administration's (FAA) National Airport Pavement Test Facility in Atlantic City, New Jersey, was used to measure

interlayer bonding for pavement sections that had encountered a loss of bond between lifts of the surface HMA. It was found that the calculated stiffness moduli for surface layers could be used as a parameter to determine the quality of interlayer bonding. A parameter called "Tack Coat Failure Ratio" (TFR) was defined and it was attributed to the slippage susceptibility at the interface. TFR was defined as the ratio of the moduli of the HMA layers above and below the debonded interface as backcalculated form FWD results. Therefore, TFR is 1 for a bonded interface, and is 0 when the interface is debonded. Another parameter called 'Effect of Slip' in the pavement which was defined as the ratio of the difference in radial stress (between points just above and below the interface) to the maximum difference in radial stress at the interface at full slip. It was found that TFR is well correlated to the Effective Slip (see Figure A.8). It was concluded that surface layer moduli calculated from FWD data can be used to identify a lack of interlayer bonding in pavements and that the effect of slip between two asphalt layers of similar properties will be reflected by the moduli of the top layer being lower than the moduli of the bottom layer (Gomba, 2004).
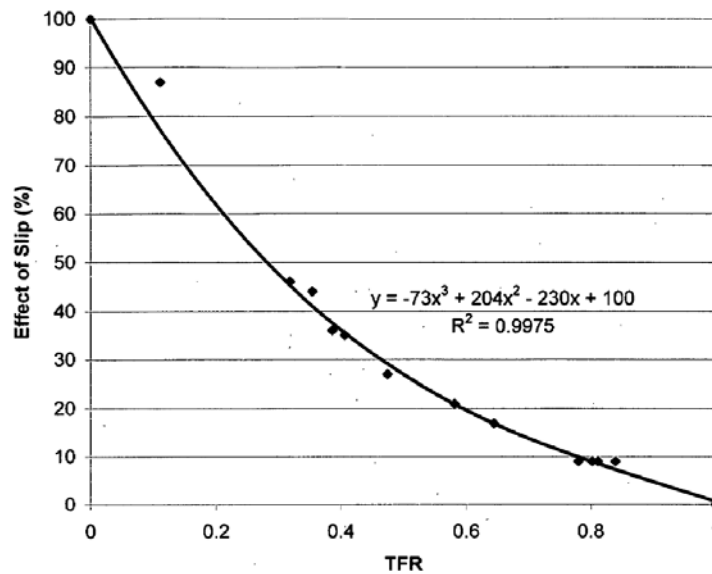
Figure A.8 – Effect of Slip/TFR Correlation (Gomba, 2004)

The chart shows a plot of Effect of Slip (%) on the y-axis versus TFR on the x-axis, with the equation $y = -73x^3 + 204x^2 - 230x + 100$ and $R^2 = 0.9975$.

A forward calculation technique was utilized to calculate the bond stiffness from the FWD deflection basin using closed-form solutions (Hammonds et al., 2005). This technique assumes that the bond modulus is primarily a function of the near-load deflections as described by the radius of curvature of the deflection basin. Because the resulting surface course stiffness is independent of the moduli of other layers within the pavement system, a unique solution is obtained. However, because the surface course stiffness is calculated independently of the other layers in the pavement structure, the values obtained may or may not be reasonable with respect to the total center deflection.

Some approaches have been carried out based on the "AREA" concept (a deflection basin curvature index), that calculates the overall composite modulus of the entire pavement structure (Hammonds et al., 2005). Using the logic of the AREA concept, the stiffness of the bound HMA layer can be given by:

$$E_{AC} = \frac{E_0 \cdot AF_{AC} \cdot k_3^{1/AF_{AC}}}{k_3^2} \tag{A.3}$$

where E_{AC} = stiffness or modulus of the upper HMA layer(s), k_3 = thickness ratio of upper layer thickness / load plate diameter = $h1 / (2a)$, E_0 = composite modulus of the entire pavement system beneath the load plate, and AF_{AC} = AREA factor.

Equation A.3 has been calibrated using a large number of trial elastic layer theory calculations, and it works well for typical materials and modular ratios. Nevertheless, this approach is not totally rigorous or scientific, but rather is empirical in nature. The approach can therefore be used effectively to approximate the relative stiffness of the uppermost layer(s) in a pavement cross section for comparative purposes.

Light Weight Deflectometer (LWD)

The LWD operates in a similar fashion to the FWD with one to three sensors (as opposed to at least seven for FWD); however such a device is generally small and light enough to be carried and operated by one person, as shown in Figure A.9 and is mainly used on unbound materials, where lighter loads are required. The analysis methods described for FWD are also applicable to LWD. After an extensive review of the literature, no study could be found where the application of LWD for detection of delamination between HMA layers was evaluated.

Impulse Response Method

The basic operating principle of the impulse response hammer is to apply an impulsive loading to the pavement surface with the hammer and measure the vertical dynamic response using an accelerometer (Sangiorgi et al., 2003). If structural distresses are present in the form of loss of adhesion between pavement layers, this is reflected in the dynamic response of the pavement structure. The equipment necessary to complete the test is shown in Figure A.10.

Figure A.9 – Light Weight Deflectometer
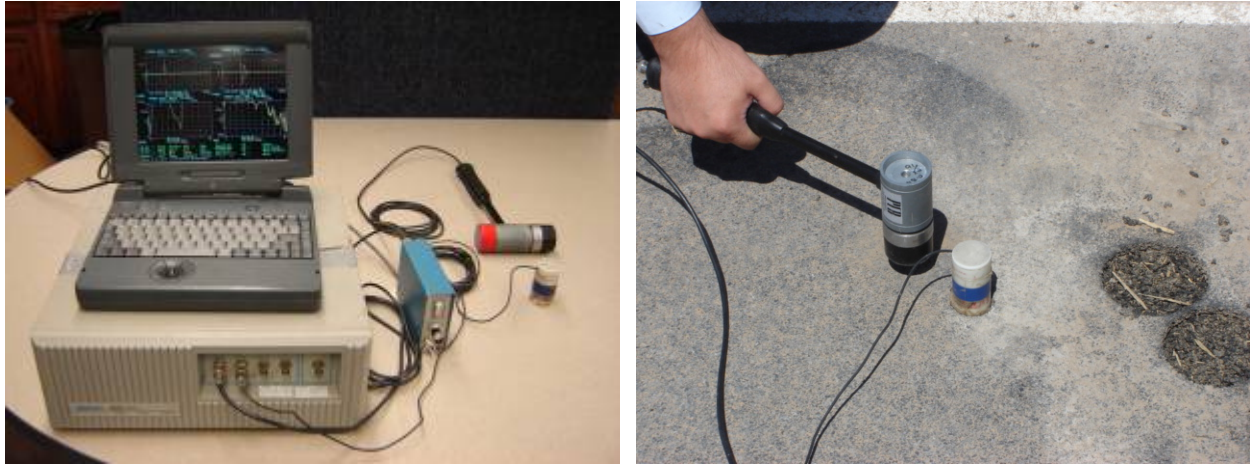
Figure A.10 – Impulse Hammer Test Setup

This method uses a low-strain impact to initiate stress wave propagation through the material under investigation. The response to the impact is measured and analyzed to assess the in-situ condition. The impactor is usually a 2 to 10 lb instrumented hammer. The response is normally measured by a velocity transducer (e.g. geophones) or accelerometer. Both the hammer and the receiver are linked to a portable field computer for data acquisition and storage. The data analysis can be completed in the field and typically includes the calculation of transfer function or mobility by dividing the frequency spectrum of response by that of the input force. The characteristics of the time history of the response as well as the shape of the graph of mobility plotted against frequency contain information about the condition and the integrity of the material under test. An example of two mobility plots obtained on a sound and delaminated slab is shown in Figure A.11. More quantitative assessment is possible by comparing the mobility plots through different calculated parameters such as (CTL, www.ctlgroup.com):

- Dynamic Stiffness

- Mobility and Damping

- Peak/Mean Mobility Ratio

The Impulse Response test has several advantages over most other nondestructive testing methods including the robust nature of the apparatus, the speed of data collection and analysis, the repeatability of test results, and its applicability on relatively rough surfaces (CTL, www.ctlgroup.com).

Kruntcheva et al. (2004) studied the feasibility of using IR method for quantifying bond condition within HMA layers under controlled laboratory condition. Different surfacing thicknesses were considered and the following interface conditions were compared: bonded; debonded; and partially bonded. Results showed that the vibration differences between bonded and debonded surfacing are force-amplitude dependent. To investigate the repeatability of the results, five input-output time histories were recorded at each particular position of the receivers.
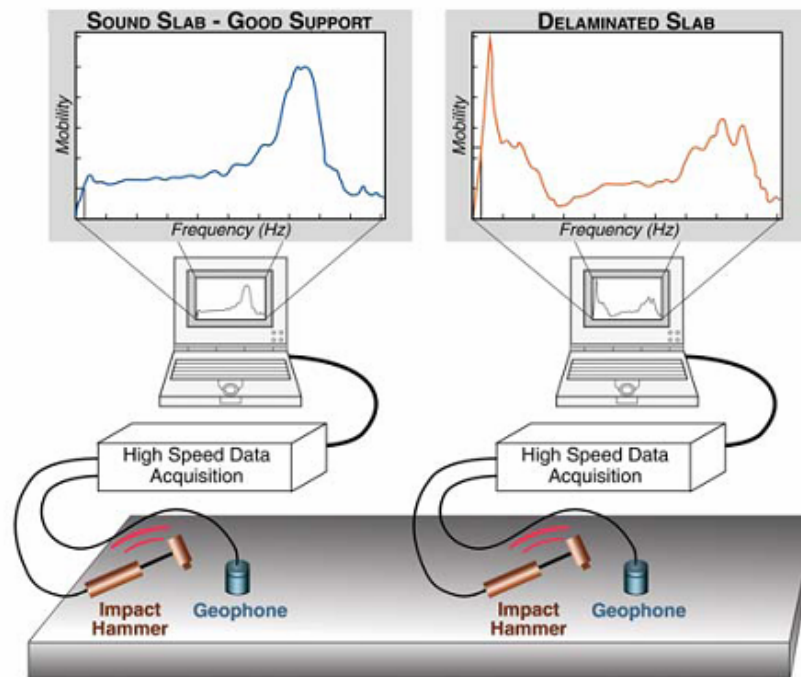
Figure A.11 – Example of IRH Signals for Intact and Delaminated Slabs (CTL, www.ctlgroup.com)

15

The differences in dynamic responses of the debonded and bonded interfaces are shown in Figure A.12. The bonded system reacts to impulse applied by transmitting displacement wave components of low frequency, whereas the debonded surfacing starts vibrating. This effect can also be recognized by the oscillatory components of the response, which were out of phase with respect to the excitation. Furthermore, the after-impact behavior of the debonded surfacing is clearly oscillatory, indicating a predominant forced damped vibrations with much longer decay time in comparison with the ''wave'' response of the bonded case. Therefore, the visual inspection the time histories provides a qualitative indicator of bond condition between HMA layers.
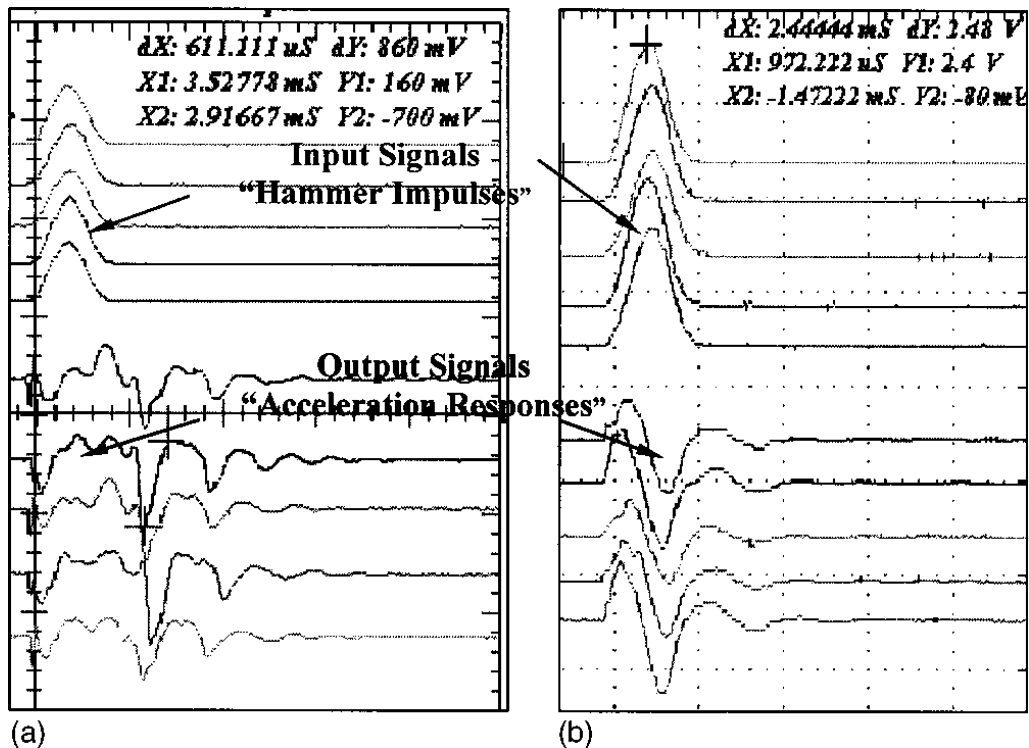
Figure A.12 – Time Histories of Input and Output Signals for Debonded (a) and Bonded (b) Surfacing (Kruntcheva et al., 2004)

For a more quantitative assessment, the input-output transfer function estimate (TFE) was obtained from the spectral analysis. The equations that relate the spectral density of the excitation and the response of a system undergoing random vibration are:

$$H(\omega) = \sqrt{\frac{S_{xx}(\omega)}{S_{yy}(\omega)}} \qquad (A.4)$$

where $H(\omega)$ is the transfer function estimate (TFE) linking the quantities $S_{xx}(\omega)$ and $S_{yy}(\omega)$ which are the autospectra of the excitation and the response signals, respectively.

The magnitudes of the TFE's for the bonded and debonded cases for a shallow interface are compared in Figure A.13. The maximum amplitudes in both cases occur at a frequency between 1 and 2 kHz but the TFE magnitude for the debonded interface is 10 times larger than the bonded one. The enhanced dynamic response of debonded or partially bonded surfacing to hammer impulse is due to vibrations of the upper pavement layer rather than wave reflection. Therefore, a large increase in this parameter, more than five times relative to the TFE magnitude for bonded surfacing, indicates partial to very poor bond at the interface provided that the other surfacing parameters such as material and thickness remain unchanged. For shallow interfaces 20 to 50 mm a normalized maximum TFE magnitude over 15 was noted as very poor bond or no bond at the uppermost interface.

Similar results were obtained for deeper cases of delamination, but with a shift in the frequency at which the maximum value of TFE occurred. The deeper the surfacing, the higher was the frequency associated with the maximum TFE. For debonding at depth of about 1 in., the maximum TFE occurred around 3.5 kHz and for debonding at a depth of about 2 in., this value

17

was close to 5 kHz. This observation may be used as an approximate indicator for the surfacing

thickness, but more extensive research is needed to confirm this finding
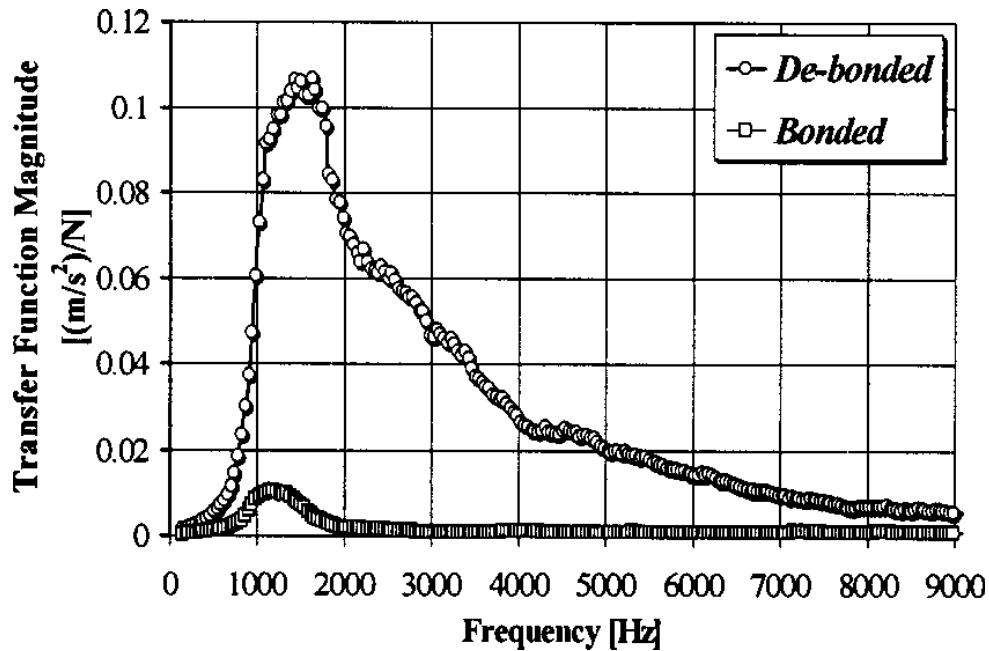
Figure A.13 – Magnitude of TFE versus Frequency for Bonded and Debonded Surfacing

(Kruntcheva et al., 2004)

The IR method was used for the in-situ assessment of bond condition between surface

and base courses for different types of surface course in another study (Sangiorgi et al., 2003).

Two sections with different materials and thicknesses were tested in December and May. One

section was overlaid with an about 1 in.-thick and the other section was overlaid with a 1.25 in.

layer.   Each section was divided into three sub-sections, each one with a different surface

treatment to achieve different levels of bond at the interface.   This included application of a

normal amount of tack coat, a swept surface with no tack coat, and clay slurry applied to the base

layer. Typical time histories for two case of intact and debonded interfaces obtained from this

study are shown in Figure A.14. Visual inspection of the records yielded similar conclusions to

those reported by Kruntcheva et al. (2004). The response of the debonded system contains

18

vibrations of higher frequencies (greater than 1 kHz) and the acceleration does not decay to zero until approximately 6 ms, because of the vibrations induced in the surface layer due to lack of bonding to the layer below. On the contrary, the acceleration history of the bonded system is of lower frequency and is heavily damped and decays to zero after approximately 1.5 ms).

A different data analysis approach based on the fractal theory was used to obtain a quantitative indicator of bond conditions. A fractal is an object with an infinite nesting of sub-structures at different scales. It is possible to apply the fractal theory to "non-mathematically" fractal objects such as time histories and calculate a unique characteristic parameter called fractal dimension (FD) which is a single number between 1 and 2. An elementary technique for determining the F.D. is known as "Box Counting", as shown in Figure A.15. The procedure to determine the F.D. for each measured acceleration time history is a follows. An initial square box dimension (L_{init}) is chosen and the number (N) of boxes required to fully cover the complete signal is determined. In the following step (i) the box dimension is reduced ($L_{(i)}$) and the number of new (smaller) boxes required to fully cover the complete signal is re-calculated. The procedure is repeated for proportionately smaller box dimensions in the next steps. The number of boxes (N) is then plotted against (s), the ratio between the initial box dimension (L_{init}) and the box dimension at each (i) step ($L_{(i)}$) on double logarithmic scales. A straight line is then fitted to the data and the gradient of the line is the F.D. Figures A.15 and A.16 show how the Fractal Dimension is deducted from the log(N)-log(s) graph for a classical Koch fractal curve and for a measured accelerometer time history recorded from a well bonded section of the trial pavement. This analysis was applied to the recorded acceleration histories and an average FD at each test point was calculated. The calculated FDs ranged from approximately 1.1 for well bonded areas to about 1.3 for debonded areas. It was also found that the average bond condition improved in
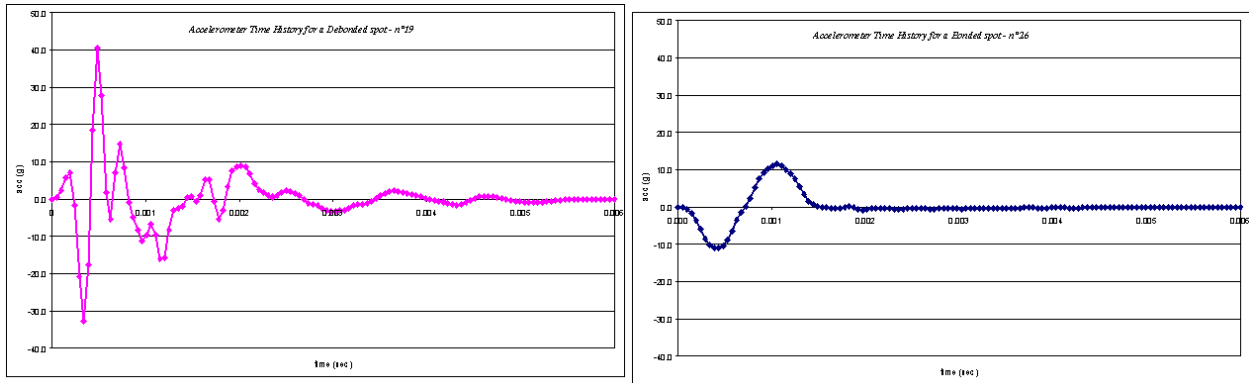
a)   b)

Figure A.14 – Typical Debonded (Left) and Bonded (Right) Time Histories (Sangiorgi et al., 2003)
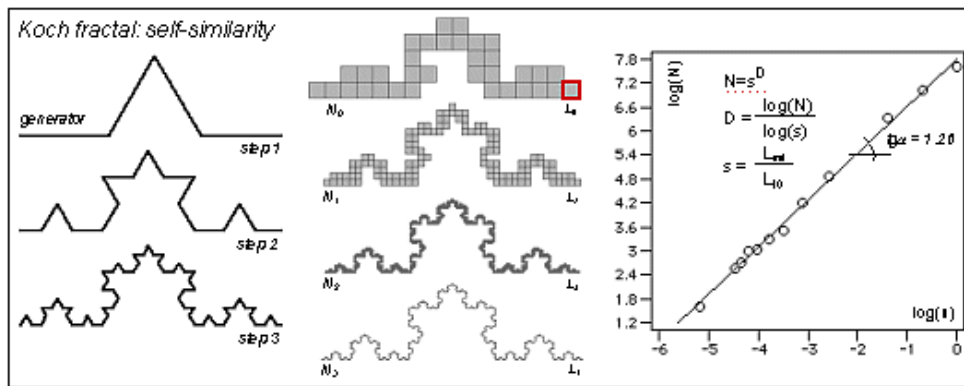
Figure A.15 – Box Counting Fractal Dimension

N	log(s)	log(N)
1	0.000	0.000
2	0.301	0.301
4	0.602	0.602
11	0.903	1.041
26	1.204	1.415
53	1.505	1.724
110	1.806	2.041
228	2.107	2.358
429	2.408	2.632
737	2.709	2.867
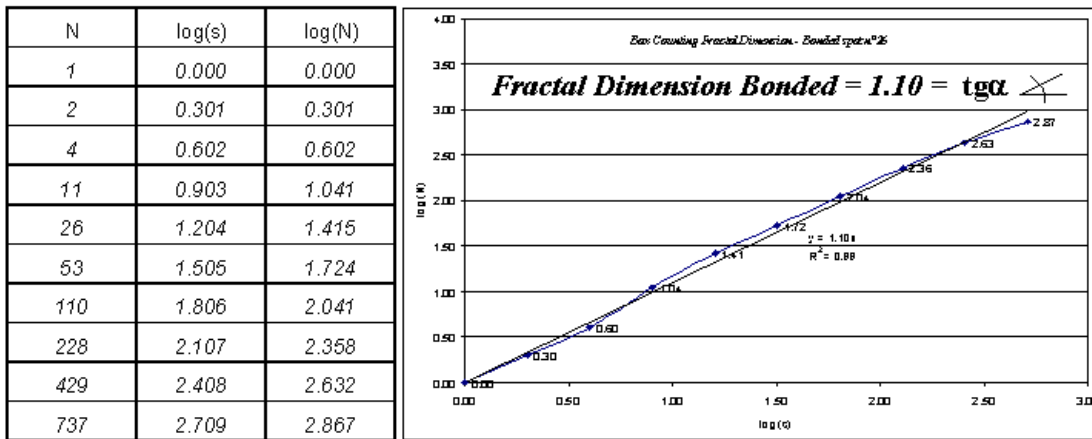
Figure A.16 – Box Counting Fractal Dimension for a Bonded Location

May relative to December, which was attributed to the bitumen healing characteristics at elevated temperatures.

The IR method seems to be a reliable quantitative and qualitative tool to obtain information about the interface bond. The surfacing material and thickness are expected to affect the test results. Therefore, when pavement test sections are of similar material, the results should be always considered relative to the response of an area that is known to be bonded. It should be noted that most of the conclusions cited above are based on the controlled laboratory studies rather than field investigations. More extensive research is needed to verify the applicability of the IR method for assessing the bond condition between HMA lifts.

Vibration Methods

Stiffness Gauge

Soil Stiffness Gauge (SSG) (Figure A.17), which is currently marketed as the Humboldt GeoGauge^{TM}, is a recently developed instrument for directly measuring in situ stiffness of soils. The SSG was conceived and developed partially by funding from FHWA in partnership with

Figure A.17 – Soil Stiffness Gauge (SSG) or GeoGauge^{TM}

several private firms. The SSG is a 11 inches in diameter and 10 inches in height portable cylinder with a 4.5 in-outer diameter and 3.5 in-inner diameter ring-shaped foot extending from the bottom of the device and it weighs approximately 22 lbs.

In vibratory methods, the pavement is vibrated using controlled input frequencies. The Stiffness Gauge developed for quality control of the granular layers, is an example of such devices. The stiffness gauge vibrates the material in the range of frequencies of 100 Hz to 200 Hz using very small load amplitudes. The variation in stiffness (displacement/load) with frequency (called stiffness spectrum) is used to measure the modulus of the material. For the detection of delamination, the stiffness spectrum can be reinterpreted (similar to impulse-response) to assess the bond quality. Since the stiffness gauge is optimized for low-stiffness geo-materials, neither the force level nor the frequency range seems adequate. The coupling of the ring that imparts load to the pavement to HMA seems problematic too. The lightweight vibrator has proven ineffective when used in a controlled experimental study on a number of special test sections in France to detect different interface conditions (Lepert et al., 1992).

High Frequency Sweep

An alternative vibratory device is a high-frequency, hand-held electromagnetic/piezoelectric shaker developed for military applications by Wilcoxon Research, as shown in Figure A.18, which can be used to impart steady state swept vibration at high-frequencies (several kilohertz) and at high energy (horizontal, vertical or at an angle).

This piezoelectric shaker utilizes piezoelectric ceramic disks, which change thickness proportional to an applied voltage. These disks are sandwiched between a heavy mass and a light fixture, which attaches to the test structure. Although the displacement is very small, the use
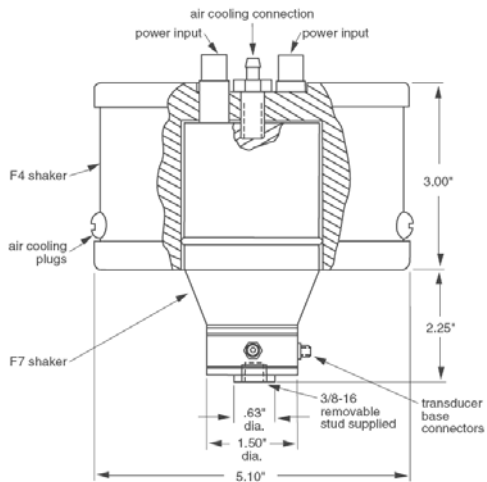
Figure A.18 – Electromagnetic/Piezoelectric Shaker System

of multiple disks and high drive voltages can produce large forces at high frequencies. The high-intensity, high-frequency vibration primarily excites the pavement layer atop the delaminated layer. Such vibrations can be detected by the built-in accelerometer of the shaker, a typical output is shown in Figure A.19. The stiffness spectra from this device can be readily used to detect the delaminated layer similar to the IR method.
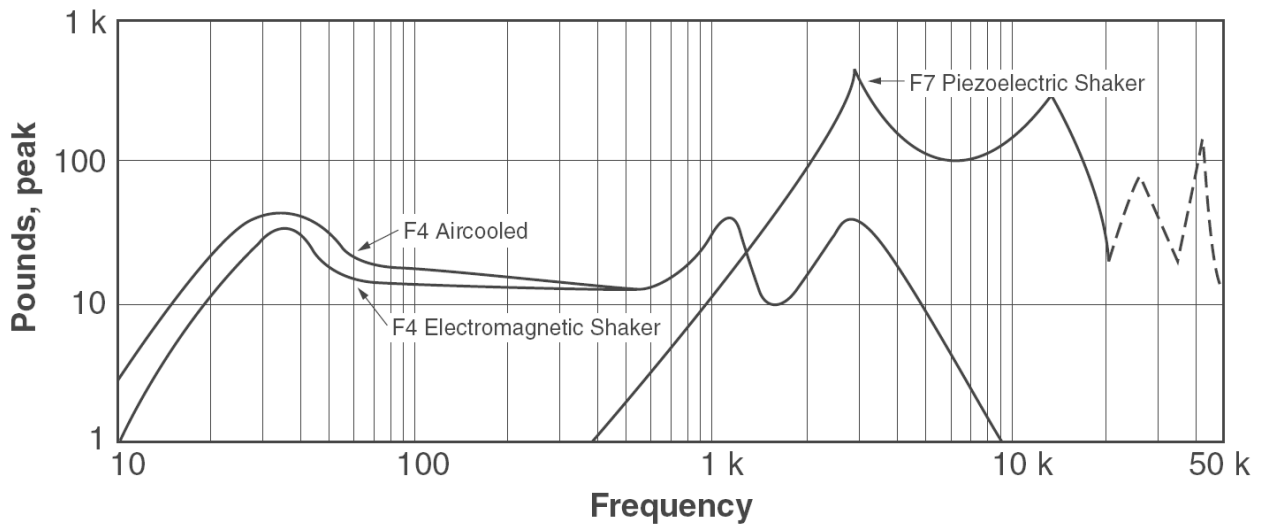
Figure A.19 – Typical Blocked Forced Output

Sonic/Ultrasonic Seismic Methods

Seismic sonic/ultrasonic methods rely on the principles of elastic wave propagation for material characterization and/or defect detection. When the surface of a material is impacted with a point source, several types of elastic waves propagate in that material. These waves can be categorized into two broad groups: body waves and surface waves. Body waves include compression waves (a.k.a. P-waves) or shear waves (a.k.a. S-waves) which propagate along a spherical front within the material. Surface waves (a.k.a. Rayleigh waves, R-waves), on the contrary, propagate along a cylindrical front. Surface waves, which carry about two-thirds of the seismic energy generated within a layer, are of higher amplitudes and attenuate at a lower rate than body waves. A concise but extended description of elastic wave propagation within a material can be found in (Nazarian et al., 1993).

Among seismic methods, the Impact-Echo (IE) and Spectral Analysis of Surface Waves (SASW) or its ultrasonic version, USW, has been successfully used for direct or indirect assessment of the bonding condition between HMA layers. IE test is based on identifying body-wave reflections in the surface response. SASW (or USW) use the changes in surface wave dispersion characteristics or elastic properties as an indication of poor bonding. Ultrasonic testing has been long used for evaluation of concrete. With the recent advances in the testing equipment and data analysis, the application of this technique to defect detection in HMA may become possible. A concise overview of these methods along with their potential applications in detection of delamination in HMA is given below.

Impact Echo

The Impact echo (IE) method involves the application of an impact (of sonic to ultrasonic frequency) and detecting reflections from interfaces of materials with dissimilar elastic

24

properties (e.g. contrast in impedance). The principal components of an impact echo system are a transducer, a set of spherical impactors, a data acquisition system, and a computer with the appropriate software to analyze the data acquired, a typical IE test system is shown in Figure A.20. The IE method is based on detecting the resonance frequency of the standing wave reflecting from the bottom and the top of the topmost pavement layer, as sketched in Figure A.21.

Figure A.20 – Typical Impact Echo Test System
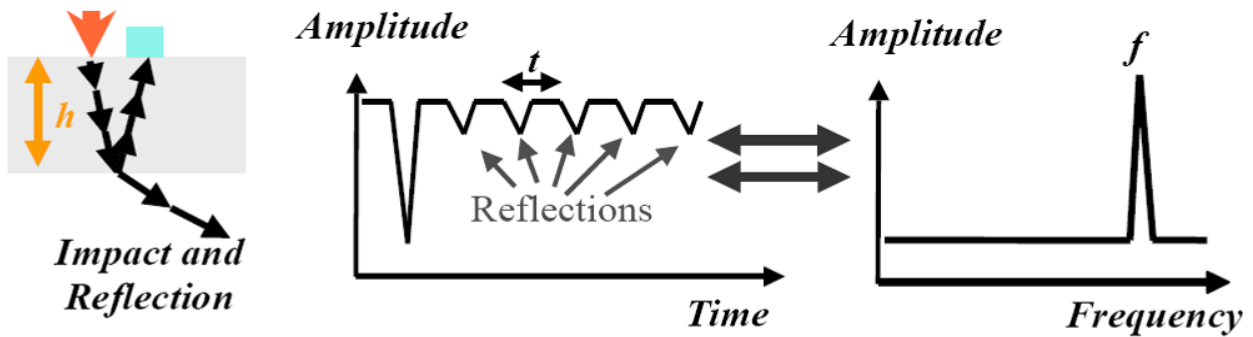
Figure A.21 – Schematic of Impact Echo Method

Upon the application of the impact on the surface of pavement, a part of the source energy is reflected from the topmost interface while some is transmitted into the base and subgrade. If a delamination exists within the top layer, a great portion of the energy is reflected from delamination. The resonance frequencies associated with the reflected waves from various

interfaces within a pavement system can be distinguished in the IE amplitude spectrum, the frequency spectrum of IE record. Knowing the compression wave velocity of the layer (*Vp*) the depth-to-reflector, *h*, can be determined from:

$$h = \frac{V_P}{2f}$$
(A.5)

where *f* is the resonant frequency associated with the reflector at a depth h.

The IE method was originally developed to evaluate thickness and locate defects, voids, cracks, and zones of deterioration within concrete structures (Sansalone and Carino, 1986). The method has been used for evaluation of both concrete and asphalt pavements as well as for detection of debonding beneath asphalt overlays (Lin and Sansalone, 1996). While is not possible to estimate the bond strength, the IE method may determine whether there is extensive porosity at the interface (Carino, 2001). A discontinuity within the top pavement layer due to delamination would reflect all the energy imparted to the pavement resulting in the detection of the depth to interface of the delaminated layer. Available IE devices can be used to detect the delaminated interfaces deeper than 4 in. (Armitage et al., 2000). Shallower delaminated areas can be still identified using IE (from the large amplitude low frequency signals); however, no information regarding the depth to the delamination layer can be drawn. In addition, as detailed in Nazarian et al. (1997), the method is not applicable to very thin layers and situations where the difference in moduli of adjacent materials is small. Other concerns with the method are the viscous behavior of the HMA which may dampen the signal and large surface aggregates that may scatter the signal.

In recent years, focused effort has been directed towards using advanced signal processing techniques to improve the analysis and facilitate the interpretation of IE test results, especially when low-frequency high-amplitude flexural vibrations may mask the resonant

reflections of interest (Medina and Garrido, 2007). In that study, windowing was used to remove the Rayleigh waves, and after that, a multi-cross-spectral density function was defined by applying cross-spectral density to the signals collected at several distances from the impact point. This process eliminated several undesirable peaks contained in the frequency spectrum, thus interpretation of the longitudinal waves becomes much easier. To validate the proposed method, a finite element study was conducted to model composite (asphalt over concrete) thin plates with shallow debonding at the interface of an asphalt overlay placed on a concrete slab. The noise and the undesirable peaks in the frequency domain were reduced after the technique was applied, facilitating the interpretation of results. In another example, a small plate made up of two layers was considered. The radius of the plate was 400 mm, and the top layer (asphalt) and the bottom concrete layer were 20 and 30 mm thick respectively. A shallow delamination in the contact zone between the concrete slab and the asphalt overlay was considered. In the IE spectrum, the resonant frequency of delamination was difficult to detect mainly because the amplitudes of the flexural modes of vibration of the whole plate as well as the thin layer above the delamination were dominating the spectrum. When the low frequency peaks of the flexural modes were removed and the multicross-spectral density function was applied, only the peak corresponding to the delamination depth was evident, demonstrating the usefulness of the proposed method. It should be emphasized that the low frequency flexural peak is very good indication of the debonding at shallow depths. The additional analysis is necessary of the depth of the debonding has to be estimated.

SASW

The SASW method provides the shear wave velocity profile. The ultrasonic surface wave (USW) method is a variation of the SASW where the frequencies are confined to very high

frequencies and therefore the shear wave velocity profile within the topmost layer is resulted (Nazarian et al., 1993). In the SASW/USW, the variation in the phase velocity with wavelength, called a dispersion curve, is generated. At wavelengths less than or equal to the thickness of the uppermost layer, the velocity of propagation of surface waves is more or less independent of wavelength. Assuming that the properties of the uppermost layer are uniform, if one simply generates high-frequency (short-wavelength) waves, the phase velocity of the upper layer can be determined. The wavelength at which the phase velocity is no longer constant is closely related to the thickness of the top layer (Nazarian et al., 1997).

For two layers with similar modulus bonded together, the variation in modulus with depth is more or less constant. However, when the two layers are debonded, the variation in modulus with depth is significantly reduced below the interface of the two layers. This principle can be readily used to not only detect but also identify the approximate depth of the debonded layers. This method has been successfully used in a few forensic studies to detect HMA debonding (Hammons et al., 2005). As an example, typical dispersion curves (the variations in modulus versus depth) obtained through the USW analysis from locations of an intact and a damaged core are shown in Figure A.22. The dispersion curve for the intact core would have been constant if different lifts were of the same material. However, at least four different lifts can be identified in the first 12 in. of the intact core shown in Figure A22a. The top layer (first 4 inches) is significantly stiffer than the rest. From 4 to 6 inches, the material seems to be of lower quality and below 6 inches the modulus increases again. In the case of the damaged core, the top 4 in. seem to be stiffer. A significant drop in modulus is observed at a wavelength of 4 in. where some loss of material was found due to stripping. The modulus increases again at a depth of 6 in.
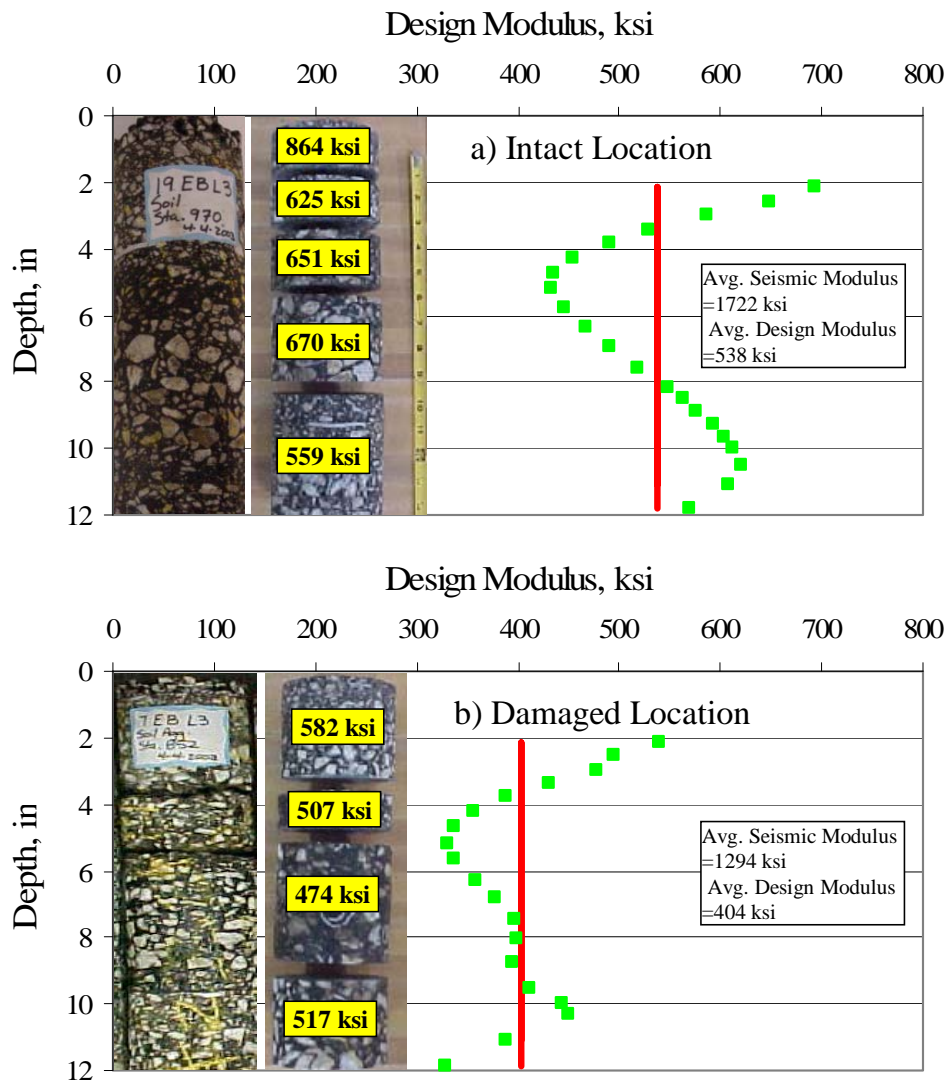
Figure A.22 – Typical Intact and Damaged-Location Dispersion Curves and Variation in Modulus with Depth for Cores after Being Saw cut (a) Intact Location and (b) Damaged Location. (Hammons et al., 2005)

To further investigate the differences observed in dispersion curves, retrieved cores were saw cut into distinct layers, and the seismic modulus of each layer was determined in the laboratory. The core pieces and their corresponding moduli are also shown in Figure A.22. For the intact core, the laboratory measurements demonstrate a similar trend as that delineated by USW. Removal of some material from the interfaces during the saw cut operations, and the

averaging process of moduli of deeper layers inherent in surface wave method may explain the higher values in moduli obtained with the ultrasonic device. For the damaged core, the modulus measured with the USW method compares reasonably well with the modulus from the ultrasonic device for the top 4 in. (depth where the stripping occurred). The USW results below a depth of 4 in. are considerably lower than those from the ultrasonic device because of the significantly lower modulus of the stripped layer (note that the stripped material was lost during coring).

Delatte et al. (2002) recognized the SASW method as an NDT tool for estimating the engineering properties of surface layers. In their study, thin concrete overlays on top of asphalt in airport pavements were investigated with the FWD and SASW techniques to measure stiffness of the top and underlying layers and to detect potential debonding. It was concluded that the SASW method could be used to assess the condition and thickness of pavement layers and could be used to monitor the overlay condition and investigate potential problem areas. A combination of SASW and FWD testing was recommended for better evaluation of airport pavements.

IE-SASW

Nazarian et al. (1993) developed automated testing equipment known as the Seismic Pavement Analyzer (SPA). Later, the same technology was implemented in portable hand-held device called the Portable Seismic Pavement Analyzer (PSPA). PSPA can automatically conduct both IE and SASW tests simultaneously and it is designed so that it would work on rough HMA surfaces. The PSPA measures the average modulus of the exposed surface layers within a few seconds in the field. The operating principle of the PSPA is based on generating and detecting stress waves in a layer. The Ultrasonic Surface Wave (USW) interpretation method (Nazarian et al. 1993) is used to determine the modulus of the material. The PSPA, as shown in Figure A.23, consists of two transducers (accelerometers in this case) and a source

packaged into a hand-portable system, which can perform high-frequency (1 kHz to 50 kHz) seismic tests. The source package is also equipped with a transducer for consistency in triggering. The device is operable from a computer tethered to the hand-carried transducer unit through a cable that carries operational commands to the PSPA and returns the measured signals to the computer.

To collect data with the PSPA, the technician initiates the testing sequence through the computer. All the other data acquisition tasks are handled automatically by the computer. The source, which is a computer-controlled solenoid, is activated four to six times. Pre-recording impacts of the source are used to adjust the amplifiers in a manner that optimizes the dynamic range of the electronics. The outputs of the three transducers from the final three impacts are saved and averaged for more reliability. Typical voltage outputs of the three accelerometers are shown in Figure A.24. In any seismic method, the goal is to determine the velocity of propagation of waves within a material. These records are used to determine the velocity of propagation of waves in the HMA layer.
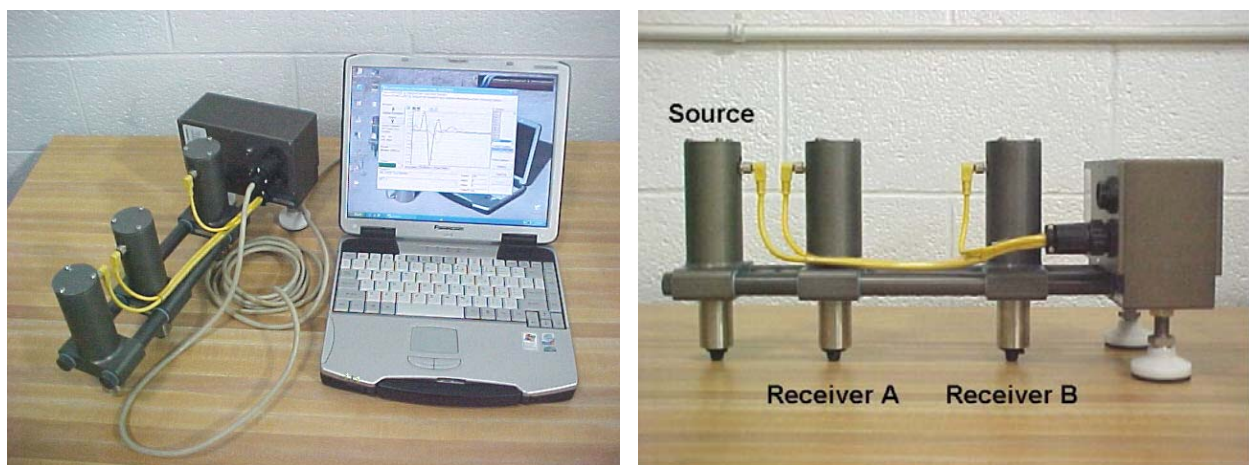
Figure A.23 – Portable Seismic Pavement Analyzer
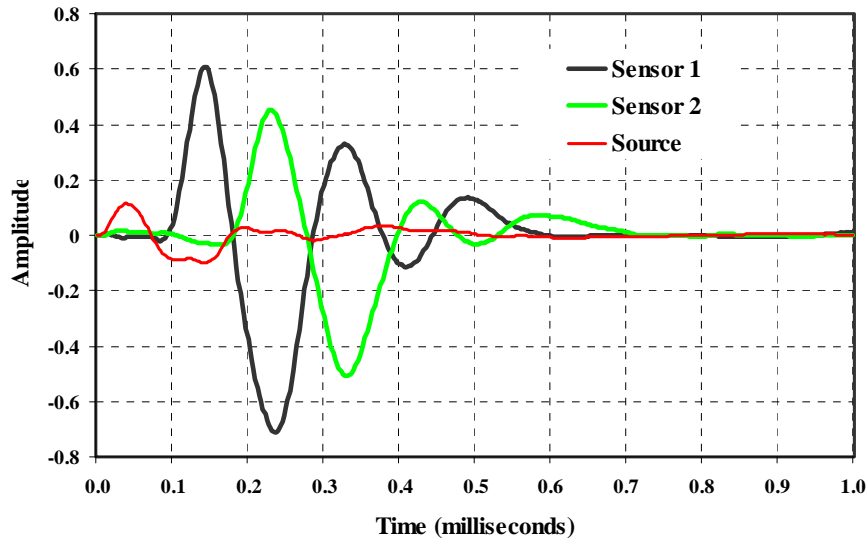
Figure A.24 – Typical Records from PSPA

The SASW method can yield the wave velocity and subsequently the modulus of the uppermost layer. The results of IE test will reveal the locations of defects within the layer. Knowing the velocity from SASW test, one may determine the depth of the reflectors and/or the thickness of the top layer. This process has been automated and incorporated in PSPA. PSPA has been previously used for determining the modulus, and thickness of the upper pavement layer (Ganji, 1998). The old version of the PSPA was proved successful for detection of debonding between bituminous layers with similar properties, provided the interface is deeper than 100 mm from the pavement surface (Armitage et al., 2000; Kruntcheva et al., 2000). The newer version of PSPA is equipped with a higher frequency source that can provide information for shallower depths. PSPA has been recently used to detect stripping and other types of water damage in asphalt pavements (Hammonds et al., 2005). SASW-based moduli provided supplementary information which greatly facilitated the interpretation of IE test results.

Ultrasound

Ultrasonic waves are elastic waves of audible frequency (above 20 kHz). Ultrasonic testing has been used for detection and characterization of internal defects in a material, and measurement of the thickness and mechanical properties of a solid (stresses, toughness, and elasticity constants) by Garbacz and Garboczi (2003).

The ultrasonic-echo method is often used for defect detection. The test procedure involves the generation of a short pulse of ultrasonic frequency and transmitting it through the material by a transducer. After being reflected by the material's heterogeneity (including defects) or by the limiting boundaries, the pulses are recorded by the receiving transducer which can be the transmitter itself as shown in Figure A.25. A portion of the ultrasonic wave which is reflected by the target defect is known as the defect's echo. The portion of the ultrasonic energy that reaches the opposite wall of the tested material, is reflected and returns to the receiver with some delay is known as the back-wall echo. Knowing the ultrasonic wave velocity in the material under investigation, the depth of the defects or other reflecting surfaces can be determined from the measured arrival times of the echoes (Garbacz and Garboczi, 2003).

Ultrasonic testing of multi-phase heterogeneous materials such as HMA is challenging. The challenge lies in the fact that heterogeneities of comparable size (or larger than) the ultrasonic wavelength result in scattering and attenuation of ultrasonic energy. The grain size should be significantly smaller than the target defects; otherwise, any defect echo will be masked by the echoes from the grain boundaries.
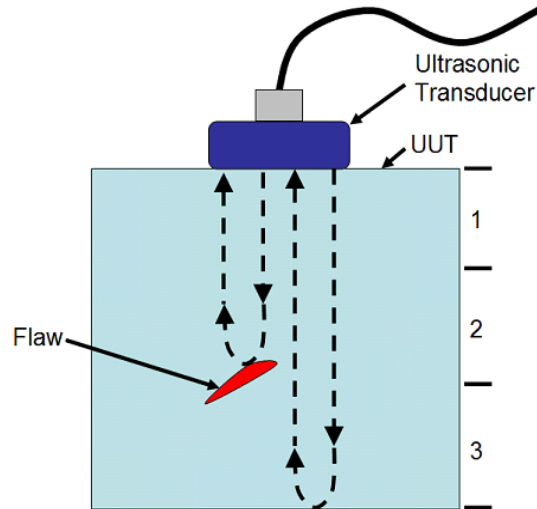
Figure A.25 – Delamination Detection by Ultrasonic Echo Method

Recently a low-cost multi-sensor dry-contact *Ultrasonic Device* (A1040 POLYGON, as shown in Figure A.26) has been developed in Russia (AKC) in cooperation with Germany's Federal Institute for Materials Research and Testing (BAM). The equipment includes 8 to 16 spring-mounted ultrasonic transducers of a nominal frequency of 50 KHz (20-100 KHz). Using real-time tomographic imagining principles, this system provides a detailed image of the interior of the material and can resolve cracks, flaws, and other heterogeneities, as shown in Figure A.27. This equipment has been developed specifically for testing of concrete and has not been used in imagining of HMA (Acoustic Control Systems, www.acsys.ru/eng/).

Figure A.26 – A1040 POLYGON Ultrasonic Device
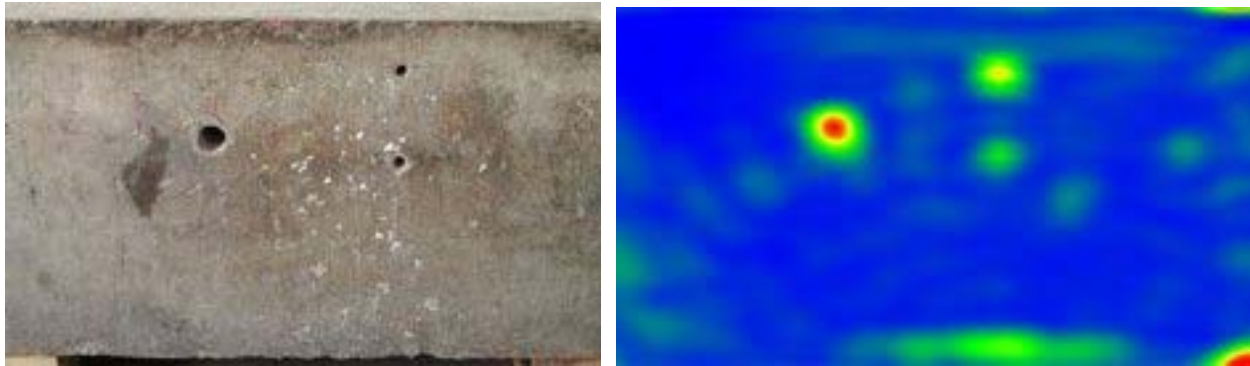
Figure A.27 – Real Time Tomographic Imaging of an Internal Structure of a Concrete Specimen

Thermal Methods

Infrared Thermography

Infrared (IR) thermography provides a nondestructive means of temperature measurement by detecting the differences in infrared radiations emitted from objects at different temperatures. The presence of shallow subsurface voids results in anomalies (hot or cold spots) in surface temperature distribution maps. Therefore, IR thermography can be used to indirectly locate near-surface flaws and voids

The technique involves the use of IR cameras for non-contact surface temperature measurement, as shown in Figure A.28. In some applications, the object to be tested is artificially heated to produce the desired temperature differentials (active method). In other applications, the heat source is either the solar radiation or the natural temperature of the material or structure being tested. In either case the infrared sensor detects the infrared radiation emitted from the object, and converts the radiation measurement into a temperature measurement using the Stefan-Boltzmann Law:

$$Q = \sigma E(T^4 - T_0^4) \tag{A.6}$$

where Q is the radiation emitted from an object, σ is the Stefan-Boltzman constant, E is the emissivity of the object, T is the absolute temperature of the object, and T_0 is the absolute temperature of the surroundings.

Figure A.28 – Infrared Survey Vehicle

IR thermography has found some applications in pavement construction and maintenance. The technology has been used at the time of placement of HMA to investigate the relationships between the rate of cooling of newly placed HMA overlays and the variations in the measured post-construction volumetric and engineering properties of field cores (Sebesta and Scullion, 2002). Stroup-Gardiner and Brown (2000) showed that temperature differentials measured by IR were significantly related to changes in the properties of the finished mat such as air void content and gradation. On existing pavements, the IR technology can be used to relate local temperature gradients to the presence of shallow subsurface flaws in HMA. It is believed that the trapped air in a delamination or cracked zone acts as an insulator blocking the heat transfer between the HMA lifts above and below the delaminated interface. Consequently, the

surface of the pavement over the delaminated exhibits a temperature gradient (negative at night and positive during the day) with respect to its surrounding fully bonded area.

An example of temperature distribution during daytime condition using finite element analysis for an asphalt layer with some delamination is shown in Figure A.29 (Tsubokawa et al., 2007). In one study, the asphalt pavement was actively heated to detect defects (Maser, 2003). The IR technology has been previously used for detection of shallow delamination in HMA airfield pavements in Japan and Greece (Tsubokawa et al., 2007, Moropoulou et al., 2002). For example, two thermographic images taken from a runway in the International Airport of Athens are shown in Figure A.30. Surveys were carried out through daytime, at times of rapid heat transfer (approximately 3 hours after sunrise), between January and March. The surface temperature of the pavement, as well as the environmental conditions, such as air temperature and relative humidity, were taken into consideration. The defects were identified where a temperature difference of at least 0.5° between the defected areas and intact pavement exists (ASTM standard D4788-88) and marked on the thermographs as shown in Figure A.30. These defects were attributed to the aging of the HMA airfield pavement. They concluded that to achieve the best results, tests should be executed on sunny days and during daytime to allow more rapid and effective energy transfer to the pavement. Since moisture could affect the surface temperature and the defect detection, tests should be completed at times where the pavements are dried out (Moropoulou et al., 2002).
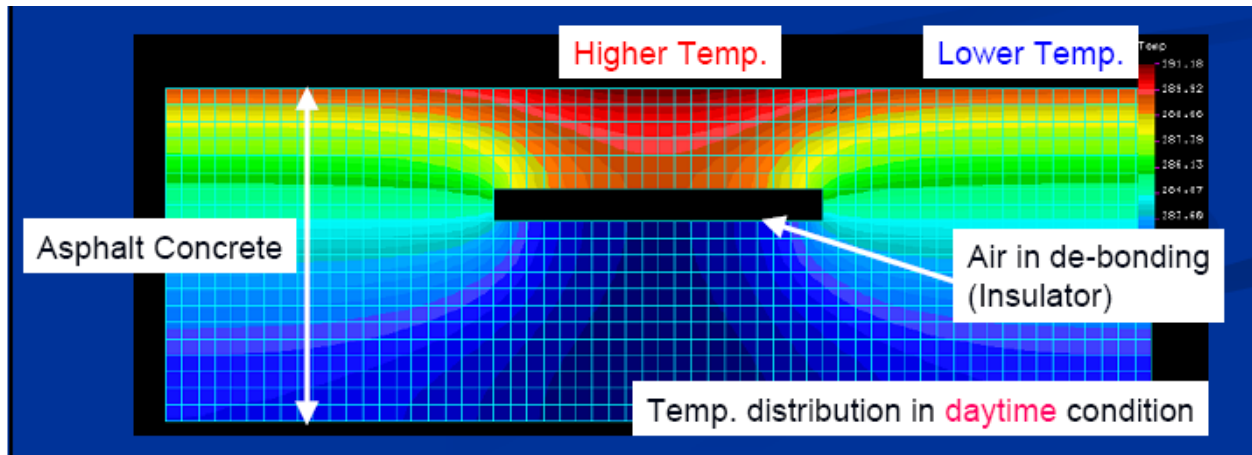
Figure A.29 – Example Image of Thermal Analysis (Daytime Condition) (from Tsubokawa et al., 2007)
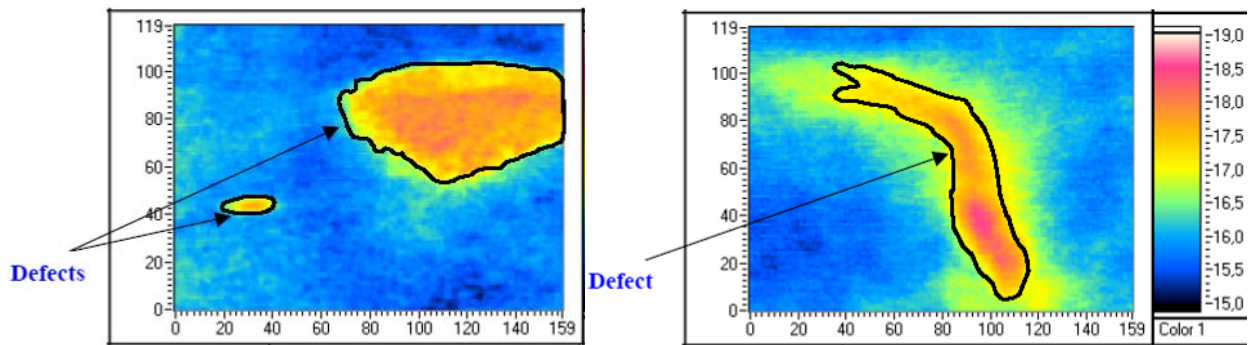
Figure A.30 – Thermographs Showing Defects on Asphalt Runway (Moropoulou et al., 2002)

Infrared thermography and Impact Echo were used side-by-side to detect delamination in airport flexible pavements in Japan (Tsubokawa et al., 2007). A trial section on a runway-taxiway intersection of 10 m by 10 m was used. As shown in Figure A.31a, the inspection area was divided into small squares of 50 cm by 50 cm, each area was tested using IE, and the debonded zones were identified and marked. Later, the infrared images of the same area were taken every 30 min from 0:30 a.m. to 5:30 a.m. (Figure A.31b). Air temperature and intensity of

solar radiation during the tests were recorded. In Figure A.31b, darker areas represent lower temperature than the white areas. The low-temperature areas (cold spots) generally matched the debonded areas found by the IE method. A number of cores were retrieved from the seven low temperature areas marked in Figure A.31b. Shallow debonding (40 to 70 mm below the surface) at all seven locations was confirmed (Tsubokawa et al., 2007).

a) Debonded Areas   b) Infrared Image
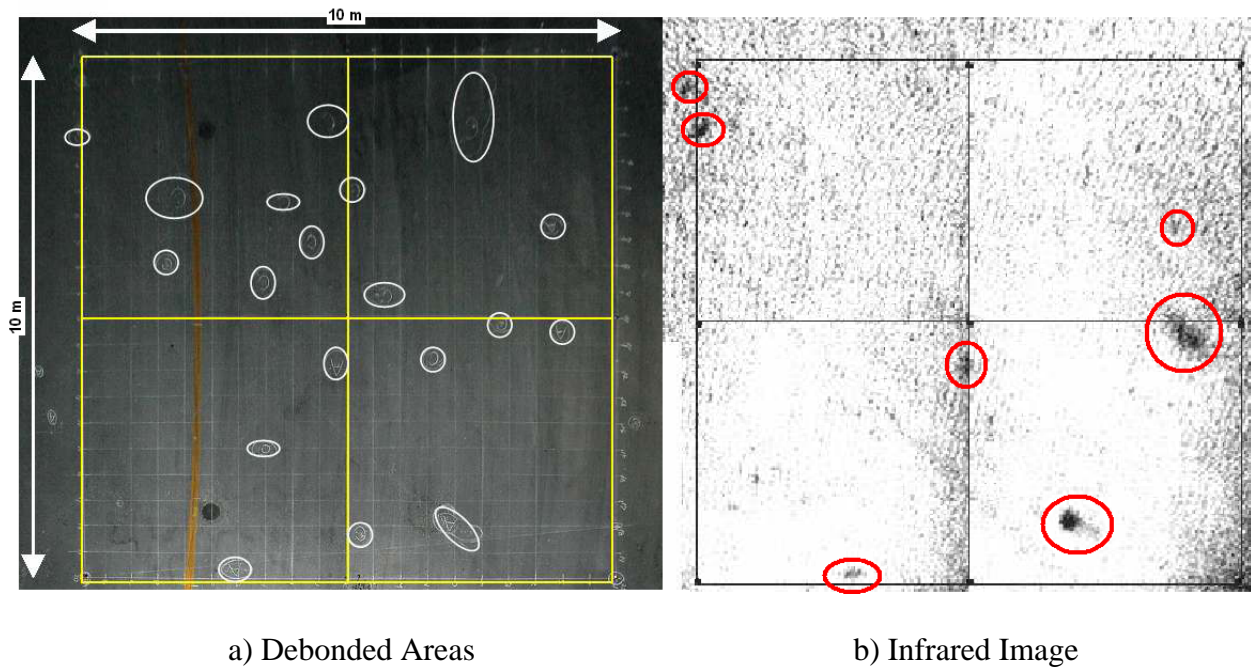
Figure A.31 – Low-temperature Areas Generally Match the Debonded Areas Found by IE.

(Tsubokawa et al., 2007)

In sum, both studies concluded the effective use of the IR for large areal inspection but also reported a number of limitations associated with the application of this technology. The IR technology provides a rapid means of inspection of the large airfield pavements and gives areal images. However, it cannot provide the exact dimensions or the depth of the localized defects. Moreover, the reliability of the results is compromised by its high sensitivity to ambient environmental and surface conditions such as solar radiations, air temperature, wind speeds, surface texture, pavement grooves, the external debris, shadow zones, etc. Some of the

environmental effects can be minimized if the evaluation is based on temperature gradients (relative temperatures) rather than absolute temperature values for the effect of ambient condition will be the same and therefore, will be neutralized in individual thermal shots. The presence of external debris such as rubber on the surface of the runways introduces further difficulties in interpretation of thermal images (Tsubokawa et al., 2007). Furthermore, given the dependency of temperature differentials on air void content, a coarsely segregated spot may be misinterpreted as a delaminated zone.

APPENDIX B

JOB MIX FORMULAE

MATERIAL DATA SHEET

ASPHALTIC CONCRETE MIX DESIGN

February 8, 2008

SOURCE: JOBE MATERIALS, L.P.
MATERIAL: PMBP ITEM P 403 – BASE COURSE
PROJECT: EPIA – RECONSTRICTION OF TAXIWAY J & M
CLIENT: C F JORDAN INFRASTRUCTURES

SIEVE SIZE	MASTER GRADING	JMF	ACTION LIMIT
1"	100	100	100
3/4 "	76 – 98	96	90 - 100
1/2 "	66 – 86	82	76 – 88
3/8	57 – 77	71	65 - 77
No.4	40 – 60	50	44 - 56
No. 8	26 – 46	35	--------
No.16	17 – 37	26	21 - 31
No.30	11 – 27	19	--------
No.50	7 – 19	13	10 – 16
No.100	6 – 16	7	--------
No. 200	3 -- 6	4.7	2.7 – 6.7

Asphalt Content	4.5 – 7.0	4.9	4.45 – 5.35
Percent Air Voids:	4.0%		Design : 2 – 5
Marshal Stability : 2780			Design : 1800 Min.
Flow : 12			Design : 8 – 16
Voids in Mineral Agg (Vma): 15			Minimum: 14
Voids filled with Asphalt: 73 %			Range: 65 -78
TSR : 90 .1%			Minimum: 75 TSR
Dust / Asphalt Ratio : 0.96			Range: 0.8 to 1.4
Asphalt film thickness: 9.7 microns			Minimum: 8 microns

Recommend Mixing / discharge Temp: 320 F, Laboratory molding Temp: 295 F
Design based on 75 blow Marshall method, per Asphalt Institute MS-2 6 th Ed. and
ASTM D 6926 & 6927. Asphalt cement is Western refining PG 64-22. Liquid anti-
strip Azko Nobel Wet –fix 312, added at a rate of 0.5%. Mix was recently used for
Reconstruction of Runway 8R-26L and Taxiway E.

JOBE MATERIALS, LP

RICHARD L. RICE, CET
QUALITY CONTROL

MATERIAL DATA SHEET

ASPHALTIC CONCRETE MIX DESIGN

February 8, 2008

SOURCE: JOBE MATERIALS, L.P.
MATERIAL: PMBP ITEM P 401 – SURFACE COURSE
PROJECT: EPIA – RECONSTRICTION OF TAXIWAY J & M
CLIENT: C F JORDAN INFRASTRUCTURES

SIEVE SIZE	MASTER GRADING	JMF	ACTION LIMIT
1"	100	100	100
3/4 "	76 – 98	96	90 - 100
1/2 "	66 – 86	82	76 – 88
3/8	57 – 77	71	65 - 77
No.4	40 – 60	50	44 - 56
No. 8	26 – 46	35	--------
No.16	17 – 37	26	21 - 31
No.30	11 – 27	19	--------
No.50	7 – 19	13	10 – 16
No.100	6 – 16	7	--------
No. 200	3 -- 6	4.7	2.7 – 6.7
Asphalt Content	4.5 – 7.0	5.2	4. 75 – 5.65

Percent Air Voids: 3.5%   Design : 2.8 – 4.2
Marshal Stability : 2800   Design : 2150 Min.
Flow : 13   Design : 10 - 14
Voids in Mineral Agg (Vma): 15   Minimum: 14
Voids filled with Asphalt: 75 %   Range: 65 -78
TSR /Dry Strength @ 5.2 : 92 / 234   Minimum: 75 / 200 psi
Dust / Asphalt Ratio : 0.9   Range: 0.8 to 1.4
Asphalt film thickness: 10.4 microns   Minimum: 8 microns

Recommend Mixing / discharge Temp: 335 F, Laboratory molding Temp: 305 F
Design based on 75 blow Marshall method, per Asphalt Institute MS-2 6 th Ed. and
ASTM D 6926 & 6927. Asphalt cement is Western Refining PG 76-22. Liquid anti-
strip Akzo Nobel Wet-fix 312 added at a rate of 0. 5%. Mix was recently used for
Reconstruction of Runway 8R-26L and Taxiway E.

JOBE MATERIALS, LP

RICHARD L. RICE, CET
QUALITY CONTROL

APPENDIX C

CONSTRUCTION DETAILS OF CONTROLLED STUDY

Schematic of Delamination on Controlled Study

Details on the distribution of the debonding for each of the prepared sections are illustrated on Figure C.1 for the coarse mix sections, Figure C.2 for the fine mix sections and Figure C.3 for the transition area.

a) Section 2 (2.5 in deep)

b) Section 3 (2.5 in deep) and 5 (5 in deep)
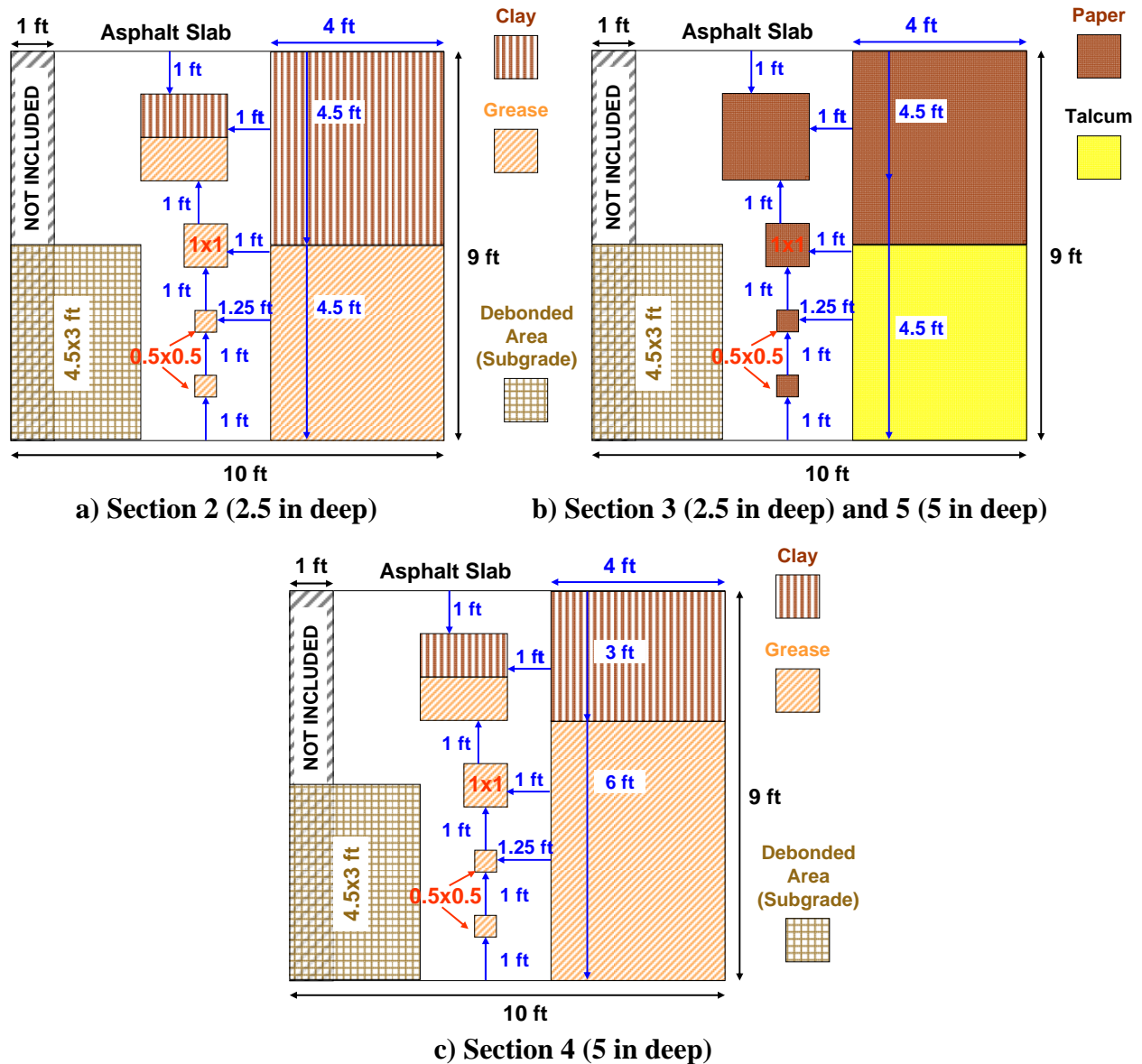
c) Section 4 (5 in deep)

Figure C.1 – Layout of Delamination on Coarse Mix Sections
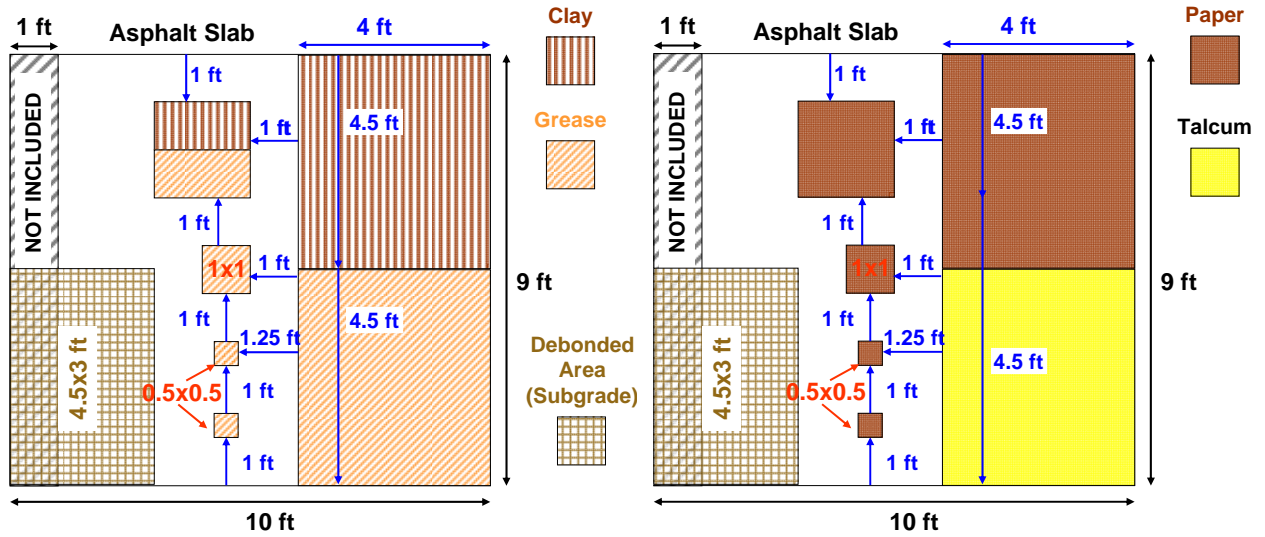
a) Section 7 (2.5 in deep) and 9 (5 in deep)   b) Section 8 (2.5 in deep) and 10 (5 in deep)

Figure C.2 – Layout of Delamination on Fine Mix Sections
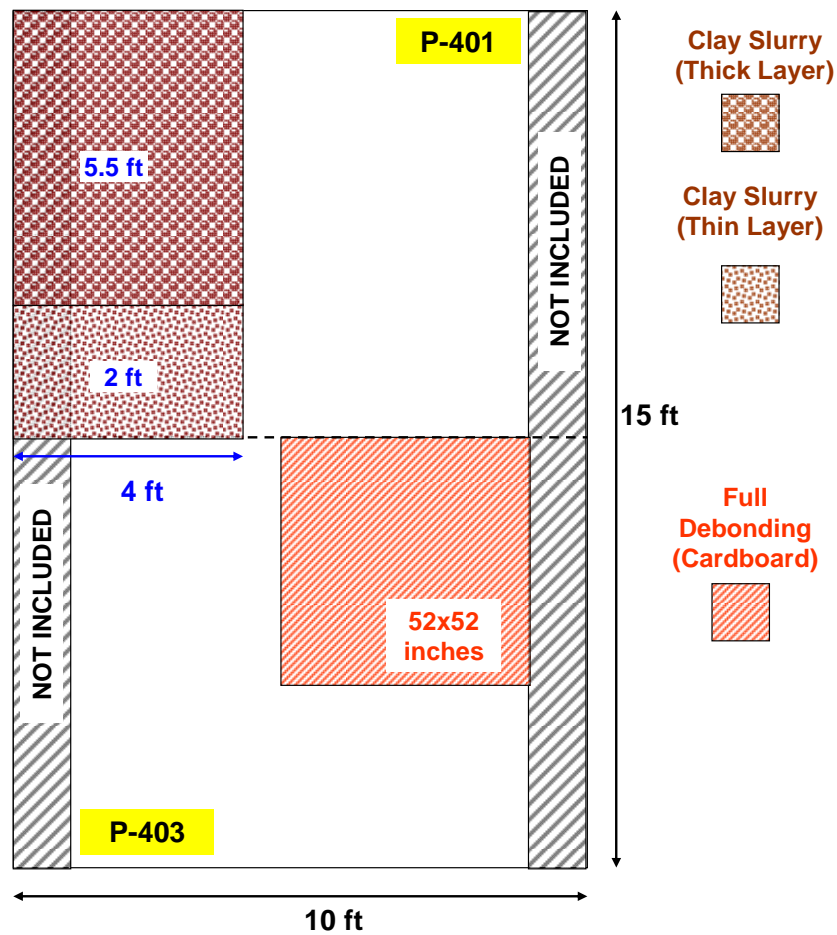
Figure C.3 – Layout of Delamination on Transition Sections

44

Subgrade Preparation and Construction of Asphalt Base

During the first day of construction, the subgrade was prepared to accommodate the asphalt base. The subgrade was reworked, graded, watered and compacted during the first day of construction (see Figure C.4).

Figure C.4 – Preparation of Subgrade

On the second day, the marking of the sections and the placement of the subgrade debonding material was conducted initially. Sections of 4.5 by 3 ft corrugated cardboard soaked in motor oil were used to simulate debonding between the subgrade and the asphalt base, as detailed in Figure C.5a.

Once the subgrade was prepared, the asphalt base mix (P-403) was shipped to UTEP and placed in the asphalt paver (see Figure C.5b). An asphalt paver distributed the asphalt on a 10 foot wide lane along the length of the section (Figures C.5c and C5.d). After the asphalt base was laid down a static compactor was used to compact the asphalt to the desired compaction level and to match the required thickness of 3 inches (Figures C.5e and C5.f).

After the asphalt base was compacted and the surface was cool enough, the locations of the different debonded areas were marked on Sections 4, 5, 9 and 10. As an example, Figure C.6a shows debonding areas on sections 9 and 10 after they were marked out on the pavement. The

a)

b)

c)

d)

e)

f)

Figure C.5 – Construction of Asphalt Base

spreading of the debonding agents on these sections was next. Figure C.6b illustrates the application of grease, clay slurry and talcum powder on the same sections. After these materials dried out, debonding areas were covered with pieces of corrugated cardboard and plywood to avoid intrusion from emulsion and prevent damage from construction traffic (see Figure C.6c). Then, a standard amount of tack coat was applied on the entire section, as depicted in Figure C.6d.

a)

b)

c)

d)

Figure C.6 – Construction of Debonding Sections on Asphalt Base (Deep Debonding)

As recommended by the technical panel a thermocouple to measure the temperature of the asphalt was installed in Section 1. A small groove was excavated and the thermocouple was inserted and attached to the pavement (see Figure C.7). The temperature sensor is used at the time of field testing to measure temperature profiles within the pavement structure.

Figure C.7 – Installation of Thermocouple on Asphalt Base

Construction of Asphalt Pavement

After the tack coat on the asphalt base was dry, the material used as first layer of asphalt (P-401 mix) was distributed with the paver (see Figures C.8a and C.8b). Some loose material was spread on top of the small debonding areas these areas to avoid any damage from the paver (Figure C.9a). The big debonding areas dig not show any damage from the paver as it was going trough (see Figure C.9b). After the asphalt was placed, the same static compactor was used to achieve the desired height of 2.5 inches (see Figure C.9c). Similarly to the asphalt base, a thermocouple was installed after the asphalt was compacted. In this case, the thermocouple was placed on the transition section (see Figure C.9d).

a)	**b)**

Figure C.8 – HMA Delivery to the Site

On the third day the construction of the top layer of HMA was accomplished. The same process followed to construct the debonding areas the day before was reproduced on the second layer of HMA (see Figure C.10a) for Sections 2, 3, 7 and 8. After the asphalt was placed with the paver, it was compacted with a static compactor followed by a pneumatic roller to finish the section (see Figure C.10b).

In addition to the predetermined debonded areas, two supplementary areas were located on the transition section. One area of severe debonding was constructed on the coarse mix segment. A cardboard section of 52x52 inches was attached to the bottom layer of HMA (see Figure C.11a). The other area covered a section of 7.5 foot long and 4 foot wide on the fine mix. On the first 2 feet a very thin application of clay slurry was used and on the other 5.5 feet a very thick layer of the same material was employed as shown in Figure C.11b.

49

a)

b)

c)

d)

Figure C.9 – Construction of Bottom Layer of HMA

a)

b)

Figure C.10 – Construction of Top Layer of HMA

| a) | b) |

Figure C.11 – Construction of Additional Debonding on Transition Section

Table C.1 – NDG Density Results after Completion of Controlled Study

Location	Section Number and Density (pcf)										
	1	2	3	4	5	T	6	7	8	9	10
LWP	139.2	150.1	141.8	142.9	137.5	141.5	148.5	140.8	141	138.8	148.9
Center	138.8	139.8	136.1	151.1	139.7	142.3	138.8	143.8	140.7	138	140.7
RWP	138.3	137.3	136.9	140.4	159.3	147.7	140.8	146.8	135.5	140	140.1
						145.8					

Table C.2 – Percentage of Marshall Density Obtained with NDG after Completion of

Controlled Study

Location	Section Number and % of Marshall Density*										
	1	2	3	4	5	T	6	7	8	9	10
LWP	92.9	100.1	94.6	95.4	92	94.4	99	93.9	94.1	92.6	99.3
Center	92.6	93.2	90.8	100.8	93.2	94.9	92.6	95.9	93.9	92.1	93.9
RWP	92.3	91.6	91.3	93.6	106.2	98.5	93.9	97.9	90.4	93.4	93.4
						97.2					

* 100% of Marshall Density was 149.9 pcf

Table C.3 – PSPA Results after Second Day of Construction (Lifts 1 and 2 Combined)

Location	Point	Seismic Modulus (ksi)		
		LWP	Center	RWP
S10, Deep and Full Debonding	2	1858	1708	1222
	1	1891	1901	1108
S9, Deep and Partial Debonding	2	2004	1703	1312
	1	1651	2065	1503
S8, Shallow and Full Debonding	2	1759	2051	1858
	1	2112	2197	1957
S7, Shallow and Partial Debonding	2	1910	1877	1731
	1	1656	1811	1642
S6, Intact Area	2	1995	2018	1717
	1	1943	2037	1905
TRANSITION	1	1850	1872	1896
S5, Deep and Full Debonding	2	1868	1703	1133
	1	1797	1440	1056
S4, Deep and Partial Debonding	2	1774	1623	1171
	1	1534	1585	1110
S3, Shallow and Full Debonding	2	1670	1614	1548
	1	1599	1726	1651
S2, Shallow and Partial Debonding	2	1614	1689	2004
	1	1585	1670	1642
S1, Intact Area	2	1872	1543	1717
	1	1759	1402	1640

Table C.4 – PSPA Results after Second Day of Construction (Top Lift)

Location	Point	Seismic Modulus (ksi)		
		LWP	Center	RWP
S10, Deep and Full Debonding	2	1825	1769	1563
	1	1938	2216	1470
S9, Deep and Partial Debonding	2	2013	1891	1440
	1	1736	2183	1778
S8, Shallow and Full Debonding	2	1821	2140	1882
	1	2070	2169	1882
S7, Shallow and Partial Debonding	2	2009	1966	1736
	1	1741	1910	1637
S6, Intact Area	2	2131	2206	1835
	1	1976	2145	1999
TRANSITION	1	1995	1924	1818
S5, Deep and Full Debonding	2	1990	1712	1494
	1	1731	1618	1317
S4, Deep and Partial Debonding	2	1821	1604	1442
	1	1505	1585	1352
S3, Shallow and Full Debonding	2	1679	1604	1609
	1	1646	1778	1614
S2, Shallow and Partial Debonding	2	1637	1844	1853
	1	1806	1694	1651
S1, Intact Area	2	1849	1548	1698
	1	1712	1427	1621

Table C.5 – PSPA Results after Completion of Construction (3 Lifts Combined)

Location	Point	Seismic Modulus (ksi)		
		LWP	Center	RWP
S10, Deep and Full Debonding	2	1628	1948	1684
	1	1885	1797	1648
S9, Deep and Partial Debonding	2	1774	1659	1741
	1	1745	2023	1794
S8, Shallow and Full Debonding	2	1938	1888	1321
	1	1717	1872	1197
S7, Shallow and Partial Debonding	2	1936	1679	1511
	1	1587	1590	1806
S6, Intact Area	2	1901	1792	2055
	1	1891	1941	1853
TRANSITION	1	1626	1549	1769
S5, Deep and Full Debonding	2	1979	1524	1229
	1	1853	1969	1559
S4, Deep and Partial Debonding	2	2104	2007	1870
	1	1764	2032	1618
S3, Shallow and Full Debonding	2	1599	1800	1465
	1	2092	1621	1440
S2, Shallow and Partial Debonding	2	1599	1844	1344
	1	2177	2079	1650
S1, Intact Area	2	2506	2042	1874
	1	1835	1943	1882

Table C.6 – PSPA Results after Completion of Construction (Top Lift)

Location	Point	Seismic Modulus (ksi)		
		LWP	Center	RWP
S10, Deep and Full Debonding	2	1929	2434	2051
	1	2079	1905	2070
S9, Deep and Partial Debonding	2	1849	1891	1949
	1	1976	2308	1982
S8, Shallow and Full Debonding	2	2432	2095	1936
	1	1924	2129	1479
S7, Shallow and Partial Debonding	2	2065	1872	1684
	1	1706	1915	2096
S6, Intact Area	2	2023	1929	2324
	1	2366	2136	2124
TRANSITION	2	1946	1643	1896
	1	2010	1978	1752
S5, Deep and Full Debonding	2	1943	2336	2004
	1	2365	2214	2206
S4, Deep and Partial Debonding	2	1679	2148	2244
	1	2070	2007	1951
S3, Shallow and Full Debonding	2	2311	1681	1761
	1	2007	2264	1652
S2, Shallow and Partial Debonding	2	2515	2380	2102
	1	2779	2368	2004
S1, Intact Area	2	2032	2279	1966
	1	2018	2173	1886

APPENDIX D

COMPLETE NDT RESULTS ON CONTROLLED STUDY

Table D.1 – PSPA Results on Small Scale Study (3 Lifts Combined). Coarse Mix

Section	Point	Seismic Modulus from PSPA (for 8 in), ksi				
		Line 1	Line 2	Line 3	Line 4	Line 5
S5, Deep and Full Debonding	5	1733	1851	1652	1508	1627
	4	1845	1767	1914	1599	1421
	3	1914	1879	1684	1690	1481
	2	1783	1374	1614	1573	1284
	1	1666	1827	1651	1442	1527
S4, Deep and Partial Debonding	5	1645	1712	1984	1837	1437
	4	1724	1502	2025	1653	1511
	3	1668	1612	1676	1696	1726
	2	1955	1729	1815	1817	1548
	1	1808	1715	1666	1453	1044
S3, Shallow and Full Debonding	5	1633	1347	1747	1387	1091
	4	1933	1643	1714	1266	1054
	3	1956	1611	1617	1326	1313
	2	1891	1527	2325	987	1151
	1	1983	1874	1908	1289	1048
S2, Shallow and Partial Debonding	5	1929	1626	1563	1320	1146
	4	2214	1778	1974	1768	1774
	3	1951	1755	1899	1740	1626
	2	2236	1957	1807	1643	1667
	1	2231	1685	1977	1804	1902
S1, Intact	5	1991	1829	1825	1751	1922
	4	1736	1636	1589	1891	1876
	3	1812	1714	1854	1963	1683
	2	1777	1690	1835	1626	1699
	1	1768	1921	1674	1602	1745

Table D.2 – PSPA Results on Small Scale Study (3 Lifts Combined). Fine Mix and Transition

Section	Point	Seismic Modulus from PSPA (for 8 in), ksi				
		Line 1	Line 2	Line 3	Line 4	Line 5
S10, Deep and Full Debonding	5	1875	1925	2340	1958	1812
	4	1802	1993	2213	2018	1677
	3	1760	2356	2234	2073	1572
	2	1990	1902	2058	2006	1615
	1	1873	1899	2117	1888	1557
S9, Deep and Partial Debonding	5	1802	1569	1646	1598	1729
	4	1655	1753	2050	1986	1820
	3	1845	1720	1922	2093	1661
	2	1882	1741	1825	2140	2034
	1	1828	1795	1836	1397	1446
S8, Shallow and Full Debonding	5	1869	1469	2141	1629	1375
	4	1448	1513	1919	1542	1463
	3	1524	1856	2335	1667	1409
	2	1873	1744	2048	1674	1469
	1	1598	1719	2051	1578	1612
S7, Shallow and Partial Debonding	5	1644	1300	1649	1531	1538
	4	1727	2023	1854	1547	1611
	3	1628	1960	1880	1592	1777
	2	1824	1819	1750	1766	1680
	1	1762	1813	1961	1771	1841
S6, Intact	5	1717	1962	1569	1924	2180
	4	1827	2171	1968	2025	2031
	3	1809	2095	1828	2175	2078
	2	2083	2212	1967	2307	2156
	1	1443	1953	2134	2116	1990
TRANSITION	8	2200	1909	2137	2218	2010
	7	1558	1921	1854	1901	2064
	6	1373	1668	2268	1647	1983
	5	1680	2155	2229	2121	1747
	4	2037	2217	1607	1448	1185
	3	1995	1970	1411	1518	1163
	2	2321	2111	2254	2388	1925
	1	1989	1994	2246	1946	2041

Table D.3 – PSPA Results on Small Scale Study (Top Lift). Coarse Mix

Section	Point	Seismic Modulus from PSPA (for 2.5 in), ksi				
		Line 1	Line 2	Line 3	Line 4	Line 5
S5, Deep and Full Debonding	5	2130	2067	1858	1719	1599
	4	1891	1790	1989	1808	1500
	3	2106	1968	1909	1761	1758
	2	1862	1632	1773	1751	1528
	1	1899	1654	1936	1680	1888
S4, Deep and Partial Debonding	5	1771	1963	2179	2112	1736
	4	2086	1981	2118	1830	1768
	3	1705	1903	1862	1920	2178
	2	2225	1915	2104	2138	1963
	1	2043	1892	1973	2007	1487
S3, Shallow and Full Debonding	5	2008	1579	1942	1619	1347
	4	2169	1778	1775	1823	1537
	3	1947	1404	1626	1739	1643
	2	2071	1633	2242	1377	1508
	1	2001	2124	1889	1261	1457
S2, Shallow and Partial Debonding	5	2223	2078	2071	1427	1571
	4	2586	2022	2190	2026	2111
	3	2057	1999	2319	1952	2079
	2	2374	2206	2401	2007	2148
	1	2350	1828	2240	1997	2318
S1, Intact	5	2069	1701	2171	2111	2063
	4	2209	1805	1791	2169	2172
	3	2022	1875	1960	1854	1893
	2	2057	1773	2141	1886	1753
	1	2023	1842	1848	1868	1862

Table D.4 – PSPA Results on Small Scale Study (Top Lift). Fine Mix and Transition

Section	Point	Seismic Modulus from PSPA (for 2.5 in), ksi				
		Line 1	Line 2	Line 3	Line 4	Line 5
S10, Deep and Full Debonding	5	1977	2060	2403	2190	2292
	4	1832	2083	2422	2327	2068
	3	1882	2534	2440	2286	2020
	2	2105	2110	2162	2231	1973
	1	1989	2341	2297	2202	1994
S9, Deep and Partial Debonding	5	2084	1899	1767	1907	1878
	4	1862	1944	2212	2116	2128
	3	2170	2177	2277	2317	1826
	2	2211	1815	2240	2287	2028
	1	2063	2123	2157	1747	1878
S8, Shallow and Full Debonding	5	1929	1776	2279	1729	1717
	4	1522	1882	2226	2038	1832
	3	1657	1981	2377	2034	1780
	2	2003	1981	2366	1861	1669
	1	1754	1932	2054	1653	1779
S7, Shallow and Partial Debonding	5	1890	1630	1799	1694	1812
	4	1933	2198	2117	1825	1868
	3	1842	2094	2103	1815	2147
	2	1971	2148	1945	1998	1957
	1	1842	2003	2291	2025	1955
S6, Intact	5	1877	1954	1944	2293	2355
	4	1986	2443	2070	2365	2315
	3	1903	2034	2140	2359	2371
	2	2084	2434	2213	2455	2424
	1	1653	2309	1911	2215	2331
TRANSITION	8	2244	2344	2035	2234	2098
	7	1731	2066	1992	2045	2183
	6	1458	1713	2379	1806	2066
	5	1808	2489	2432	2465	2281
	4	2125	2162	1877	1888	1361
	3	2432	2413	2015	1988	1685
	2	2340	2484	2676	2561	2034
	1	2386	2431	2326	2364	2407

Table D.5 – FWD Results on Small Scale Study

Section	Point	Geophone S1 Deflection (mils)			Modulus, ksi		
		Line 1	Line 3	Line 5	Line 1	Line 3	Line 5
S10, Deep and Full Debonding	5	5.0	5.1	8.7	990	914	307
	3	5.5	5.1	9.8	741	899	252
	1	5.3	5.1	9.3	835	876	265
S9, Deep and Partial Debonding	5	4.9	5.4	7.3	898	689	409
	3	4.4	4.8	6.7	1085	881	458
	1	5.2	4.8	5.6	759	856	692
S8, Shallow and Full Debonding	5	5.1	6.8	8.2	849	380	228
	3	5.3	5.5	6.4	749	628	357
	1	5.5	5.7	5.6	697	598	495
S7, Shallow and Partial Debonding	5	5.2	6.4	6.0	784	451	489
	3	5.2	6.5	5.7	862	282	619
	1	5.5	5.3	5.7	856	903	685
S6, Intact Area	5	5.6	5.2	5.3	804	946	815
	3	5.7	4.9	5.8	749	1073	619
	1	5.2	5.0	5.2	876	927	869
Transition	5	5.7	5.3	N/A	N/A	N/A	N/A
	4	6.3	5.4	N/A	N/A	N/A	N/A
	3	6.2	7.9	16.7	N/A	N/A	N/A
	2	4.8	12.5	N/A	N/A	N/A	N/A
	1	4.4	4.5	N/A	N/A	N/A	N/A
S5, Deep and Full Debonding	5	4.5	5.2	6.7	1008	786	487
	3	4.1	5.1	7.6	1279	871	346
	1	4.2	4.7	7.4	1273	1081	374
S4, Deep and Partial Debonding	5	3.9	4.7	7.0	1606	1184	527
	3	4.1	5.3	6.3	1375	920	741
	1	5.0	5.9	8.1	912	763	408
S3, Shallow and Full Debonding	5	4.7	6.8	11.6	1091	524	195
	3	5.5	6.3	10.0	783	672	244
	1	5.4	5.6	8.9	918	870	328
S2, Shallow and Partial Debonding	5	5.2	5.7	7.6	916	846	493
	3	5.7	6.0	6.9	757	749	660
	1	5.6	5.6	6.9	812	877	675
S1, Intact	5	4.7	5.1	5.9	1306	1108	1046
	3	4.6	5.0	6.7	1289	1080	769
	1	4.9	5.1	7.0	1093	989	692

Table D.6 – LWD Results on Small Scale Study. Coarse Mix

Section	Point	Geophone Deflection (mils)					Modulus, ksi				
		Line 1	Line 2	Line 3	Line 4	Line 5	Line 1	Line 2	Line 3	Line 4	Line 5
S5, Deep and Full Debonding	5	9.4	7.8	9.1	8.8	9.1	21.4	19.2	19.5	23.8	18.0
	4	8.0	8.9	8.8	7.2	9.5	20.0	15.2	19.9	22.7	16.4
	3	8.6	11.3	8.6	7.6	10.5	20.7	16.7	18.7	19.9	17.4
	2	8.3	10.2	9.2	8.6	9.8	19.5	21.2	21.8	16.4	23.0
	1	8.8	8.1	7.9	10.4	7.4	19.3	18.2	22.0	18.9	19.5
S4, Deep and Partial Debonding	5	7.8	11.5	9.6	8.5	8.9	22.1	14.8	17.3	19.7	17.8
	4	7.7	11.5	9.9	8.7	9.7	22.3	15.7	17.9	19.0	13.1
	3	12.8	10.9	9.6	9.0	13.1	13.4	21.3	16.5	22.7	15.0
	2	7.7	9.1	10.4	7.6	11.4	22.3	18.8	16.7	19.5	18.1
	1	11.7	7.8	10.3	8.8	9.5	14.6	22.0	7.7	17.8	20.1
S3, Shallow and Full Debonding	5	8.2	9.8	9.1	10.5	13.0	21.0	17.5	18.9	16.3	13.1
	4	7.5	10.9	8.5	9.0	9.4	22.8	15.7	20.1	19.0	18.3
	3	7.2	11.4	10.6	9.2	8.5	23.8	15.1	16.2	18.7	20.0
	2	7.3	9.5	10.2	9.3	8.9	23.4	18.0	16.7	18.5	19.2
	1	6.8	10.5	8.6	10.4	7.3	25.1	16.3	19.9	16.5	23.4
S2, Shallow and Partial Debonding	5	6.4	9.3	11.0	7.5	8.8	26.7	18.5	15.6	22.9	19.5
	4	6.5	11.4	10.9	10.5	9.8	26.4	15.0	15.8	16.4	17.5
	3	6.5	11.4	10.1	8.9	8.4	26.5	15.0	16.9	19.2	20.5
	2	6.9	10.7	10.7	7.0	8.4	25.0	16.0	16.1	24.4	20.5
	1	7.6	11.3	9.0	9.5	8.9	22.5	15.2	19.1	18.1	19.2
S1, Intact	5	8.1	9.3	10.4	7.2	7.9	21.2	18.4	16.5	23.6	21.8
	4	7.6	10.4	10.5	7.5	8.9	22.7	16.5	16.4	22.9	19.2
	3	7.9	10.3	8.9	8.5	8.7	21.6	16.7	19.3	20.1	19.6
	2	8.7	11.5	9.2	9.2	7.6	19.6	14.9	18.6	18.7	22.7
	1	8.7	10.5	8.9	9.1	8.5	19.7	16.4	19.3	18.8	20.2

Table D.7 – LWD Results on Small Scale Study. Fine Mix and Transition

Section	Point	Geophone Deflection (mils)					Modulus, ksi				
		Line 1	Line 2	Line 3	Line 4	Line 5	Line 1	Line 2	Line 3	Line 4	Line 5
S10, Deep and Full Debonding	5	7.1	6.9	10.1	9.3	9.0	24.0	24.9	17.0	18.4	19.1
	4	9.5	8.6	10.0	9.9	10.5	18.1	19.9	17.1	17.3	16.4
	3	8.6	8.0	8.6	9.8	11.1	20.0	21.5	20.0	17.4	15.4
	2	11.2	13.5	9.9	9.2	11.3	15.3	12.7	17.3	18.7	15.2
	1	8.5	9.7	10.2	6.3	9.6	20.2	17.7	16.9	27.2	17.8
S9, Deep and Partial Debonding	5	10.2	11.0	14.6	6.6	9.8	16.7	15.6	11.7	25.9	17.5
	4	8.6	10.4	10.1	6.8	11.1	19.7	16.4	17.0	25.1	15.5
	3	9.7	10.2	10.2	5.5	9.7	17.7	16.8	16.8	31.3	17.7
	2	8.4	10.0	9.5	5.9	7.8	20.3	17.1	18.0	28.8	22.0
	1	10.9	10.5	9.0	6.7	9.0	15.7	16.4	19.0	25.7	19.1
S8, Shallow and Full Debonding	5	10.5	10.8	8.7	9.6	14.3	16.4	15.9	19.7	17.9	12.0
	4	9.9	10.6	11.0	8.9	10.7	17.3	16.1	15.5	19.2	16.1
	3	11.0	10.7	9.8	8.9	11.2	15.6	15.9	17.5	19.3	15.3
	2	13.5	13.5	11.1	6.9	9.7	12.6	12.6	15.4	24.9	17.7
	1	12.9	11.5	10.3	8.6	8.5	13.3	14.8	16.6	20.0	20.1
S7, Shallow and Partial Debonding	5	9.6	9.3	9.0	8.1	10.4	17.8	18.5	19.1	21.1	16.5
	4	12.1	9.8	9.0	7.2	8.1	14.2	17.5	19.0	23.8	21.1
	3	10.1	11.7	10.8	7.8	8.6	16.9	14.7	15.9	21.9	19.9
	2	12.0	10.9	8.0	8.0	7.9	14.3	15.8	21.3	21.3	21.8
	1	11.9	10.5	10.4	8.1	9.3	14.4	16.4	16.5	21.2	18.4
S6, Intact	5	8.4	11.1	7.8	7.4	13.2	20.4	15.4	21.9	23.1	12.9
	4	12.4	9.7	9.5	8.2	8.5	13.9	17.6	18.0	20.8	20.2
	3	11.2	9.5	7.7	8.6	8.7	15.3	18.0	22.3	20.0	19.7
	2	10.9	10.2	8.6	7.7	8.8	15.7	16.8	20.0	22.2	19.5
	1	11.2	9.1	9.0	7.2	7.9	15.3	18.8	19.0	23.9	21.6
Transition	8	10.4	9.4	9.3	8.9	10.7	16.4	18.2	18.5	19.2	16.1
	7	10.9	9.6	10.3	7.6	8.7	15.6	17.8	16.7	22.4	19.7
	6	10.2	7.4	8.3	6.9	6.9	16.8	23.0	20.6	24.9	25.0
	5	10.5	9.0	7.6	7.2	7.9	16.4	19.0	22.7	23.6	21.8
	4	9.5	10.0	12.0	15.1	7.4	18.1	17.1	14.3	11.4	23.0
	3	9.5	9.1	9.8	15.2	15.9	18.0	18.9	17.5	11.2	10.8
	2	8.2	10.0	7.6	8.4	8.5	20.8	17.1	22.4	20.3	20.1
	1	8.7	9.7	8.7	8.2	9.3	19.7	17.7	19.6	21.0	18.4

Table D.8 – IR Results (Voltage) on Small Scale Study. Coarse Mix

Section	Point	Hammer Voltage, volts					Geophone Voltage, volts				
		Line 1	Line 2	Line 3	Line 4	Line 5	Line 1	Line 2	Line 3	Line 4	Line 5
S5, Deep and Full Debonding	5	3.16	3.10	2.69	2.98	3.05	0.59	0.72	0.66	0.76	0.81
	4	2.94	3.18	3.11	3.14	2.74	0.65	0.69	0.69	0.80	0.85
	3	3.23	2.46	3.08	2.64	2.99	0.66	0.64	0.71	0.76	0.84
	2	3.31	2.90	3.52	2.64	3.41	0.65	0.61	0.70	0.76	0.88
	1	3.29	3.52	3.44	3.31	3.10	0.64	0.66	0.70	0.75	0.82
S4, Deep and Partial Debonding	5	3.36	2.77	3.32	2.65	2.84	0.61	0.57	0.62	0.65	0.76
	4	3.11	3.20	3.59	2.76	3.16	0.62	0.65	0.68	0.70	0.78
	3	3.04	2.68	3.29	2.85	3.11	0.60	0.63	0.69	0.66	0.69
	2	3.20	2.52	3.07	3.38	3.40	0.62	0.64	0.68	0.72	0.73
	1	2.87	3.25	3.00	3.10	3.54	0.75	0.71	0.71	0.77	0.88
S3, Shallow and Full Debonding	5	3.46	3.10	2.88	3.32	3.43	0.64	0.71	0.72	0.92	0.97
	4	3.34	3.37	3.10	3.26	3.32	0.64	0.76	0.77	0.95	1.00
	3	3.58	3.31	3.18	2.92	3.22	0.67	0.66	0.74	0.80	0.83
	2	3.69	3.56	2.53	3.01	3.52	0.67	0.69	0.70	0.79	0.82
	1	3.39	2.98	2.81	3.44	2.94	0.65	0.60	0.71	0.77	0.77
S2, Shallow and Partial Debonding	5	3.20	2.91	3.13	3.06	3.19	0.62	0.59	0.63	0.68	0.74
	4	2.97	3.03	3.14	3.33	2.90	0.61	0.66	0.65	0.68	0.64
	3	2.87	3.25	3.38	3.57	2.90	0.62	0.60	0.63	0.69	0.67
	2	3.24	3.42	3.31	3.34	3.64	0.63	0.65	0.64	0.70	0.71
	1	2.86	3.27	3.00	3.68	3.16	0.64	0.62	0.62	0.67	0.63
S1, Intact	5	4.10	2.44	2.57	3.29	2.96	0.61	0.52	0.56	0.59	0.61
	4	2.61	2.42	2.89	3.46	3.57	0.48	0.51	0.56	0.64	0.63
	3	2.53	2.31	3.23	2.88	3.57	0.51	0.51	0.60	0.64	0.65
	2	2.42	2.40	3.21	3.25	3.75	0.51	0.51	0.57	0.63	0.66
	1	3.05	2.39	2.80	3.34	3.33	0.54	0.53	0.57	0.62	0.67

Table D.9 – IR Results (Voltage) on Small Scale Study. Fine Mix and Transition

Section	Point	Hammer Voltage, volts					Geophone Voltage, volts				
		Line 1	Line 2	Line 3	Line 4	Line 5	Line 1	Line 2	Line 3	Line 4	Line 5
S10, Deep and Full Debonding	5	3.37	3.65	3.65	3.75	3.17	0.60	0.65	0.71	0.71	0.76
	4	3.22	3.19	2.91	3.41	3.29	0.59	0.64	0.64	0.72	0.71
	3	3.77	4.15	3.85	3.35	3.11	0.62	0.64	0.65	0.69	0.77
	2	3.46	3.80	3.83	3.47	2.88	0.64	0.61	0.66	0.70	0.75
	1	3.30	3.33	3.64	3.24	2.93	0.63	0.61	0.63	0.66	0.69
S9, Deep and Partial Debonding	5	3.62	3.52	3.13	3.25	3.05	0.56	0.59	0.65	0.75	0.72
	4	3.63	3.33	3.06	2.94	3.33	0.53	0.58	0.55	0.70	0.65
	3	3.37	3.83	3.82	3.03	3.29	0.56	0.57	0.62	0.68	0.58
	2	3.55	3.59	3.87	2.89	3.17	0.59	0.60	0.60	0.73	0.63
	1	3.48	3.33	3.55	3.23	3.41	0.56	0.57	0.60	0.60	0.66
S8, Shallow and Full Debonding	5	3.41	2.97	3.60	3.45	2.86	0.58	0.63	0.67	0.75	0.73
	4	3.74	3.05	3.32	4.11	3.14	0.59	0.71	0.69	0.77	0.93
	3	2.86	3.24	2.93	3.50	3.02	0.57	0.61	0.61	0.66	0.67
	2	3.30	2.76	3.56	3.14	2.50	0.63	0.63	0.71	0.64	0.68
	1	3.36	3.23	3.23	4.16	3.69	0.61	0.65	0.72	0.76	0.73
S7, Shallow and Partial Debonding	5	3.47	3.25	2.78	3.20	2.96	0.63	0.64	0.67	0.71	0.65
	4	3.33	4.06	3.34	3.09	2.81	0.60	0.69	0.70	0.65	0.63
	3	2.93	3.46	3.36	3.55	3.76	0.61	0.65	0.65	0.63	0.63
	2	3.21	3.51	2.72	3.31	3.76	0.62	0.64	0.62	0.65	0.63
	1	3.08	3.51	3.58	3.35	3.40	0.62	0.64	0.65	0.63	0.61
S6, Intact	5	3.82	3.72	3.88	3.42	3.72	0.63	0.69	0.65	0.66	0.66
	4	3.36	3.42	3.88	3.07	3.85	0.62	0.63	0.65	0.62	0.65
	3	3.55	3.31	3.07	3.38	3.57	0.62	0.63	0.63	0.63	0.68
	2	3.25	3.43	4.02	3.16	3.49	0.61	0.64	0.67	0.65	0.67
	1	2.80	3.09	2.92	3.64	3.38	0.59	0.64	0.68	0.66	0.67
Transition	8	2.88	3.13	3.03	3.32	3.56	0.58	0.63	0.68	0.65	0.66
	7	3.04	2.99	3.61	2.97	3.58	0.60	0.61	0.65	0.67	0.63
	6	2.97	2.95	3.33	3.48	3.34	0.62	0.64	0.69	0.70	0.64
	5	3.06	3.30	2.86	3.52	3.40	0.62	0.63	0.65	0.66	0.72
	4	3.50	3.54	2.94	2.96	3.03	0.60	0.64	0.93	2.68	1.17
	3	2.91	2.70	3.39	2.74	3.13	0.57	0.61	1.77	2.79	1.36
	2	3.32	3.21	3.05	3.67	3.45	0.58	0.62	0.63	0.59	0.65
	1	3.34	3.35	3.48	3.32	3.41	0.59	0.62	0.62	0.62	0.64

Table D.10 – IR Results (FFT) on Small Scale Study. Coarse Mix

Section	Point	Maximum Amplitude FFT Hammer					Maximum Amplitude FFT Geophone				
		Line 1	Line 2	Line 3	Line 4	Line 5	Line 1	Line 2	Line 3	Line 4	Line 5
S5, Deep and Full Debonding	5	14.5	18.7	15.7	16.6	16.8	6.7	11.1	7.7	9.1	11.2
	4	16.6	15.0	15.9	16.5	14.7	8.9	8.9	8.0	10.5	12.6
	3	17.3	13.9	16.5	14.9	15.9	8.2	8.1	8.3	9.3	10.2
	2	16.7	13.7	17.8	14.9	17.6	8.3	6.8	8.0	9.3	12.4
	1	15.4	18.2	18.3	16.3	16.1	7.2	8.9	8.4	7.9	9.5
S4, Deep and Partial Debonding	5	17.4	13.3	17.3	13.4	15.7	7.0	5.7	6.9	6.2	9.2
	4	15.3	15.4	16.6	15.3	14.8	6.3	7.6	7.0	7.6	8.2
	3	15.0	15.0	17.1	16.4	15.1	6.3	9.4	9.1	8.0	7.0
	2	15.2	14.1	17.7	15.4	17.9	6.6	8.8	9.5	8.2	8.7
	1	13.6	15.9	18.1	16.6	16.6	7.5	8.4	10.2	10.6	11.2
S3, Shallow and Full Debonding	5	18.0	15.1	15.9	16.9	17.9	7.9	9.2	8.9	17.6	17.2
	4	16.8	18.2	16.4	15.7	16.5	6.6	11.3	10.0	18.6	17.0
	3	15.8	14.9	15.3	14.8	15.3	6.6	7.6	10.5	10.7	11.3
	2	17.1	17.5	14.2	15.9	18.1	7.1	8.3	9.7	12.4	12.7
	1	15.2	15.1	15.5	17.3	17.1	7.0	7.1	8.4	10.0	9.1
S2, Shallow and Partial Debonding	5	14.4	12.9	18.0	15.5	15.3	6.4	5.6	8.3	8.2	7.3
	4	13.3	17.6	14.0	15.6	16.5	6.4	11.0	6.8	7.9	7.1
	3	16.2	16.4	16.7	16.2	16.1	8.4	9.1	7.8	7.8	7.6
	2	14.4	15.5	15.7	16.6	15.9	8.3	8.4	8.2	9.1	8.5
	1	13.5	17.7	14.2	17.4	16.4	8.3	9.2	7.4	8.8	7.9
S1, Intact	5	19.9	11.6	11.1	14.7	13.5	7.6	6.1	6.4	6.8	5.7
	4	11.6	11.9	13.7	15.2	16.7	5.5	5.6	6.3	6.6	7.4
	3	11.3	10.3	15.3	15.0	15.7	5.8	5.2	6.9	8.4	7.5
	2	11.5	11.4	13.7	14.7	16.8	6.1	5.7	6.1	5.8	5.9
	1	12.9	11.0	14.6	14.1	17.2	5.2	5.7	6.3	5.3	7.1

Table D.11 – IR Results (FFT) on Small Scale Study. Fine Mix and Transition

Section	Point	Maximum Amplitude FFT Hammer					Maximum Amplitude FFT Geophone				
		Line 1	Line 2	Line 3	Line 4	Line 5	Line 1	Line 2	Line 3	Line 4	Line 5
S10, Deep and Full Debonding	5	14.0	17.9	16.9	17.2	14.2	5.9	8.3	8.1	9.6	12.1
	4	15.6	14.9	13.4	15.2	15.5	6.8	8.2	7.5	9.0	10.4
	3	16.9	16.8	16.5	14.8	14.0	7.7	7.3	7.4	11.1	10.7
	2	15.7	17.3	16.1	15.5	16.6	8.8	8.0	7.1	9.9	14.6
	1	14.4	14.2	16.1	14.1	14.5	7.9	6.9	7.1	9.0	11.1
S9, Deep and Partial Debonding	5	15.1	16.4	14.9	14.2	15.8	5.7	7.2	8.2	10.6	12.2
	4	15.0	14.4	14.3	14.4	13.9	5.4	6.4	6.5	9.1	8.5
	3	16.1	15.7	19.4	14.3	14.7	8.0	6.0	8.1	8.0	6.9
	2	14.7	17.6	15.7	14.0	15.4	7.4	8.4	7.5	8.4	8.1
	1	14.3	16.3	16.4	16.4	15.4	6.5	6.9	7.8	7.9	8.4
S8, Shallow and Full Debonding	5	15.8	14.1	18.4	17.2	12.7	6.1	8.9	11.0	11.7	10.0
	4	17.5	14.4	18.1	17.3	15.2	6.8	10.3	12.1	12.0	16.8
	3	14.3	14.0	15.1	16.0	16.2	5.7	5.9	7.2	9.6	11.3
	2	14.4	13.8	14.8	14.1	16.1	5.8	7.5	9.3	8.0	14.0
	1	15.0	15.8	16.3	18.4	16.1	5.9	6.3	9.6	10.6	10.1
S7, Shallow and Partial Debonding	5	16.9	18.0	14.5	15.0	15.5	6.8	6.4	7.7	9.1	8.7
	4	15.9	18.5	14.8	16.6	14.2	5.9	6.3	6.4	9.3	8.2
	3	16.1	17.2	16.3	17.0	16.6	7.2	6.4	7.1	7.0	6.7
	2	17.4	15.0	14.6	14.0	16.6	7.2	5.6	7.2	6.4	6.7
	1	14.2	16.8	17.7	17.8	16.3	6.4	6.1	8.2	9.1	8.1
S6, Intact	5	15.9	18.7	18.0	15.2	16.9	5.3	7.2	8.3	7.1	7.8
	4	15.7	14.5	18.0	14.1	16.2	5.4	6.5	8.3	6.6	6.5
	3	15.9	15.2	13.9	18.3	15.2	5.6	6.7	6.9	8.1	6.7
	2	13.7	15.6	18.1	14.7	17.1	5.3	6.3	8.1	6.5	7.4
	1	12.6	13.7	14.4	16.3	15.4	4.7	5.3	7.6	7.4	7.4
Transition	8	16.1	13.4	16.0	13.9	17.1	6.3	5.4	8.4	6.5	7.5
	7	12.6	16.8	16.7	14.0	17.5	4.8	6.6	6.6	7.7	7.3
	6	15.0	14.7	17.0	15.0	15.8	6.6	6.3	6.8	6.7	6.6
	5	13.1	16.3	13.4	17.5	16.9	5.5	7.0	7.9	6.8	7.4
	4	13.9	16.7	12.6	14.6	18.3	5.9	6.9	30.3	163.6	42.9
	3	15.5	12.5	16.1	16.0	15.2	6.8	6.1	61.4	173.8	41.3
	2	14.6	14.4	15.2	16.2	16.9	6.0	6.0	7.1	5.5	7.5
	1	14.4	18.8	18.8	16.8	14.8	6.0	7.4	7.2	7.2	7.2

Table D.12 – Geogauge Results on Small Scale Study. Coarse Mix

Section	Point	Modulus, ksi					Signal to Noise Ratio, ksi				
		Line 1	Line 2	Line 3	Line 4	Line 5	Line 1	Line 2	Line 3	Line 4	Line 5
S5, Deep and Full Debonding	5	27.6	54.9	55.9	54.6	41.2	39.6	39.8	44.0	41.4	45.6
	4	72.2	65.2	63.1	69.7	38.8	40.7	42.4	39.5	36.7	40.7
	3	32.4	71.8	28.4	65.3	47.7	42.2	41.4	40.9	33.2	41.5
	2	64.5	32.3	48.8	44.5	57.7	36.6	44.4	39.4	40.1	40.7
	1	35.4	65.6	53.2	65.4	64.7	45.5	40.3	48.2	36.6	47.0
S4, Deep and Partial Debonding	5	60.0	31.7	38.3	51.4	48.4	31.9	45.9	39.9	42.4	43.6
	4	43.2	47.5	42.7	32.4	54.0	41.4	44.0	39.3	40.9	18.8
	3	53.5	37.6	56.8	44.9	39.1	32.4	46.8	41.7	40.2	43.6
	2	46.5	63.3	51.1	47.0	46.0	36.9	37.4	36.4	42.8	33.8
	1	69.3	65.8	35.1	49.1	38.8	38.3	40.3	45.0	43.3	47.2
S3, Shallow and Full Debonding	5	57.5	59.1	33.6	48.6	36.2	35.6	40.9	43.5	42.2	45.6
	4	69.2	77.4	54.4	40.5	46.2	37.2	36.7	42.2	42.4	42.6
	3	67.6	43.1	57.7	39.2	26.6	39.5	39.5	40.1	39.3	49.9
	2	45.5	47.1	42.7	51.2	38.9	40.9	45.0	44.4	41.8	46.2
	1	65.2	40.8	54.3	31.1	37.8	35.3	41.9	38.1	46.8	47.0
S2, Shallow and Partial Debonding	5	60.4	43.3	44.2	65.5	52.6	39.9	42.8	44.0	39.9	41.7
	4	24.7	51.6	51.4	50.4	74.6	46.1	37.8	38.3	41.8	35.0
	3	54.5	35.6	48.8	61.4	47.1	36.6	43.7	42.5	36.5	41.3
	2	32.1	33.7	30.4	71.6	45.4	41.7	44.7	50.5	35.7	43.3
	1	70.0	35.1	46.8	72.6	50.2	40.3	39.5	40.3	39.1	37.5
S1, Intact	5	63.6	43.8	30.8	60.1	44.6	39.2	40.6	34.3	38.6	39.1
	4	64.9	63.6	52.6	51.6	56.8	36.6	40.0	41.4	44.2	41.3
	3	55.8	56.2	48.0	44.0	51.6	38.6	42.0	41.6	43.7	40.8
	2	78.2	50.0	54.6	61.9	48.9	38.3	42.8	37.9	38.6	41.3
	1	58.4	49.6	57.8	80.0	75.9	41.1	38.8	40.4	38.3	47.5

Table D.13 – Geogauge Results on Small Scale Study. Fine Mix and Transition

Section	Point	Modulus, ksi					Signal to Noise Ratio, ksi				
		Line 1	Line 2	Line 3	Line 4	Line 5	Line 1	Line 2	Line 3	Line 4	Line 5
S10, Deep and Full Debonding	5	64.6	63.6	63.0	51.6	59.9	41.0	39.8	37.1	31.0	39.8
	4	47.4	39.1	43.4	62.5	90.1	44.9	39.6	36.0	37.0	39.7
	3	52.6	26.8	61.8	59.9	54.8	41.2	35.7	26.6	44.0	35.7
	2	38.6	65.9	55.1	48.4	45.8	40.2	39.9	31.7	36.4	39.9
	1	47.5	44.7	52.7	26.1	59.2	39.0	35.7	39.9	41.8	34.7
S9, Deep and Partial Debonding	5	65.6	58.8	51.8	40.8	40.2	41.8	45.9	37.0	15.6	43.1
	4	65.7	45.1	50.2	55.9	44.2	41.3	40.8	43.3	41.1	41.3
	3	47.1	61.8	57.2	39.0	60.3	45.0	49.4	42.6	42.5	41.7
	2	64.5	42.6	66.8	44.7	31.6	37.9	40.0	35.2	43.6	39.0
	1	34.6	60.9	39.9	49.1	43.3	40.1	39.8	42.3	38.9	48.8
S8, Shallow and Full Debonding	5	43.1	62.7	46.3	44.6	49.3	38.4	39.1	38.6	47.2	42.2
	4	50.6	54.4	57.9	46.1	36.1	43.1	40.9	39.5	40.7	41.3
	3	59.4	49.0	42.8	39.5	46.0	42.1	43.1	39.3	41.4	43.3
	2	38.1	51.6	46.6	56.5	62.5	45.9	39.3	42.5	41.3	39.0
	1	45.5	49.0	50.8	46.3	50.5	43.6	44.4	49.2	45.1	43.6
S7, Shallow and Partial Debonding	5	45.5	51.0	36.2	58.4	47.4	38.5	42.3	38.6	44.5	40.3
	4	63.7	42.3	44.0	61.7	41.7	32.5	36.7	33.2	42.0	37.9
	3	38.3	49.2	56.5	68.1	57.5	44.6	48.2	40.4	43.5	45.6
	2	39.5	69.6	33.8	57.2	51.6	13.5	34.6	41.9	41.6	40.1
	1	41.6	49.4	38.3	93.7	58.5	41.9	17.1	41.5	35.7	43.5
S6, Intact	5	39.4	72.2	37.3	46.0	72.0	41.2	38.2	42.9	36.8	37.9
	4	52.3	53.6	75.7	76.7	56.8	40.1	37.2	37.6	37.4	32.9
	3	44.0	67.8	66.0	64.1	41.5	42.2	42.9	37.2	34.5	41.6
	2	63.0	62.8	41.3	64.1	73.7	35.3	35.6	38.8	37.5	36.1
	1	42.1	82.9	45.5	56.1	56.4	44.6	35.9	39.7	24.9	42.8
Transition	8	46.3	58.3	55.1	62.0	63.7	29.1	40.7	37.6	43.2	33.2
	7	55.4	51.0	35.0	35.0	35.6	44.1	35.6	40.7	42.1	45.4
	6	41.9	55.7	25.0	64.1	61.9	36.5	43.2	21.7	42.6	36.5
	5	41.3	33.2	50.0	35.7	43.3	44.8	40.5	44.4	41.3	38.8
	4	41.9	70.5	34.7	22.1	23.0	40.2	39.0	39.5	38.9	47.0
	3	73.4	58.7	33.7	35.1	29.2	39.0	37.1	46.6	39.0	39.9
	2	26.6	72.4	51.0	37.0	50.7	43.9	40.5	44.4	38.0	39.8
	1	42.7	49.4	59.8	72.2	58.8	44.9	50.7	39.8	37.8	42.7

Table D.14 – Shear Strength Results (psi) for Cores Retrieved at 2 ft from Start from Small Scale Study

Section #	Interface at 2.5 inches deep			Interface at 5 inches deep		
	Tack Coat	Grease	Talcum Powder	Tack Coat	Grease	Talcum Powder
1	42[a]			86[a]		
2		32[a]		88[a]		
3			0[a,c]	94[a]		
4	82[a]				25[a]	
5	71[a]					0[a,c]
6	84[b]			90[a]		
7		50[b]		63[a]		
8			0[b,c]	96[a]		
9	95[b]				21[a]	
10	91[b]					0[a,c]
Average	78	41	0	86	23	0
COV, %	24.8	32.3	--	13.9	14.1	--

[a] *P403/P401 Interface* ,[b] *P401/P401 Interface*
[c] *Specimen not feasible for shear testing*

Table D.15 – Shear Strength Results (psi) for Cores Retrieved at 7 ft from Start from Small Scale Study

Section #	Interface at 2.5 inches deep			Interface at 5 inches deep		
	Tack Coat	Clay Slurry	Paper Soaked in Oil	Tack Coat	Clay Slurry	Paper Soaked in Oil
1	74[a]			78[a]		
2		0[a,c]		86[a]		
3			0[a,c]	76[a]		
4	88[a]				0[a,c]	
5	75[a]					0[a,c]
6	97[b]			93[a]		
7		30[a]		78[a]		
8			0[b,c]	84[a]		
9	88[b]				0[b,c]	
10	97[b]					0[b,c]
Average	87	30	0	83	0	0
COV, %	11.7	141.4	--	7.8	--	--

[a] *P403/P401 Interface*
[b] *P401/P401 Interface*
[c] *Specimen not feasible for shear testing*

APPENDIX E

COMPLETE NDT RESULTS OF EXTENDED TESTS ON SMALL SCALE STUDY

Table E.1 – PSPA Results on Small Scale Study (3 Lifts Combined). Fine Mix and Transition (Cool Weather)

Section	Point	Seismic Modulus from PSPA (for 8 in), ksi									
		Line 1	Line 2	Line 3	Line 4	Line 5	Line 6	Line 7	Line 8	Line 9	Line 10
S10, Deep and Full Debonding	10	1736	1794	2061	1986	2114	2526	1799	1759	1629	1724
	9	1807	1740	2074	2152	2298	2549	1553	1745	1610	1566
	8	1598	1792	2207	2029	2228	2353	1641	1817	1505	1625
	7	1696	1630	1981	2304	2213	2436	1828	1629	1572	1664
	6	1595	1695	2100	2369	2482	2342	1859	1869	1408	1697
	5	1722	1967	2042	2169	2110	2429	1463	1864	1413	1454
	4	1756	1946	1992	1901	2034	2146	1499	1807	1447	1368
	3	1696	1764	2000	2278	1615	2445	1744	1431	1341	1626
	2	1647	1706	1790	1874	2178	2304	1602	1564	1569	1577
	1	1595	1840	1941	1866	1879	2172	1916	1697	1395	1629
S9, Deep and Partial Debonding	10	1888	1880	1838	1609	2147	1663	2000	1607	1506	1620
	9	1795	1785	1944	1697	1892	1995	1878	1981	1547	1460
	8	1737	1683	1960	1804	1887	2071	1798	1993	1578	1584
	7	2071	1724	1867	1627	1934	1799	1797	1758	1567	1535
	6	1898	1898	1812	1774	1594	1942	1806	2094	1435	1580
	5	2041	1862	1759	1997	1768	2019	1986	2101	1734	1610
	4	1845	2045	2088	1798	1775	1845	2189	2137	1758	1848
	3	1884	1929	1698	1774	1575	1907	1678	1920	1684	1702
	2	2044	2006	1823	1720	2060	1942	1840	2057	1725	1675
	1	1862	1974	1957	1862	1869	1855	1427	1385	1252	1197
S8, Shallow and Full Debonding	10	2015	1927	1237	1540	1227	2209	1421	1646	1426	1511
	9	1781	1731	1241	1483	1606	2217	1661	1441	1300	1249
	8	1633	1417	1704	1564	1851	1974	1598	1566	1513	1416
	7	1599	1448	1655	1824	1414	2367	1531	1720	1413	1466
	6	1623	1582	1792	1894	1876	2396	1534	1701	1453	1573
	5	1774	1907	1887	1869	1806	2197	1555	1709	1493	1501
	4	1914	2016	2001	1780	1588	2090	1449	1700	1503	1575
	3	1903	1877	1729	1719	1510	1813	1329	1608	1273	1480
	2	1732	1837	1680	1887	1711	1967	1686	1490	1484	1561
	1	1563	1771	1604	1755	2013	2062	1465	1579	1613	1576
S7, Shallow and Partial Debonding	10	1894	1677	1378	1412	1571	1780	1801	1642	1650	1510
	9	1899	1873	1863	1715	1701	2055	1669	1728	1717	1615
	8	1794	1827	1935	2219	1990	1984	1938	1640	1713	1443
	7	1755	1791	1875	1905	1884	1918	1841	1781	1817	1744
	6	1665	1685	1716	2171	1831	1993	1906	1669	1873	1685
	5	1938	1992	1791	2141	2037	2013	1775	1809	1693	1609
	4	1997	1780	1779	2011	2015	1861	1981	1860	1777	1799
	3	1876	1884	1686	2148	1938	1751	1764	1711	1737	1748
	2	1705	1968	2036	1976	2035	2019	1815	1727	1873	1733
	1	1778	1955	2085	1995	2336	2104	1704	1889	1963	1949

Table E.1 Contd. – PSPA Results on Small Scale Study (3 Lifts Combined). Fine Mix and

Transition (Cool Weather)

	10	1784	1985	2227	2341	2206	1549	2063	1974	2261	2093
	9	1861	2235	1951	2282	1974	1871	1915	2193	2110	1996
	8	1821	2198	2399	2583	2236	1921	1797	2022	2100	1997
	7	1938	2013	2054	2293	2182	1922	1940	1943	2215	1966
S6, Intact	**6**	2038	1943	2386	2479	2353	1766	2004	2119	2143	2176
	5	2111	2044	2063	2600	2440	2211	1975	2052	2117	1834
	4	2220	2349	2183	2584	2322	2257	1995	2247	2193	2166
	3	2079	2273	2382	2113	2378	2498	2047	2109	2243	2121
	2	2091	2083	2093	2456	2234	2945	1814	1943	1827	1896
	1	1454	1673	1761	2202	2486	2448	1879	2061	1947	1969
	15	1342	1422	1530	2118	2237	2060	2123	2151	1840	1883
	14	1487	1658	1577	1804	2149	2963	1977	1875	1982	1998
	13	1462	1395	1488	1896	1815	2271	2059	2106	1971	1807
	12	1332	1577	1658	1633	1418	1922	2358	1864	1820	1926
	11	1145	1423	1527	1624	1932	2227	1739	1868	1783	1760
	10	1422	1363	1746	1821	1663	2287	2310	1965	1664	1622
	9	1080	1398	1823	1754	1508	1962	1842	1913	1942	1824
TRANSITION	**8**	1553	1852	2120	1996	1244	1252	1113	1173	1136	963
	7	1871	2118	2129	1874	1442	1119	1002	954	1051	1149
	6	1917	2135	2069	2075	1173	1319	1192	1048	1116	994
	5	1944	2047	2347	2321	1183	1286	1216	1226	1144	1026
	4	1771	2233	1890	2279	1446	1982	1846	2149	1720	1947
	3	1718	2057	1945	1960	2166	1911	2140	2173	1620	1989
	2	1690	1936	1952	2092	2059	1928	2097	2067	1820	1717
	1	1852	2067	2012	2156	1788	1802	1820	2433	2084	2004

Table E.2 – PSPA Results on Small Scale Study (3 Lifts Combined). Coarse Mix (Cool Weather)

Section	Point	Seismic Modulus from PSPA (for 8 in), ksi									
		Line 1	Line 2	Line 3	Line 4	Line 5	Line 6	Line 7	Line 8	Line 9	Line 10
S5, Deep and Full Debonding	10	1678	1755	1890	1911	1908	1693	1987	1864	1761	1684
	9	1916	2001	2146	1870	1637	1690	1724	1935	1697	1600
	8	1829	1889	2006	1546	1765	1727	1579	1699	1569	1493
	7	2006	1855	2029	1809	1785	1800	1671	1636	1756	1695
	6	2243	1926	1976	1512	1691	1725	1727	1805	1824	1484
	5	2053	1921	1841	1718	1618	1814	1927	1940	1736	1754
	4	1881	2138	1859	1456	1750	1786	1749	1894	1660	1778
	3	1955	1835	1867	1982	1888	1847	1695	1942	1726	1754
	2	2244	2088	1869	1750	2062	1998	1946	1701	1635	1814
	1	2056	1831	1883	1496	1993	1740	1912	1467	1595	1806
S4, Deep and Partial Debonding	10	1859	1928	1762	1655	1948	1776	1731	1825	1609	1700
	9	2141	1892	1862	1765	1856	2070	1873	1693	1551	1608
	8	1862	1734	1861	1612	1670	1591	1837	1517	1616	1712
	7	2039	1808	1794	1640	1875	1827	1561	1698	1572	1723
	6	1767	1854	1796	1431	1495	1494	1753	2052	1663	1849
	5	2039	2130	1712	1269	1778	1832	1772	1757	1623	1475
	4	1692	2137	1777	1457	1486	1941	1843	1835	1641	1190
	3	1849	1951	1804	1659	1649	1749	1926	1609	1000	868
	2	1691	1781	1991	1527	1622	1666	1731	1587	1254	1147
	1	2051	1760	1938	1796	1738	1788	1369	1488	1279	1086
S3, Shallow and Full Debonding	10	2075	1769	1291	1224	1548	1803	1156	1182	1268	1213
	9	1920	1461	1156	1208	1523	1781	1281	1301	1319	1217
	8	1908	1893	1582	1481	1770	2009	1408	1331	1314	1318
	7	1952	1948	1722	1544	1569	1539	1396	1267	1326	1143
	6	1822	1864	1786	1382	1694	1733	1674	1522	1517	1288
	5	1854	1844	1854	1631	2102	1758	1535	1577	1326	1314
	4	1894	1898	1818	1928	2128	1888	1369	1387	1335	1119
	3	1909	2127	1931	1699	2046	2046	1522	1312	1271	1156
	2	1945	2226	1929	1896	2215	2024	1404	1289	1241	1253
	1	1920	2214	1893	1632	1935	1764	1463	1610	1328	1418
S2, Shallow and Partial Debonding	10	2104	1906	1683	1833	1932	2528	1675	1467	1083	1426
	9	2018	2045	1858	1892	2052	2737	2101	1481	1297	1468
	8	1979	2022	1922	1734	2016	1978	2487	1674	1443	1843
	7	1903	2059	1796	1778	1869	2246	1932	1444	1402	1653
	6	1878	1960	1636	1587	1995	2115	2131	1623	1457	1853
	5	1960	1993	1757	1624	2330	2048	2014	1660	1227	1626
	4	1883	2122	1883	1876	1980	2162	1910	1643	1575	1659
	3	1999	2079	1869	1529	2083	2214	1850	1552	1459	1735
	2	1847	1946	1870	1952	2341	1895	2168	1478	1602	1714
	1	2035	1787	1877	1691	2281	2196	2405	1596	1840	1846
S1, Intact	10	2225	2007	1987	1735	1805	1645	1679	1825	1927	1782
	9	2119	1799	2029	1919	1626	1551	1736	1806	1860	1859
	8	2141	2089	2192	1877	1762	1575	1936	1668	1899	1923
	7	2220	1954	1894	1664	1762	1497	1635	1733	1727	1750
	6	2264	1809	1981	1880	1863	1619	1668	1859	1743	1851
	5	1893	1898	1862	1634	1815	1836	1659	1590	1544	1577
	4	2276	1708	1937	1812	2013	1575	1563	1425	1817	1732
	3	1864	1840	1996	1572	1728	1569	1518	1566	1551	1767
	2	2139	2105	1533	1751	1926	1465	1578	1696	1665	1936
	1	1907	1700	1679	1847	1638	1741	1320	1517	1524	1781

Table E.3 – PSPA Results on Small Scale Study (Top Lift). Fine Mix and Transition (Cool Weather)

Section	Point	Seismic Modulus from PSPA (for 2.5 in), ksi									
		Line 1	Line 2	Line 3	Line 4	Line 5	Line 6	Line 7	Line 8	Line 9	Line 10
S10, Deep and Full Debonding	10	1947	2006	2168	2060	2100	2403	2358	2190	2292	2283
	9	1884	1868	2188	2275	2596	2368	2363	2376	2161	2397
	8	1742	1922	2178	2083	2473	2422	2268	2327	2068	2100
	7	1804	2136	2102	2426	2297	2613	2207	2324	1970	2065
	6	1936	1828	2317	2534	2538	2440	2309	2286	2020	2210
	5	1866	2155	2274	2349	2269	2649	2077	2272	1970	1972
	4	2039	2170	2032	2110	2138	2162	2123	2231	1973	2039
	3	1854	2305	2250	2394	1872	2433	2065	2143	1916	2219
	2	2044	1872	2026	2118	2195	2311	2059	2263	2046	2219
	1	1959	2019	2141	2341	2065	2297	2512	2202	1994	2184
S9, Deep and Partial Debonding	10	2158	2009	2009	1899	2205	1767	2226	1907	1878	2079
	9	1956	1910	2176	1874	2132	2122	2109	2164	1835	1981
	8	1866	1858	2039	1944	1933	2212	2083	2116	2128	2041
	7	2210	2043	2118	1845	2143	2088	2083	2222	2039	1903
	6	2152	2187	1916	2177	1746	2277	2266	2317	1826	2096
	5	2159	1984	2129	2127	2029	2184	2272	2321	1961	2289
	4	2070	2351	2090	1815	1896	2240	2417	2287	2028	2137
	3	2102	2090	1766	2020	1718	2012	2070	2313	2099	2071
	2	2198	2216	1761	1821	2053	2202	2300	2451	2112	2054
	1	2041	2085	2003	2123	1945	2157	1900	1747	1878	1789
S8, Shallow and Full Debonding	10	2002	1856	1404	1776	1533	2279	1861	1729	1717	1763
	9	1878	1769	1547	1665	1765	2428	1726	1613	1586	1758
	8	1693	1351	1914	1882	1929	2226	1983	2038	1832	1653
	7	1758	1664	1900	1969	1827	2547	1997	2017	1787	1937
	6	1635	1678	1904	1981	2012	2377	1785	2034	1780	1846
	5	1884	1904	2148	1992	1957	2462	1858	1939	1710	1889
	4	1964	2042	1992	1981	1861	2366	1668	1861	1669	1690
	3	1875	1850	1813	2051	1592	2049	1575	1960	1580	1621
	2	1755	1862	1730	2174	1937	2012	1856	1711	1758	1738
	1	1657	1851	1689	1932	2326	2054	1743	1653	1779	1952
S7, Shallow and Partial Debonding	10	2014	1766	1599	1630	1691	1799	1786	1694	1812	1707
	9	2061	1858	1946	1843	1891	2038	1830	1907	1892	1756
	8	1900	1965	2260	2198	1917	2117	2004	1825	1868	1804
	7	1892	1855	2202	2114	1878	2010	1763	2045	1953	2067
	6	1851	1832	2023	2094	1828	2103	1995	1815	2147	1773
	5	1971	2163	2009	2113	2129	2147	1920	2194	1846	1741
	4	2127	1816	1896	2148	1922	1945	2037	1998	1957	2102
	3	1947	1965	1749	2091	1921	1719	1838	1709	1880	1920
	2	1823	1991	2154	1950	2035	2142	1951	1674	2044	1975
	1	1922	1762	2153	2003	2330	2291	1754	2025	1955	2046
S6, Intact	10	1787	1966	2213	1954	2221	1944	2222	2293	2355	2342
	9	1929	1947	1873	2263	2150	2205	2188	2340	2315	2363
	8	1884	2087	2178	2443	2191	2070	2135	2365	2315	2275
	7	1795	1925	2205	2256	2301	2100	2297	2335	2347	2330
	6	1884	1921	2213	2034	2087	2140	2179	2359	2371	2502
	5	1881	1972	2128	2431	2337	2289	2300	2287	2308	2257
	4	2105	2063	2128	2434	2385	2213	2244	2455	2424	2452
	3	1925	2138	2105	2074	1933	1999	2247	2323	2578	2369
	2	2149	2109	2205	2248	2113	2186	2015	2405	2070	2195
	1	1560	1746	1904	2309	2256	1911	2061	2215	2331	2437

74

Table E.3 Contd. – PSPA Results on Small Scale Study (Top Lift). Fine Mix and Transition

(Cool Weather)

	15	1412	1519	1577	1799	2283	1992	2041	1835	1716	1716
	14	1441	1730	1528	1568	2172	1750	1941	1911	1809	1912
	13	1376	1375	1383	1537	1779	1630	1849	1857	1843	1822
	12	1404	1424	1560	1419	1384	2016	1656	1845	1756	1898
	11	1271	1381	1432	1440	2342	2356	1653	1712	1458	1919
	10	1305	1341	1799	1929	1811	2248	2222	2155	1578	1837
	9	1107	1437	2023	1818	1594	2050	2080	1919	2130	2016
TRANSITION	**8**	1517	1869	2182	2011	1696	1586	1455	1530	1409	1349
	7	1692	2048	2069	1888	2019	1490	1249	1375	1369	1369
	6	2028	2108	2036	2015	1636	1777	1747	1507	1747	1595
	5	1929	1876	2238	2178	1730	1883	1653	1671	1482	1461
	4	1831	1963	1916	1851	1499	2057	2078	2291	1810	1794
	3	1812	2069	2262	1885	2078	2058	2142	2053	1638	1829
	2	1783	1866	1953	2274	2035	2083	2206	2168	1797	1683
	1	1871	2147	2125	2068	1872	1873	1923	2484	1950	2087

Table E.4 – PSPA Results on Small Scale Study (Top Lift). Coarse Mix (Cool Weather)

Section	Point	Seismic Modulus from PSPA (for 2.5 in), ksi									
		Line 1	Line 2	Line 3	Line 4	Line 5	Line 6	Line 7	Line 8	Line 9	Line 10
S5, Deep and Full Debonding	10	1829	2020	2303	1997	2231	1868	2319	2192	1998	2066
	9	2295	2176	2302	2060	1808	1830	2188	2171	1940	1936
	8	1989	1914	2289	1858	2102	1942	1915	2047	1790	1656
	7	2175	2218	2421	2097	2215	2018	2005	1871	2079	1816
	6	2556	2090	2410	1744	1912	1924	2062	2164	2222	1653
	5	2387	2189	2307	1981	1793	2028	2039	2198	2041	2042
	4	2150	2342	2067	1732	1932	2208	2082	2144	2002	2374
	3	2163	2182	2186	2084	2345	2334	2139	2232	2191	2151
	2	2348	2338	2342	1986	2285	2228	2244	2135	2024	2107
	1	2224	2205	2313	1763	2398	2110	1901	1829	1909	2229
S4, Deep and Partial Debonding	10	2079	1899	1948	1709	1802	1960	1916	2108	1988	1966
	9	2100	1927	2051	1897	2026	2071	2021	1972	1970	1874
	8	1940	1885	1941	1874	2097	1882	1918	1755	1917	1972
	7	2027	1863	2021	1752	2063	2136	1899	2043	1902	1922
	6	1942	2090	1914	1740	1866	1722	1989	2194	1959	2120
	5	2193	2114	2040	1502	1892	1968	2000	1859	1938	1787
	4	1691	2269	2106	1617	1595	2139	2103	2223	1952	1492
	3	1938	1961	1950	1823	1767	1838	2139	1830	1482	1189
	2	1785	1824	2081	1600	1655	1840	1902	1758	1710	1711
	1	2085	1827	2008	1795	1848	1976	1777	1956	1724	1552
S3, Shallow and Full Debonding	10	2054	1912	1539	1452	1740	1824	1566	1605	1641	1718
	9	1711	1641	1415	1508	1627	1856	1551	1613	1604	1588
	8	1833	1857	1631	1561	1777	2023	1699	1613	1647	1515
	7	1892	1982	1833	1680	1687	1668	1668	1558	1550	1515
	6	1784	1951	1872	1434	1684	1661	1835	1597	1617	1564
	5	1904	2088	1884	1845	2108	1882	1712	1689	1556	1479
	4	2036	2155	1770	1915	2256	1993	1562	1437	1477	1392
	3	1990	2100	1910	1801	2025	2237	1345	1330	1322	1274
	2	2017	2194	2044	1926	2328	2033	1318	1282	1339	1398
	1	2083	2303	1955	1791	2075	1974	1414	1610	1689	1497
S2, Shallow and Partial Debonding	10	2346	2307	2083	1543	1406	2129	1838	1707	1674	1847
	9	2516	2245	2170	1462	1628	2268	1696	1586	1532	1844
	8	2232	2388	2155	1672	1787	2080	1940	1994	1753	1737
	7	2286	2267	2105	1768	1700	2379	1945	1964	1694	2038
	6	2161	2096	1966	1799	1882	2221	1730	1971	1673	1946
	5	2042	2158	2086	1808	1830	2300	1801	1880	1606	1990
	4	2183	2255	2233	1945	1719	2218	1619	1813	1588	1763
	3	2382	2391	2055	1974	1453	1927	1532	1918	1522	1675
	2	2154	2289	2118	2142	1746	1899	1808	1682	1715	1778
	1	2291	2056	2152	1921	2072	1945	1700	1633	1757	1976
S1, Intact	10	2245	2260	2312	2029	2146	1822	1847	2005	2113	2196
	9	2318	2125	2134	2131	2024	1855	1942	2021	1986	2239
	8	2224	2100	2361	2103	2077	1838	2121	1931	2052	2278
	7	2356	2189	2309	1983	2061	1780	1906	1823	1810	2148
	6	2415	2109	2353	2155	2117	1801	1930	2022	1934	2259
	5	2177	2134	2128	1961	2057	2100	1943	1895	1611	2122
	4	2355	1986	2189	1893	2170	1773	1816	1530	1756	2165
	3	2114	1941	2282	2161	2236	1856	1808	1818	1709	2204
	2	2337	2364	1940	2106	2317	1659	1871	1908	1797	2239
	1	2282	1970	1983	2034	1913	1807	1585	1715	1600	2133

Table E.5 – PSPA Results on Small Scale Study (3 Lifts Combined). Fine Mix and

Transition (Hot Weather)

Section	Point	Seismic Modulus from PSPA (for 8 in), ksi									
		Line 1	Line 2	Line 3	Line 4	Line 5	Line 6	Line 7	Line 8	Line 9	Line 10
S10, Deep and Full Debonding	10	1958	1927	2065	2008	1716	1904	1821	2006	1834	1869
	9	1923	1881	1797	1990	1898	2359	1756	1704	1696	1736
	8	1935	1857	1904	1984	2220	2472	2050	1764	1654	1495
	7	1768	1916	1937	2021	2283	2187	1848	2108	1625	1261
	6	2075	1896	1885	2195	1728	2227	2234	2026	2005	1580
	5	1772	2141	1978	1814	2163	2308	2166	1970	1725	1844
	4	1710	2311	2071	1818	1771	2211	1762	1576	1373	1451
	3	1850	1667	1916	1783	1689	2468	1921	1734	1386	1805
	2	1885	1811	1951	1661	1711	2080	2025	1786	1515	1858
	1	1850	1869	1962	1857	1730	2129	2122	1978	1611	1811
S9, Deep and Partial Debonding	10	1698	1874	1656	1721	2319	2443	2593	2353	2075	1985
	9	1727	1625	1747	2130	1907	2251	2390	2477	2038	2104
	8	1877	1842	1744	1908	2384	2766	2575	2435	2118	1927
	7	2075	1798	1822	1891	2301	2531	2585	2125	2081	1877
	6	1993	2110	1833	2203	2381	2651	2344	2473	1922	1905
	5	1802	2054	1770	2009	2238	2919	2521	2452	2307	2179
	4	1686	2079	1746	1805	2092	2779	2647	2283	2350	2170
	3	1864	1713	1704	1799	1708	2510	2546	2510	2307	2478
	2	1636	2041	1698	1537	1745	2244	2268	2626	2366	2494
	1	1794	1924	1780	1878	1792	2312	1747	1835	1324	1559
S8, Shallow and Full Debonding	10	1945	2106	1589	1399	1321	2574	1677	1502	1185	1184
	9	1967	1809	1449	1336	1374	2186	1664	1471	1064	1207
	8	1745	1997	1689	2108	1938	1922	1598	1453	1218	1268
	7	1770	1776	2102	1937	1671	2088	1642	1589	1439	1336
	6	1851	1665	2233	2170	1864	2361	1721	1797	1781	1536
	5	2332	2064	2026	2233	1874	2466	1935	1835	1639	1612
	4	2299	1966	2187	1936	1844	2531	1808	1880	1598	1586
	3	2012	1861	2064	1893	1976	1986	1799	1925	1359	1360
	2	1906	2002	2039	2309	2741	2470	1867	1511	1547	1448
	1	1735	1799	2001	1934	2402	2184	2079	1804	1841	1578
S7, Shallow and Partial Debonding	10	2017	2220	1981	1452	1950	2583	2377	2077	2336	2303
	9	2271	1887	1689	1859	1714	3051	2223	2123	2002	2343
	8	2042	2011	1882	2297	2366	2054	2161	2121	2148	1926
	7	1885	2016	2242	1588	1719	1949	2325	2289	2156	2313
	6	2455	2329	2385	2133	2364	2268	1876	2171	2091	2185
	5	1981	2315	2088	2378	1903	2398	2106	2371	2313	2192
	4	2003	2537	2196	2378	2345	2438	2109	2269	2021	2185
	3	1764	2369	2390	2507	2266	2160	2196	2141	1855	1903
	2	1635	2098	2285	2311	2408	2480	1973	2014	2310	2055
	1	2033	2151	2382	2126	2336	2840	2266	2131	2219	2165
S6, Intact	10	2583	1773	1827	2061	1590	2015	1716	1990	1860	2223
	9	2295	1951	2166	1872	1763	2089	1902	1747	1835	2216
	8	2324	1780	2013	1928	1550	2018	1804	1922	2296	2079
	7	2156	1822	1944	1954	1949	1969	1735	1915	1881	1944
	6	2324	2503	2597	2431	2082	2016	2133	2265	2266	2068
	5	2267	2503	1795	2126	1785	1955	1999	1981	2056	1927
	4	2543	2511	2115	2177	2025	2202	2059	2003	2141	2105
	3	2755	2804	2450	2317	1832	2041	2008	2079	1812	2063
	2	2243	2471	2042	2082	1885	2205	2039	2144	2132	2239
	1	2113	1900	1921	2209	2165	2134	2116	2050	1923	2291

Table E.5 Contd. – PSPA Results on Small Scale Study (3 Lifts Combined). Fine Mix and Transition (Hot Weather)

	15	1280	1448	1583	1764	1828	2258	2296	2323	1965	2049
	14	1499	1564	1721	1874	2090	2669	2173	2050	2324	2161
	13	1475	1248	1498	1934	1892	1863	2533	2534	2024	2284
	12	1294	1820	1784	1735	1539	2197	2165	2036	1949	2122
	11	1249	1155	1383	1319	1654	2134	2029	1988	2007	2295
	10	1416	1406	1764	2045	1784	2071	2309	2462	1882	1999
	9	1124	1425	1770	1986	1698	2395	2053	2301	1837	2107
TRANSITION	**8**	1753	1790	2173	1903	1559	973	1076	1101	1048	980
	7	1854	2292	1935	1905	1252	1343	1151	1110	1037	1208
	6	1916	1878	2177	2023	1101	1239	1324	1059	1140	1086
	5	1822	1951	2243	1921	1028	1061	1272	1292	1156	1069
	4	1943	2184	1984	2074	2021	1910	2134	2324	1972	2272
	3	2087	2092	2035	1999	2023	2284	2083	2172	1973	2066
	2	1986	2176	2082	1962	2189	1974	2243	2226	2041	1854
	1	2086	2045	2148	2197	2079	2160	2055	2394	2015	2136

Table E.6 – PSPA Results on Small Scale Study (3 Lifts Combined). Coarse Mix (Hot Weather)

Section	Point	Seismic Modulus from PSPA (for 2.5 in), ksi									
		Line 1	Line 2	Line 3	Line 4	Line 5	Line 6	Line 7	Line 8	Line 9	Line 10
S5, Deep and Full Debonding	10	1579	1833	2169	2177	1797	1938	2037	2006	1643	1922
	9	1746	1925	2007	2145	2087	2123	2033	2043	1936	1988
	8	1903	1838	2409	1999	2415	2520	1955	2018	2022	2113
	7	1808	2000	2463	2183	2478	2566	2283	2114	2113	2014
	6	1955	2072	1965	1828	2013	2427	2493	2399	2006	2143
	5	2040	2067	1944	2056	2266	2443	2249	2420	1785	1901
	4	1790	2140	1594	1858	2369	2281	2313	2113	1948	1722
	3	1982	1905	1879	2001	2335	2174	2019	1976	1863	1805
	2	2015	2028	1695	1985	2247	2191	1866	2034	1739	1809
	1	1716	1902	1900	2061	2067	2118	1867	1921	1778	1652
S4, Deep and Partial Debonding	10	1670	1785	1624	1470	2074	2148	1907	1645	1915	1760
	9	1691	1755	1670	1364	1959	2082	1739	1521	1754	1841
	8	1779	1774	1619	1328	2045	2074	2014	1665	1794	1907
	7	1866	1910	1647	1623	1994	1975	1998	1921	1976	1978
	6	1730	1714	1597	1619	2023	2004	1880	1828	1508	1861
	5	1605	1710	1703	1635	1956	1672	1818	1888	1789	1713
	4	1805	1678	1622	1644	1761	2137	1834	1713	1399	1261
	3	1601	1577	1627	1661	1979	1861	1869	1765	1338	864
	2	1608	1593	1581	1539	1910	1791	1810	1846	1648	1435
	1	1588	1682	1685	1628	1883	1964	1475	1525	1404	1138
S3, Shallow and Full Debonding	10	1503	1295	1083	913	1288	1514	1107	945	1185	982
	9	1600	1210	953	1122	1182	1565	1176	1086	1160	1085
	8	1696	1494	1532	1318	1486	1600	1081	1102	1261	967
	7	1685	1709	1295	1047	1261	1715	1137	1184	1110	1107
	6	1525	1622	1520	1365	1533	1328	1415	1446	1307	1082
	5	1793	1581	1508	1344	1743	1573	1400	1362	1207	1008
	4	1748	1676	1601	1590	1617	1755	1136	1136	1065	1148
	3	1798	1895	1524	1241	1641	1755	989	1071	1368	1155
	2	1873	1768	1646	1500	1926	1498	1024	1051	1087	1133
	1	1794	1655	1597	1387	1577	1541	1348	1355	1259	1185
S2, Shallow and Partial Debonding	10	1924	1846	1584	1631	1729	1838	1612	1482	1491	1430
	9	1931	1906	1530	1425	1938	1828	1687	1549	1271	1653
	8	2049	1849	1715	1580	1660	1732	1636	1557	1518	1660
	7	1807	1914	1707	1496	1530	1766	1812	1753	1515	1502
	6	1960	1897	1749	1803	1725	1730	1510	1710	1549	1681
	5	2038	1982	1936	1408	1588	1791	1569	1592	1371	1751
	4	1939	2103	1859	1750	1900	1890	1475	1482	1380	1561
	3	1971	1854	1764	1580	1652	1822	1725	1541	1534	1519
	2	1738	1935	1847	1774	1857	1828	1569	1434	1305	1630
	1	1800	1759	1776	1759	1783	1664	1858	1609	1782	1580
S1, Intact	10	2018	2051	1755	1833	1926	2000	1933	1984	1868	1826
	9	1969	1900	1720	1796	1641	1653	1734	1890	1830	1782
	8	1991	1906	1794	1783	1731	1848	1675	1784	1926	1763
	7	1902	1996	1861	1582	1446	1516	1845	1692	1757	1578
	6	2115	1831	1699	1670	1629	1741	1738	1814	1912	1692
	5	1846	2024	1782	1666	1667	1860	1786	1814	1757	1651
	4	1840	2256	1843	1640	1662	1839	1794	1820	1897	1782
	3	1751	1973	1645	1677	1690	1872	1871	1717	1808	1930
	2	1531	1800	1779	1532	1560	1806	1664	1726	1893	1937
	1	1519	1666	1788	1429	1453	1779	1513	1767	1878	2106

**Table E.7 – PSPA Results on Small Scale Study (Top Lift). Fine Mix and Transition (Hot Weather)**

Section	Point	Seismic Modulus from PSPA (for 2.5 in), ksi									
		Line 1	Line 2	Line 3	Line 4	Line 5	Line 6	Line 7	Line 8	Line 9	Line 10
S10, Deep and Full Debonding	10	2106	2033	2260	2031	1812	1797	2023	2021	2085	1964
	9	2216	1832	1926	2150	1964	2178	1857	1728	1899	1688
	8	2048	2041	1974	2106	2209	2508	2387	1753	1842	1872
	7	2117	1946	1876	2305	2183	2047	1728	2131	1724	1680
	6	2059	2183	1957	2213	2034	2279	2056	2268	2294	1460
	5	1957	2344	2128	1826	2105	2066	2228	1898	1749	2164
	4	1953	2286	2074	1903	1930	2205	1959	1501	1552	1541
	3	2019	1744	1931	1911	1655	2221	2151	1855	1697	1894
	2	1872	1916	1997	1903	1983	1953	1795	1941	1758	1864
	1	1909	1993	1960	1955	1772	1954	1964	2190	1641	1966
S9, Deep and Partial Debonding	10	1557	1884	1696	1507	2009	1824	1853	1811	1702	1645
	9	1471	1697	1837	2035	1558	1701	1963	1967	1763	1814
	8	1752	1746	1624	1696	2180	2262	1856	1944	1719	1736
	7	1887	1588	1619	1622	2139	2026	2120	1759	1740	1838
	6	1702	2053	1760	2099	2065	2091	1880	2050	1949	1867
	5	1738	1685	1882	1964	2070	2533	2231	1877	1940	1988
	4	1622	2006	1690	1853	2049	2078	1955	1852	2116	1832
	3	1688	1619	1816	1587	1581	1980	1956	2111	1966	1982
	2	1604	1799	1754	1592	1673	1936	1966	2141	1945	1914
	1	1665	1752	1626	1827	1776	1902	1858	1706	1383	1428
S8, Shallow and Full Debonding	10	1901	1840	1666	1323	1377	2280	1641	1702	1484	1548
	9	1866	1871	1525	1438	1392	1930	2081	1680	1399	1522
	8	1682	1881	1671	1967	1690	1799	1735	1583	1473	1514
	7	1843	1861	1966	2125	1674	1896	1750	1637	1901	1668
	6	1765	1726	2020	2111	1803	2078	1770	1853	1737	1617
	5	2061	2071	1732	2020	1808	2062	1851	1718	1860	1733
	4	2218	1942	2138	1918	1777	2289	1790	1671	1880	1711
	3	1837	1764	2008	1615	1678	1856	1727	1974	1421	1529
	2	1829	1845	1872	2074	2074	2234	1736	1554	1735	1653
	1	1665	1785	1923	1803	2094	2031	2040	1688	1858	1784
S7, Shallow and Partial Debonding	10	1653	1827	1466	1333	1825	1967	1614	1498	1582	1375
	9	1729	1700	1313	1444	1458	2075	1872	1633	1797	1784
	8	1594	1487	1665	1888	1936	1492	1732	1850	1523	1632
	7	1412	1514	1555	1483	1751	1727	1709	1845	1558	1765
	6	1995	1799	1756	1881	2116	1730	1785	1668	1715	1711
	5	1639	1974	1895	2081	1954	1954	1658	1939	1994	1877
	4	1688	1994	1913	2313	1884	1938	1960	1930	1932	1611
	3	1343	1905	2024	2010	2069	1844	1795	1722	1589	1696
	2	1525	1883	1800	1832	2140	1939	1650	1652	1873	1611
	1	1800	1677	2014	1546	1963	2211	1737	1739	1758	1677
S6, Intact	10	1435	1754	1661	1946	1759	1841	1622	2032	1701	2366
	9	1587	1988	1962	1897	1896	1889	1756	1719	1914	2254
	8	1858	1691	1729	1840	1579	1836	1667	1936	2249	2029
	7	1720	1784	1841	1722	1888	1857	1641	2000	1899	1864
	6	1811	1999	2177	2009	1904	1900	2042	2059	1987	2002
	5	1638	1978	1719	1886	1763	1800	2007	1862	1991	1884
	4	1380	2005	1910	1988	1767	2143	1910	1870	1997	1915
	3	2775	2076	2210	2107	1504	1792	1872	1926	1599	1805
	2	2171	1766	1946	1899	1690	1923	1846	1841	1903	1983
	1	1491	2077	1883	1948	1938	2016	1803	1929	1793	2072

Table E.7 Contd. – PSPA Results on Small Scale Study (Top Lift). Fine Mix and Transition
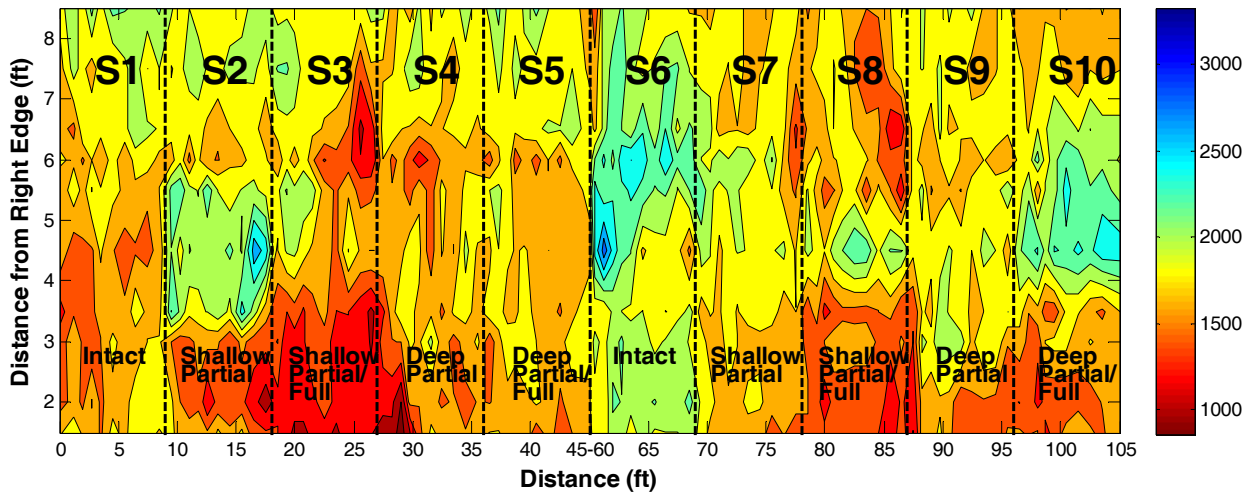
(Hot Weather)

	15	1337	1586	1550	1584	1426	1937	2554	2272	1836	2060
	14	1456	1712	1630	1678	2170	3233	2127	2342	2531	2074
	13	1462	1400	1309	1673	1651	1497	2215	2413	1718	2031
	12	1463	1742	1592	1526	1590	1899	1527	1881	2028	2220
	11	1508	1151	1371	1381	1521	1982	1877	1932	1875	2338
TRANSITION	**10**	1542	1472	1742	2015	1950	1863	2421	2570	1753	1994
	9	1164	1428	1813	2022	1705	2274	2115	2361	1791	2056
	8	1657	1791	2138	1747	1594	1313	1410	1560	1491	1630
	7	1870	2306	2070	1789	1346	2022	1584	1609	1966	2113
	6	1960	1761	2010	1968	1338	1609	1798	1370	1723	1890
	5	1698	1782	2312	1839	1399	1765	1649	1807	1941	1570
	4	1648	2022	1883	2011	1989	1849	2029	2448	2025	2439
	3	2144	1945	1955	1875	2049	2063	2170	2044	2090	1954
	2	1930	2096	2027	1878	2079	2166	2201	2174	1991	1748
	1	2111	2078	2095	1987	2057	2053	2023	2434	1916	2108

Table E.8 – PSPA Results on Small Scale Study (Top Lift). Coarse Mix (Hot Weather)

Section	Point	Seismic Modulus from PSPA (for 2.5 in), ksi									
		Line 1	Line 2	Line 3	Line 4	Line 5	Line 6	Line 7	Line 8	Line 9	Line 10
S5, Deep and Full Debonding	10	1465	1745	1771	1890	1626	1766	1906	1875	1644	1927
	9	1816	1679	1840	1990	2109	1725	1938	1973	1919	2046
	8	1555	1601	2257	1983	2404	2215	1786	1806	1989	2265
	7	1551	1843	2324	2080	2390	2346	2152	2127	2129	1859
	6	1786	1872	2040	1832	2188	2355	2308	2298	2076	2215
	5	1715	1898	1941	2126	2325	2364	2264	2261	1954	2013
	4	1822	2069	1785	1961	2238	2123	2152	2225	2147	1856
	3	1836	1846	1725	1836	2050	1985	1933	2044	1924	1922
	2	1939	1980	1616	1903	1875	2082	1946	2048	1776	1896
	1	1628	1722	1901	1783	2026	2042	1882	1981	1769	1853
S4, Deep and Partial Debonding	10	2079	1899	1948	1709	1802	1960	1916	2108	1988	1966
	9	2100	1927	2051	1897	2026	2071	2021	1972	1970	1874
	8	1940	1885	1941	1874	2097	1882	1918	1755	1917	1972
	7	2027	1863	2021	1752	2063	2136	1899	2043	1902	1922
	6	1942	2090	1914	1740	1866	1722	1989	2194	1959	2120
	5	2193	2114	2040	1502	1892	1968	2000	1859	1938	1787
	4	1691	2269	2106	1617	1595	2139	2103	2223	1952	1492
	3	1938	1961	1950	1823	1767	1838	2139	1830	1482	1189
	2	1785	1824	2081	1600	1655	1840	1902	1758	1710	1711
	1	2085	1827	2008	1795	1848	1976	1777	1956	1724	1552
S3, Shallow and Full Debonding	10	1515	1574	1599	1383	1642	1600	1510	1541	1824	1483
	9	1682	1350	1223	1523	1403	1706	1554	1594	1596	1624
	8	1776	1569	1740	1447	1615	1778	1504	1551	1579	1379
	7	1669	1864	1617	1378	1585	1937	1577	1574	1721	1368
	6	1552	1707	1723	1402	1543	1464	1571	1638	1444	1444
	5	1791	1784	1811	1528	1933	1888	1631	1668	1559	1400
	4	1729	1664	1835	1676	1625	1929	1412	1259	1394	1671
	3	1776	2068	1732	1411	1680	1857	1176	1337	1508	1541
	2	1782	1956	1806	1608	1923	1536	1163	1208	1236	1581
	1	1836	1645	1753	1538	1695	1759	1528	1460	1586	1570
S2, Shallow and Partial Debonding	10	1742	1713	1831	1758	1741	1956	2175	1729	1459	1769
	9	1563	1751	1735	1659	2152	1900	1911	1797	1429	1811
	8	1630	1799	1831	1679	1748	1842	1836	1689	1638	2076
	7	1563	1596	1809	1893	1546	2004	2036	1878	1631	1630
	6	1792	1758	1957	1835	1882	1916	1604	1792	1702	1836
	5	1767	1744	1927	1612	1724	1975	1939	1724	1481	2026
	4	1666	1815	1440	1908	1998	2082	1863	1727	1644	1758
	3	1629	1632	1430	1882	1868	1700	2021	1759	1694	1785
	2	1561	1722	1572	1892	1912	1825	2115	1757	1500	1734
	1	1471	1596	1688	1806	1918	1759	2081	1684	1841	1712
S1, Intact	10	1956	1962	1603	1709	1706	1852	1589	1856	1783	1723
	9	1797	1767	1614	1727	1645	1592	1603	1784	1731	1613
	8	1863	1782	1773	1765	1692	1697	1624	1572	1748	1732
	7	1858	1772	1908	1659	1492	1507	1755	1617	1580	1545
	6	1940	1754	1726	1743	1603	1752	1614	1772	1778	1711
	5	1799	1917	1782	1678	1628	1846	1766	1832	1649	1624
	4	1710	2222	1700	1636	1556	1895	1710	1865	1870	1613
	3	1734	1876	1600	1635	1754	1758	1776	1745	1726	2004
	2	1502	1760	1793	1625	1535	1697	1591	1698	1783	1786
	1	2252	1718	1759	1438	1480	1768	1475	1653	1698	1890
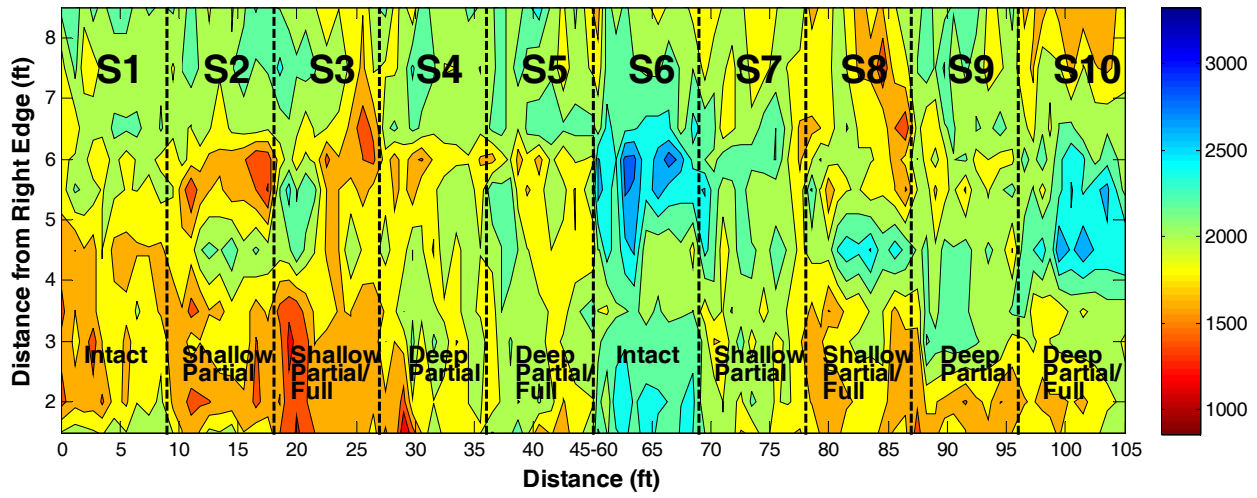
a) 2.5 inches

b) 8 inches

Figure E.1 – Overall Modulus Results (Top View) on Small Scale Study. Hot Weather
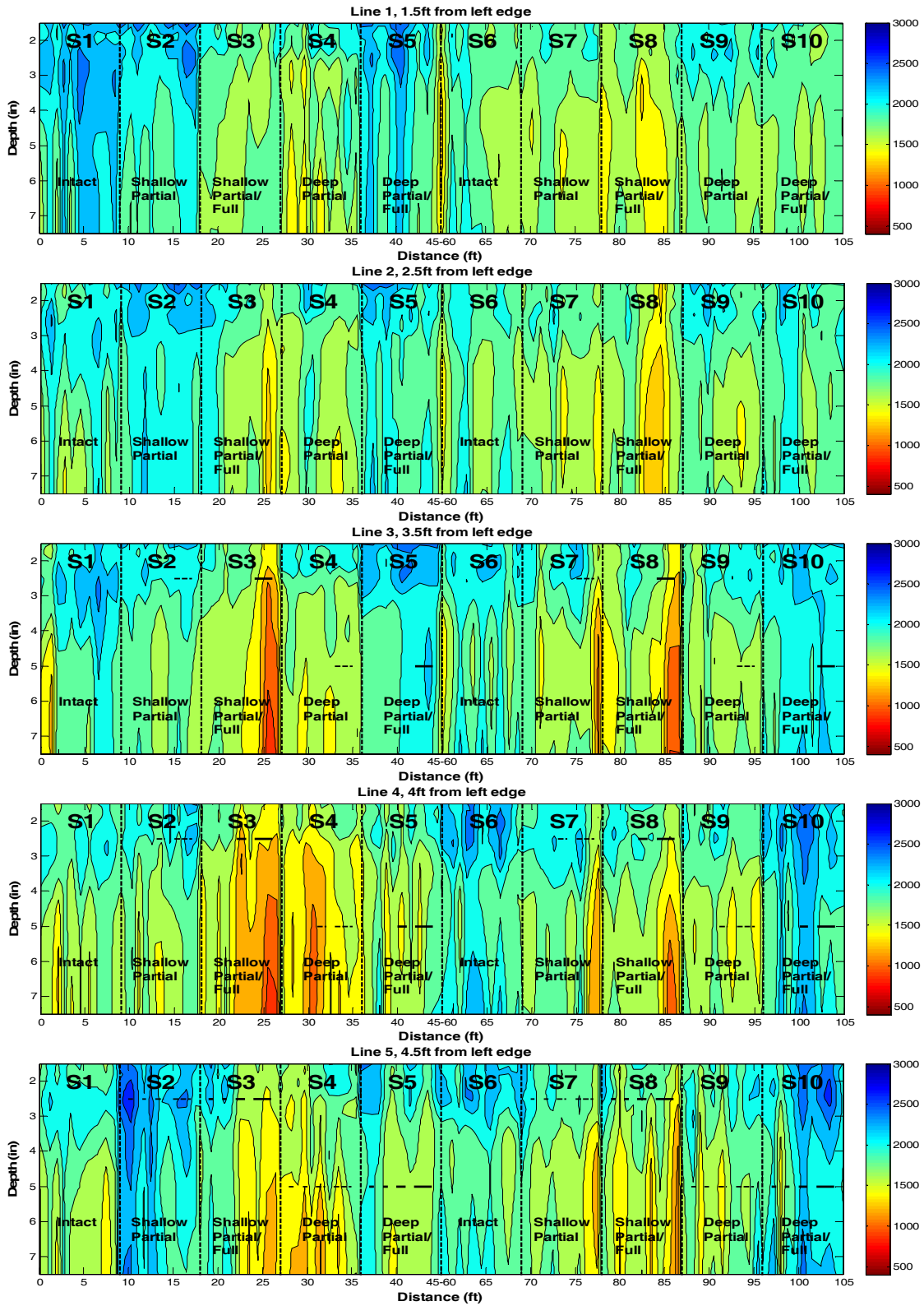
Results

Figure E.2 – Dispersion Curve Results for 10 Lines of Extended Testing (Cross Section and Cool Weather)
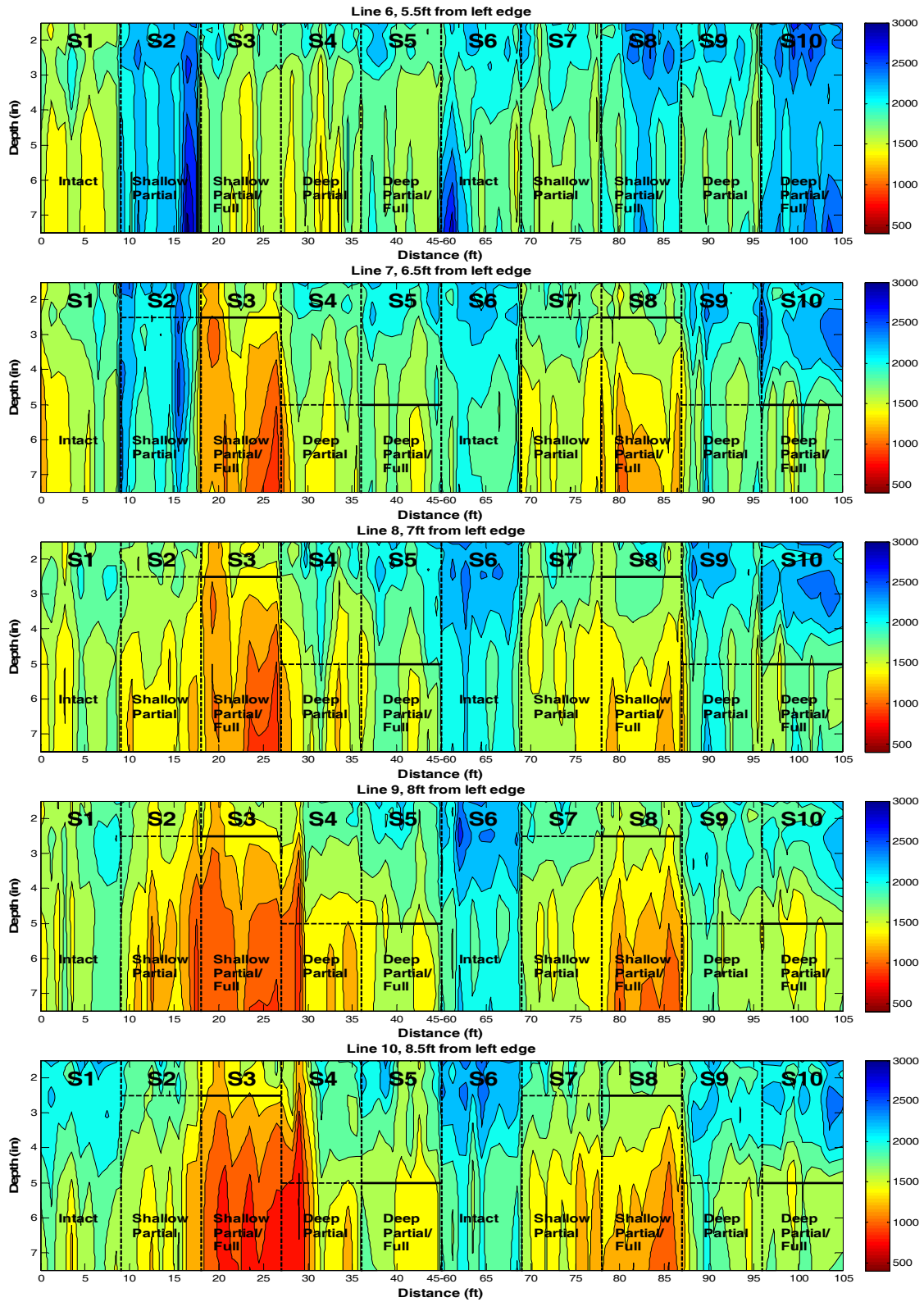
Figure E.2 Contd. – Dispersion Curve Results for 10 Lines of Extended Testing (Cross Section and Cool Weather)
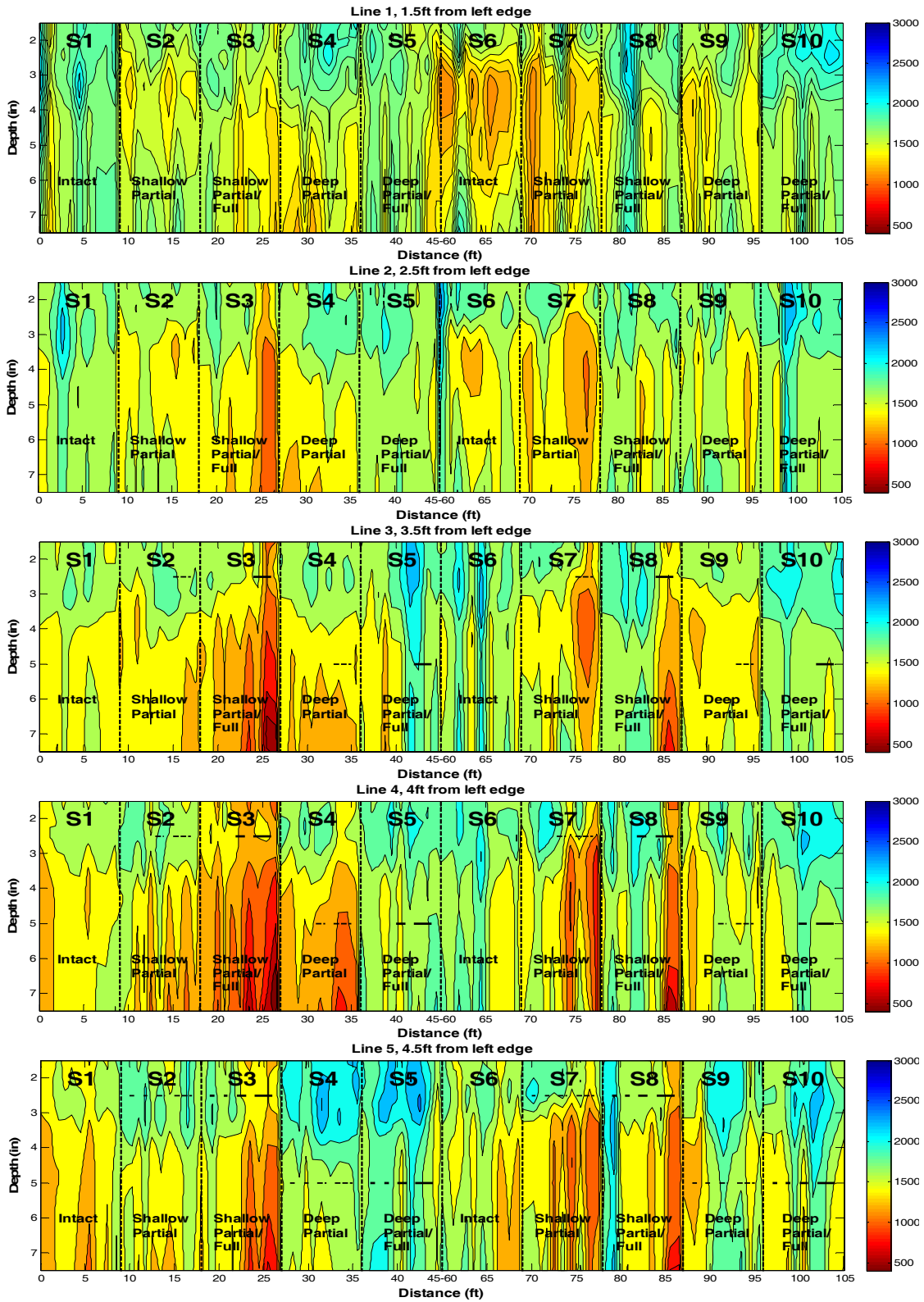
85

Figure E.3 – Dispersion Curve Results for 10 Lines of Extended Testing (Cross Section and Hot Weather)

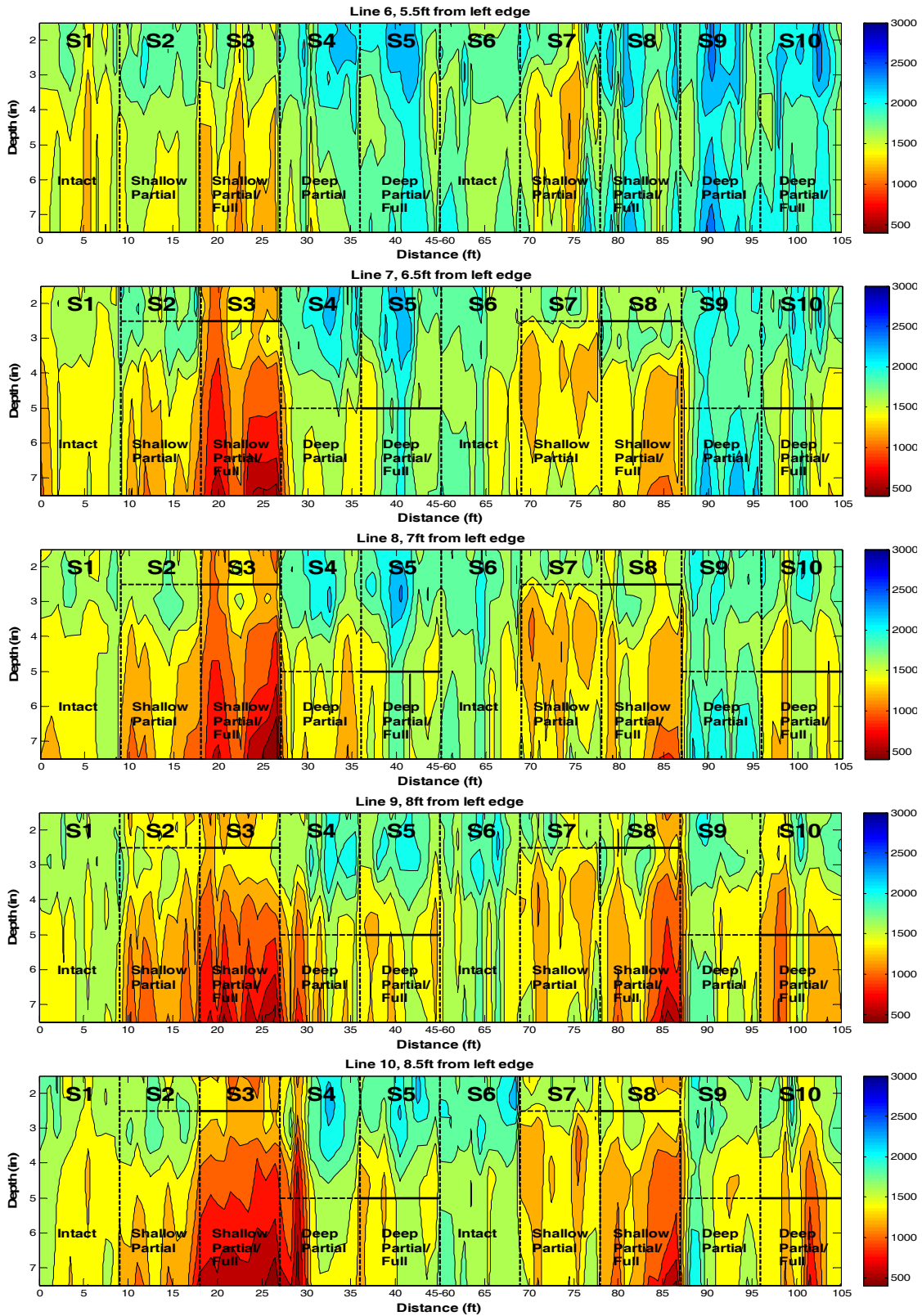**Figure E.3 Contd. – Dispersion Curve Results for 10 Lines of Extended Testing (Cross Section and Hot Weather)**
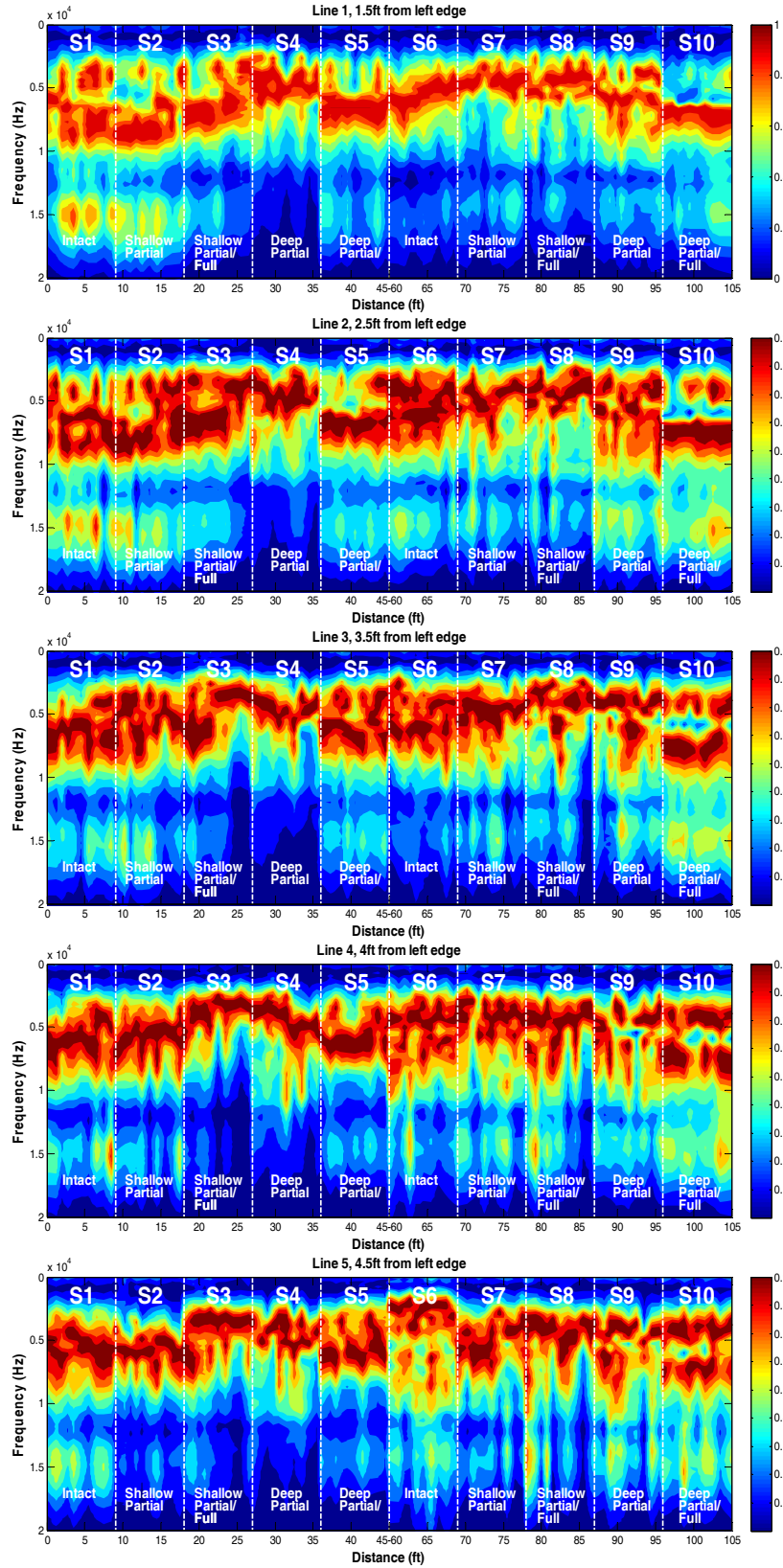
Figure E.4 – IE Results with PSPA on Extended Tests of Small Scale Study (Cool Weather)
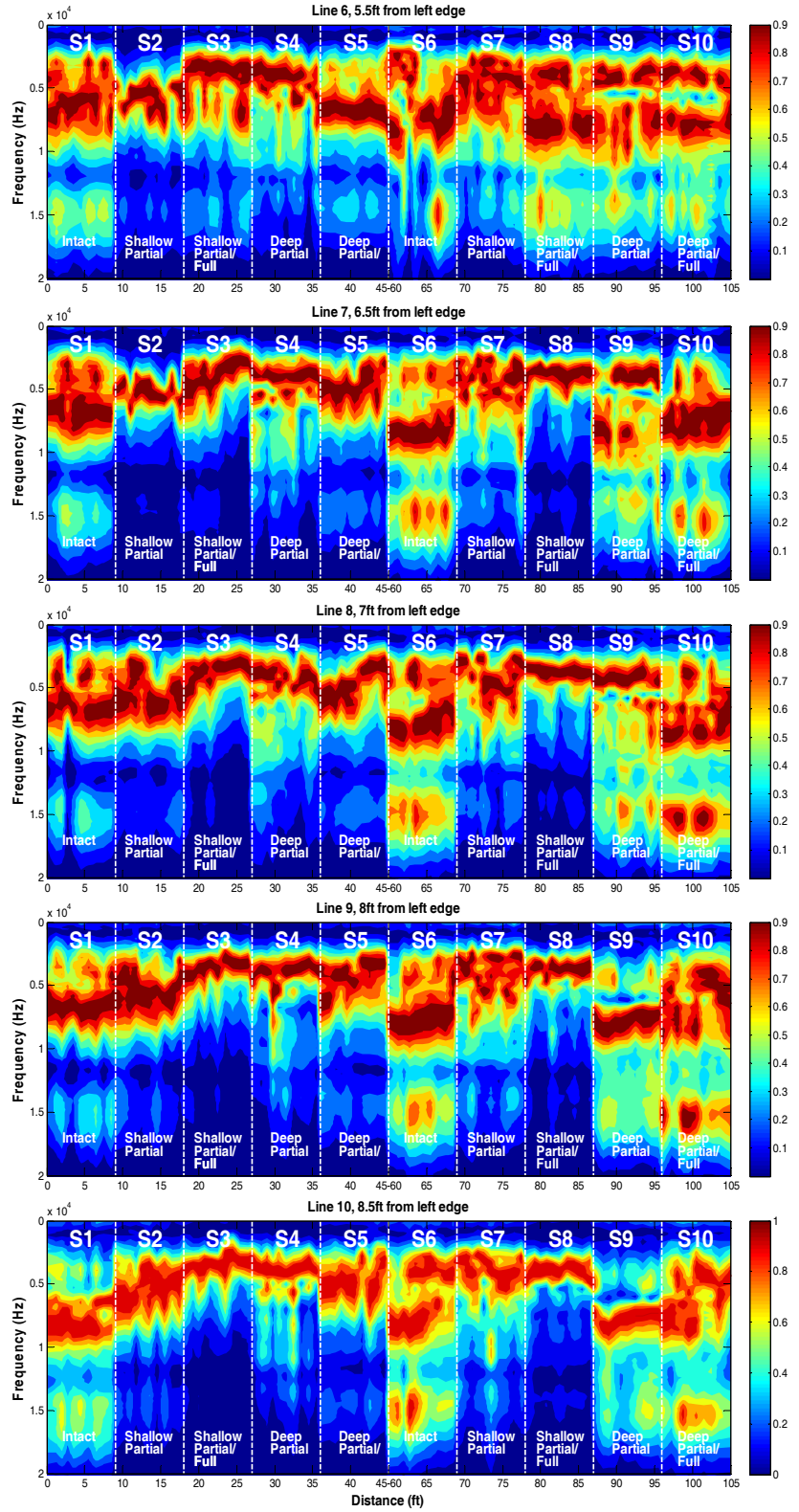
Figure E.4 Contd. – IE Results with PSPA on Extended Tests of Small Scale Study (Cool Weather)
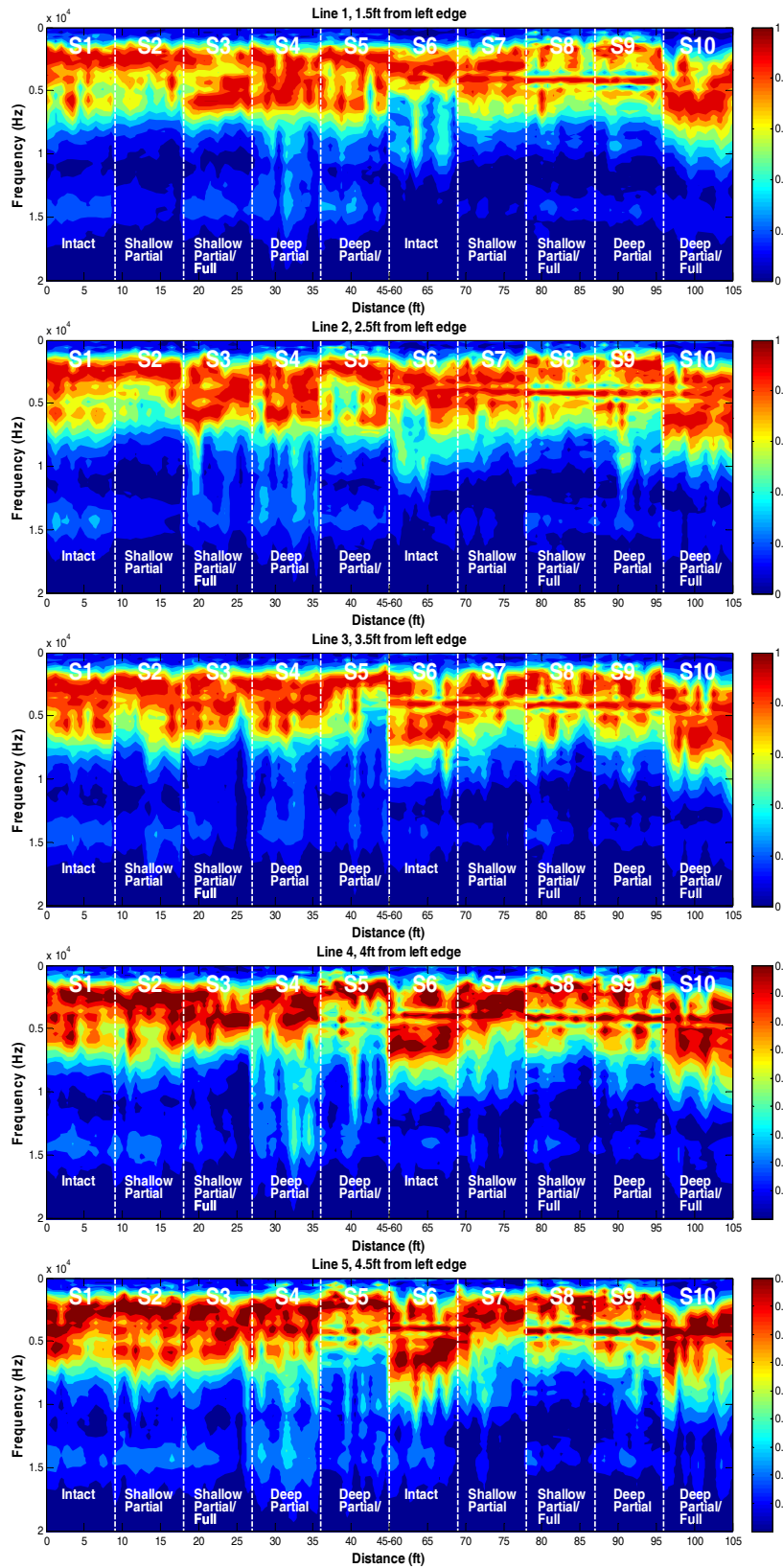
89

Figure E.5 – IE Results with PSPA on Extended Tests of Small Scale Study (Hot Weather)
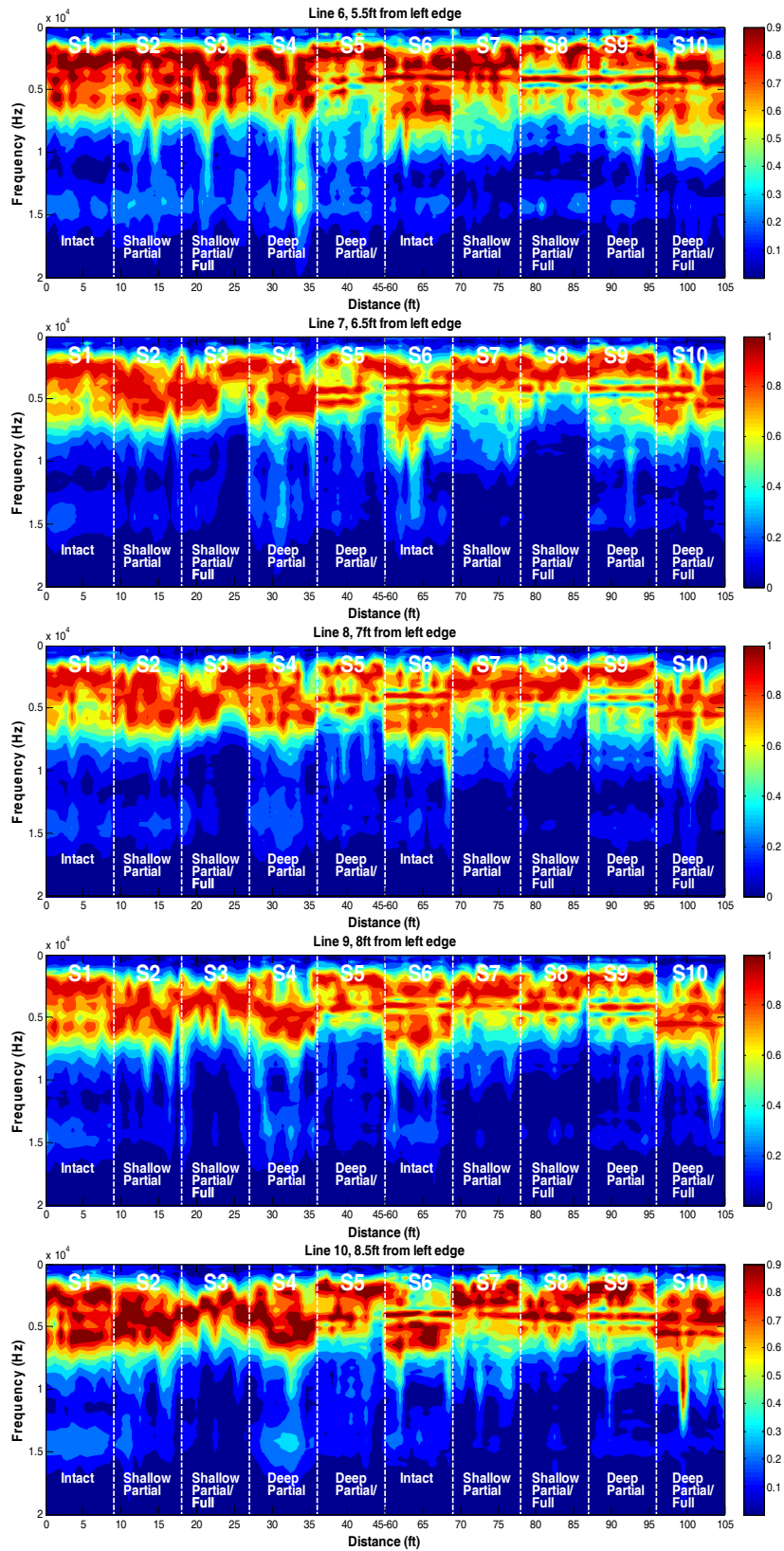
90

Figure E.5 Contd. – IE Results with PSPA on Extended Tests of Small Scale Study (Hot Weather)

Table E.9 – FFT Ratios of Impulse Response on Small Scale Study. Fine Mix and Transition (Cool Weather)

| Section | Point | Impulse Response FFT Ratios (Load/Geophone) | | | | | | | | | |
		Line 1	Line 2	Line 3	Line 4	Line 5	Line 6	Line 7	Line 8	Line 9	Line 10
S10, Deep and Full Debonding	10	3.05	3.31	3.06	2.85	2.85	2.82	2.35	2.20	1.74	1.41
	9	3.25	3.30	3.00	2.82	2.42	2.54	2.44	2.20	1.63	1.43
	8	3.13	3.45	2.84	3.16	2.83	2.71	2.40	2.21	1.33	1.13
	7	3.12	2.78	3.06	3.03	3.02	2.54	2.19	2.06	1.15	0.89
	6	2.23	2.87	3.22	2.96	2.92	2.54	1.85	2.13	1.31	0.90
	5	1.86	2.72	2.88	3.04	3.02	2.70	1.76	1.49	1.29	1.02
	4	1.96	2.63	3.13	2.93	2.85	2.64	1.72	1.50	1.03	1.08
	3	2.06	2.46	2.93	2.74	2.51	2.64	1.69	1.48	1.25	1.18
	2	2.07	2.69	2.89	2.84	2.58	2.76	1.78	1.46	1.46	1.19
	1	2.59	2.80	3.02	2.74	2.82	2.89	2.50	1.54	1.64	1.26
S9, Deep and Partial Debonding	10	2.47	2.87	2.19	1.93	2.67	2.69	2.03	1.81	1.62	1.47
	9	2.14	2.00	2.32	1.74	2.03	2.38	2.31	1.90	1.60	1.51
	8	2.15	2.89	1.92	1.71	2.01	1.87	2.44	1.88	1.60	1.40
	7	2.68	2.85	2.88	2.58	2.66	2.38	2.45	2.06	1.78	1.37
	6	2.03	2.74	2.46	2.05	2.06	2.23	2.43	1.96	1.65	1.36
	5	2.18	2.39	2.30	1.88	2.07	2.01	1.97	1.91	1.62	1.41
	4	1.63	2.56	2.12	1.98	1.76	2.08	1.97	1.98	1.68	1.39
	3	2.13	2.42	2.28	1.97	2.19	2.23	2.05	1.89	1.79	1.68
	2	2.39	2.47	1.88	2.17	2.30	2.06	2.30	2.00	1.80	1.42
	1	2.43	2.92	2.57	2.12	2.55	2.43	1.99	1.88	1.61	1.37
S8, Shallow and Full Debonding	10	2.25	2.45	1.75	1.66	1.97	2.21	1.43	1.24	1.05	1.27
	9	2.56	2.04	1.34	1.27	1.45	2.01	1.46	1.15	1.23	1.17
	8	2.34	2.20	1.33	1.40	1.71	2.06	1.39	1.06	1.20	1.21
	7	2.38	2.20	2.21	2.31	2.26	2.32	1.51	1.35	1.38	1.22
	6	2.18	2.59	2.64	2.40	2.49	2.38	1.86	1.70	1.45	1.48
	5	2.39	2.44	2.82	2.55	2.62	2.40	1.98	1.59	1.39	1.49
	4	2.63	2.62	2.77	2.54	2.48	2.39	1.83	1.44	1.41	1.26
	3	2.39	2.29	2.45	2.30	2.33	2.28	1.82	1.62	1.32	1.50
	2	2.41	2.32	2.52	2.32	2.31	2.42	1.87	1.79	1.47	1.63
	1	2.12	2.27	2.39	2.28	2.36	2.35	2.26	1.94	1.78	1.69
S7, Shallow and Partial Debonding	10	2.54	2.36	2.21	2.17	2.18	2.51	2.47	2.36	2.18	2.06
	9	2.56	2.24	1.98	2.13	2.04	2.56	2.27	2.25	2.24	2.02
	8	2.77	2.45	2.32	2.25	2.23	2.46	2.42	2.34	2.30	2.06
	7	2.65	2.58	2.16	2.44	2.20	2.36	2.52	2.35	2.32	2.08
	6	2.61	2.35	2.38	2.40	2.35	2.32	2.41	2.31	2.34	2.10
	5	2.41	2.43	2.21	2.45	2.09	2.33	2.21	2.12	2.23	2.00
	4	2.42	2.48	2.57	2.36	2.32	2.31	2.08	2.17	1.96	2.02
	3	2.46	2.67	2.50	2.31	2.23	2.29	2.10	2.04	1.89	2.08
	2	2.48	2.47	2.35	2.39	2.19	2.32	2.03	2.02	1.97	1.94
	1	2.32	2.63	2.60	2.40	2.30	2.40	2.12	2.10	2.17	2.00
S6, Intact	10	2.30	2.13	1.99	1.99	2.04	1.83	1.96	2.06	2.02	2.00
	9	2.18	2.10	1.98	1.94	1.99	1.93	1.86	2.09	2.13	1.89
	8	2.13	2.00	1.92	1.88	1.88	1.84	2.05	2.01	1.93	1.64
	7	1.82	1.92	1.87	1.92	1.95	1.82	2.00	1.81	1.90	1.71
	6	1.91	2.07	1.97	1.95	2.08	1.85	1.72	1.79	1.54	1.75
	5	1.97	1.89	1.99	1.92	1.96	1.89	1.75	1.89	1.88	1.81
	4	2.00	2.08	1.94	2.03	2.07	1.93	1.77	1.89	1.98	1.80
	3	2.22	2.28	2.09	2.15	2.07	1.94	1.79	1.83	1.78	1.90
	2	2.12	2.22	2.14	2.22	2.19	1.99	1.87	1.98	1.77	1.89
	1	2.12	2.18	2.07	2.14	2.15	1.97	1.76	2.11	1.95	1.79

Table E.9 Contd. – FFT Ratios of Impulse Response on Small Scale Study. Fine Mix and

Transition (Cool Weather)

	15	1.85	1.96	1.65	2.00	2.17	2.35	2.17	2.26	1.99	1.77
	14	1.87	1.94	1.84	2.21	2.22	2.33	2.08	2.22	2.05	1.78
	13	1.91	1.90	2.06	2.19	2.07	2.11	2.07	2.01	2.00	1.75
	12	1.77	1.85	1.84	2.04	2.04	2.16	2.07	2.14	1.97	1.65
	11	1.66	1.80	1.86	1.80	2.01	2.14	1.96	2.13	1.94	1.69
	10	1.58	1.72	1.61	1.80	2.00	2.05	2.00	2.07	1.84	1.67
TRANSITION	**9**	1.53	1.83	1.72	2.03	2.07	1.98	1.95	1.89	1.83	1.63
	8	1.60	2.01	2.03	1.95	1.82	1.37	1.24	1.34	1.40	1.16
	7	1.91	2.18	2.01	1.90	1.45	0.46	0.55	0.88	1.25	0.77
	6	1.96	2.13	1.96	1.81	1.44	0.36	0.52	0.72	0.85	0.81
	5	2.14	2.26	2.12	1.91	1.49	0.68	0.85	0.83	0.94	1.44
	4	2.23	2.40	2.05	2.00	1.86	1.67	1.67	1.71	1.70	1.50
	3	2.26	2.42	2.33	2.36	2.50	2.44	2.39	2.40	2.15	1.81
	2	2.15	2.33	2.23	2.52	2.39	2.81	2.82	2.79	2.23	1.89
	1	2.01	2.37	2.33	2.33	2.30	2.93	2.90	2.85	2.22	1.95

Table E.10 – FFT Ratios of Impulse Response on Small Scale Study. Coarse Mix (Cool Weather)

Section	Point	Impulse Response FFT Ratios (Load/geophone)									
		Line 1	Line 2	Line 3	Line 4	Line 5	Line 6	Line 7	Line 8	Line 9	Line 10
S5, Deep and Full Debonding	10	1.90	2.02	2.09	2.02	2.19	2.54	2.45	2.21	1.70	1.65
	9	1.82	1.99	1.93	1.72	1.96	2.35	2.28	1.98	1.43	1.61
	8	1.90	1.98	2.03	1.54	1.84	2.37	2.22	1.83	1.68	1.80
	7	1.99	2.06	2.27	2.03	2.15	2.47	2.38	2.37	1.90	1.87
	6	2.08	2.16	2.43	2.31	2.45	2.56	2.34	2.23	1.95	2.07
	5	2.17	2.40	2.69	2.50	2.52	2.45	2.30	2.21	1.70	2.01
	4	2.21	2.55	2.86	2.52	2.66	2.48	2.21	1.99	1.26	1.66
	3	2.30	2.42	2.96	2.74	2.73	2.86	2.15	2.01	1.52	1.34
	2	2.32	2.48	2.88	2.76	2.68	2.70	2.21	1.88	1.49	1.61
	1	2.37	2.62	3.02	2.94	2.93	2.74	2.44	2.13	1.78	1.78
S4, Deep and Partial Debonding	10	2.37	2.81	2.59	2.53	2.76	2.79	2.48	2.37	2.16	2.05
	9	2.34	2.67	2.58	2.44	2.51	2.43	2.43	2.27	2.05	2.14
	8	2.32	2.59	2.32	2.13	2.43	2.32	2.11	2.19	2.10	2.05
	7	2.24	2.24	2.12	2.04	2.27	2.06	2.06	2.05	2.12	1.93
	6	2.05	2.12	1.95	1.97	2.04	1.97	2.00	2.08	1.91	1.73
	5	1.85	1.99	1.92	2.00	2.08	2.02	1.98	1.98	1.78	1.64
	4	1.93	1.96	2.01	2.07	2.08	1.99	2.01	2.00	1.57	1.38
	3	1.94	2.15	2.11	2.16	2.22	2.01	1.90	1.82	1.31	1.23
	2	1.95	2.30	2.32	2.29	2.36	2.06	1.83	1.73	1.44	1.22
	1	2.02	2.36	2.46	2.48	2.42	2.02	1.76	1.77	1.33	1.16
S3, Shallow and Full Debonding	10	2.22	2.47	2.20	1.98	2.27	1.99	1.53	1.35	1.54	1.35
	9	2.23	2.30	2.08	1.87	2.20	1.91	1.38	1.19	1.52	1.43
	8	2.25	2.40	2.30	2.02	2.37	2.01	1.36	1.27	1.59	1.44
	7	2.09	2.37	2.05	2.17	2.34	2.20	1.38	1.27	1.66	1.44
	6	2.01	2.21	2.04	2.17	2.30	2.29	1.75	1.64	1.67	1.52
	5	2.04	2.19	2.20	2.21	2.50	2.30	1.84	1.72	1.72	1.50
	4	1.94	2.19	2.28	2.38	2.53	2.23	1.73	1.69	1.58	1.51
	3	2.02	2.29	2.50	2.49	2.57	2.23	1.70	1.65	1.61	1.49
	2	1.99	2.40	2.53	2.63	2.66	2.18	1.73	1.78	1.71	1.51
	1	2.08	2.46	2.72	2.73	2.75	2.24	1.91	1.83	1.77	1.61
S2, Shallow and Partial Debonding	10	2.00	2.33	2.65	2.82	2.79	2.27	2.17	2.03	1.89	1.63
	9	2.08	2.32	2.27	2.41	2.45	2.53	2.35	2.28	1.93	1.77
	8	2.28	2.27	2.30	2.48	2.26	2.54	2.39	2.32	2.03	1.77
	7	2.32	2.56	2.58	2.37	2.58	2.20	2.31	2.32	2.07	1.84
	6	2.10	2.15	2.50	2.56	2.56	2.68	2.35	2.35	2.13	2.00
	5	1.99	2.13	2.40	2.55	2.24	2.65	2.30	2.31	2.16	1.89
	4	1.93	2.25	2.82	2.84	2.83	2.63	2.27	2.26	2.16	1.95
	3	1.87	2.21	2.85	2.82	2.85	2.76	2.35	2.12	2.01	1.89
	2	2.02	2.40	2.76	2.96	2.93	2.61	2.26	2.16	2.11	2.00
	1	0.89	2.53	3.05	3.08	3.02	2.64	2.28	2.02	2.32	2.06
S1, Intact	10	2.47	2.48	2.38	2.18	2.23	1.98	2.10	2.18	2.29	2.02
	9	2.33	2.85	2.62	2.33	2.32	2.26	2.06	2.10	2.27	1.98
	8	2.60	3.19	2.78	2.70	2.53	2.06	1.91	2.00	2.16	1.99
	7	2.80	3.27	3.20	2.94	2.75	2.14	1.83	1.83	2.18	2.01
	6	2.56	3.17	2.96	2.61	2.52	2.06	1.80	1.97	2.20	2.04
	5	2.31	2.76	2.59	2.09	2.32	2.12	1.92	2.10	2.19	2.08
	4	2.20	2.78	2.66	2.19	2.27	2.17	1.99	1.96	2.13	1.96
	3	2.19	2.55	2.74	2.06	2.15	2.13	2.05	1.84	2.13	1.90
	2	1.96	2.54	2.35	2.25	2.26	1.99	2.09	1.91	2.01	1.92
	1	1.94	2.63	2.19	2.21	2.34	1.81	1.95	1.98	2.05	1.99

Table E.11 – FFT Ratios of Impulse Response on Small Scale Study. Fine Mix and Transition (Hot Weather)

Section	Point	Impulse Response FFT Ratios (Load/Geophone)									
		Line 1	Line 2	Line 3	Line 4	Line 5	Line 6	Line 7	Line 8	Line 9	Line 10
S10, Deep and Full Debonding	10	3.34	3.48	3.22	2.87	2.73	2.57	2.35	1.81	1.57	1.35
	9	3.42	3.12	3.18	3.03	2.87	2.71	2.24	1.69	1.15	1.08
	8	3.56	3.39	3.29	3.14	2.73	2.50	2.23	1.75	1.19	1.03
	7	3.51	3.61	3.59	3.25	2.89	2.64	2.23	1.99	1.40	1.11
	6	3.13	3.24	3.30	3.25	3.03	2.64	2.29	2.22	1.47	1.18
	5	2.34	3.07	3.39	3.16	2.99	2.74	2.11	1.77	1.23	1.29
	4	2.47	3.06	3.32	3.19	2.91	2.83	2.09	1.47	1.05	1.16
	3	2.47	3.03	3.31	2.96	2.92	2.68	1.71	1.28	0.92	1.07
	2	2.63	2.84	2.90	2.94	2.62	2.51	1.71	1.39	1.13	1.03
	1	2.50	2.99	2.92	2.92	2.69	2.89	2.28	1.63	1.29	1.17
S9, Deep and Partial Debonding	10	3.32	3.35	3.43	3.50	3.86	4.01	3.01	2.16	1.56	1.55
	9	3.59	3.16	3.37	2.71	3.16	3.49	2.26	1.85	1.42	1.35
	8	3.53	3.63	3.55	3.08	3.19	3.33	2.52	2.07	1.37	1.39
	7	4.31	4.00	3.83	3.83	3.70	3.84	3.35	2.54	1.68	1.45
	6	3.44	3.45	3.24	2.69	2.86	3.10	3.04	2.20	1.57	1.78
	5	2.86	3.19	3.03	2.73	2.66	2.74	2.76	2.15	2.08	1.73
	4	2.78	3.30	3.12	2.83	2.81	2.88	2.40	1.87	1.78	1.80
	3	2.63	3.18	2.76	2.74	3.00	2.93	2.24	1.76	1.70	1.77
	2	2.82	3.08	3.13	3.03	3.32	2.99	2.56	1.97	1.95	1.91
	1	2.95	3.28	3.07	3.13	3.31	3.26	2.66	2.18	2.10	1.82
S8, Shallow and Full Debonding	10	3.14	3.16	2.25	2.14	2.22	2.56	1.76	1.75	1.37	1.54
	9	2.98	2.61	1.82	1.74	1.74	2.30	1.60	1.16	1.05	1.31
	8	2.72	2.68	2.02	1.83	2.10	2.59	1.69	1.29	1.21	1.21
	7	2.66	2.61	2.67	2.62	2.61	2.80	2.00	1.68	1.56	1.69
	6	2.51	2.67	2.81	2.83	2.90	2.96	2.70	2.43	2.44	2.47
	5	2.57	2.73	2.83	2.89	3.16	3.01	2.74	2.77	2.43	2.44
	4	2.71	2.72	2.90	2.73	2.90	3.13	2.75	2.15	1.83	2.07
	3	2.59	2.66	2.65	2.70	2.72	2.78	2.22	1.68	1.58	1.75
	2	2.68	2.76	2.67	2.77	2.58	3.03	2.55	2.27	2.06	2.28
	1	2.92	2.88	2.83	2.88	2.83	3.03	2.72	2.61	2.88	2.78
S7, Shallow and Partial Debonding	10	2.30	2.41	2.46	2.58	2.54	2.72	2.48	2.77	3.02	3.35
	9	2.58	2.46	2.49	2.36	2.61	2.70	2.54	2.60	2.60	2.91
	8	2.64	2.59	2.43	2.56	2.57	2.65	2.61	2.75	2.34	2.95
	7	2.64	2.59	2.69	2.55	2.76	2.72	2.66	2.83	2.77	3.23
	6	2.38	2.59	2.60	2.58	2.70	2.64	2.51	2.70	2.94	3.03
	5	2.41	2.31	2.49	2.61	2.53	2.61	2.37	2.59	2.73	3.03
	4	2.45	2.26	2.39	2.47	2.57	2.46	2.36	2.45	2.56	3.00
	3	2.48	2.49	2.26	2.43	2.36	2.43	2.40	2.16	2.17	2.60
	2	2.39	2.36	2.20	2.36	2.26	2.31	2.35	2.33	2.39	2.72
	1	2.10	2.32	2.26	2.19	2.25	2.40	2.64	2.66	2.99	3.04
S6, Intact	10	2.79	2.38	2.28	2.30	2.30	2.64	2.74	3.33	3.83	3.99
	9	2.54	2.31	2.22	2.32	2.49	2.81	2.61	3.27	3.62	4.11
	8	2.45	2.32	2.31	2.44	2.74	3.05	2.73	3.07	3.32	3.71
	7	2.21	2.36	2.38	2.58	2.97	3.01	2.64	3.04	3.40	3.48
	6	2.40	2.37	2.56	2.66	2.99	3.03	3.24	3.30	3.22	3.40
	5	2.69	2.65	2.66	2.68	2.89	3.26	2.89	3.41	3.32	3.37
	4	2.92	2.83	2.60	2.78	2.87	2.83	2.96	2.81	3.29	3.21
	3	2.92	2.97	2.85	2.79	2.88	3.07	2.62	2.84	2.99	3.15
	2	2.63	2.82	2.76	2.66	2.90	3.00	3.08	3.28	3.27	3.68
	1	2.33	2.61	2.86	2.81	2.71	2.91	3.05	3.71	4.02	4.12

Table E.11 Contd. – FFT Ratios of Impulse Response on Small Scale Study. Fine Mix and

Transition (Hot Weather)

	15	2.02	2.31	2.33	2.32	2.32	2.44	2.61	2.99	3.22	3.16
	14	1.90	2.18	2.14	2.36	2.23	2.25	2.51	2.80	3.37	3.37
	13	1.87	2.04	2.06	2.10	2.27	2.20	2.44	2.80	3.26	3.16
	12	2.00	2.00	2.08	2.09	2.19	2.31	2.45	2.74	3.02	3.16
	11	1.95	1.92	1.93	1.99	2.06	2.09	2.22	2.50	3.03	2.91
	10	1.91	1.88	1.87	1.93	1.98	2.11	2.24	2.50	2.94	2.88
TRANSITION	**9**	1.79	1.88	2.03	2.05	2.01	2.09	2.31	2.40	2.82	3.02
	8	1.78	2.12	2.19	2.10	1.91	1.50	1.46	1.32	1.89	1.61
	7	2.03	2.23	2.40	2.16	1.74	0.95	0.72	1.02	1.45	1.47
	6	2.30	2.47	2.39	2.12	1.63	0.73	0.77	1.09	1.47	1.50
	5	2.55	2.71	2.57	2.28	1.79	1.07	0.84	0.74	1.04	1.28
	4	2.66	3.08	2.86	2.54	2.38	2.02	2.46	2.65	2.46	2.75
	3	2.78	3.27	3.15	3.00	2.93	3.24	3.66	3.86	3.75	3.43
	2	2.56	3.11	3.20	3.24	3.19	3.41	3.97	3.89	3.68	3.26
	1	2.58	3.20	3.18	2.99	3.07	3.57	3.86	4.24	3.80	3.10

Table E.12 – FFT Ratios of Impulse Response on Small Scale Study. Coarse Mix (Hot Weather)

Section	Point	Impulse Response FFT Ratios (Load/geophone)									
		Line 1	Line 2	Line 3	Line 4	Line 5	Line 6	Line 7	Line 8	Line 9	Line 10
S5, Deep and Full Debonding	10	2.02	2.31	2.33	2.32	2.32	2.44	2.61	2.99	3.22	3.16
	9	1.90	2.18	2.14	2.36	2.23	2.25	2.51	2.80	3.37	3.37
	8	1.87	2.04	2.06	2.10	2.27	2.20	2.44	2.80	3.26	3.16
	7	2.00	2.00	2.08	2.09	2.19	2.31	2.45	2.74	3.02	3.16
	6	1.95	1.92	1.93	1.99	2.06	2.09	2.22	2.50	3.03	2.91
	5	1.91	1.88	1.87	1.93	1.98	2.11	2.24	2.50	2.94	2.88
	4	1.79	1.88	2.03	2.05	2.01	2.09	2.31	2.40	2.82	3.02
	3	1.78	2.12	2.19	2.10	1.91	1.50	1.46	1.32	1.89	1.61
	2	2.03	2.23	2.40	2.16	1.74	0.95	0.72	1.02	1.45	1.47
	1	2.30	2.47	2.39	2.12	1.63	0.73	0.77	1.09	1.47	1.50
S4, Deep and Partial Debonding	10	2.55	2.71	2.57	2.28	1.79	1.07	0.84	0.74	1.04	1.28
	9	2.66	3.08	2.86	2.54	2.38	2.02	2.46	2.65	2.46	2.75
	8	2.78	3.27	3.15	3.00	2.93	3.24	3.66	3.86	3.75	3.43
	7	2.56	3.11	3.20	3.24	3.19	3.41	3.97	3.89	3.68	3.26
	6	2.58	3.20	3.18	2.99	3.07	3.57	3.86	4.24	3.80	3.10
	5	2.02	2.31	2.33	2.32	2.32	2.44	2.61	2.99	3.22	3.16
	4	1.90	2.18	2.14	2.36	2.23	2.25	2.51	2.80	3.37	3.37
	3	1.87	2.04	2.06	2.10	2.27	2.20	2.44	2.80	3.26	3.16
	2	2.00	2.00	2.08	2.09	2.19	2.31	2.45	2.74	3.02	3.16
	1	1.95	1.92	1.93	1.99	2.06	2.09	2.22	2.50	3.03	2.91
S3, Shallow and Full Debonding	10	1.91	1.88	1.87	1.93	1.98	2.11	2.24	2.50	2.94	2.88
	9	1.79	1.88	2.03	2.05	2.01	2.09	2.31	2.40	2.82	3.02
	8	1.78	2.12	2.19	2.10	1.91	1.50	1.46	1.32	1.89	1.61
	7	2.03	2.23	2.40	2.16	1.74	0.95	0.72	1.02	1.45	1.47
	6	2.30	2.47	2.39	2.12	1.63	0.73	0.77	1.09	1.47	1.50
	5	2.55	2.71	2.57	2.28	1.79	1.07	0.84	0.74	1.04	1.28
	4	2.66	3.08	2.86	2.54	2.38	2.02	2.46	2.65	2.46	2.75
	3	2.78	3.27	3.15	3.00	2.93	3.24	3.66	3.86	3.75	3.43
	2	2.56	3.11	3.20	3.24	3.19	3.41	3.97	3.89	3.68	3.26
	1	2.58	3.20	3.18	2.99	3.07	3.57	3.86	4.24	3.80	3.10
S2, Shallow and Partial Debonding	10	2.02	2.31	2.33	2.32	2.32	2.44	2.61	2.99	3.22	3.16
	9	1.90	2.18	2.14	2.36	2.23	2.25	2.51	2.80	3.37	3.37
	8	1.87	2.04	2.06	2.10	2.27	2.20	2.44	2.80	3.26	3.16
	7	2.00	2.00	2.08	2.09	2.19	2.31	2.45	2.74	3.02	3.16
	6	1.95	1.92	1.93	1.99	2.06	2.09	2.22	2.50	3.03	2.91
	5	1.91	1.88	1.87	1.93	1.98	2.11	2.24	2.50	2.94	2.88
	4	1.79	1.88	2.03	2.05	2.01	2.09	2.31	2.40	2.82	3.02
	3	1.78	2.12	2.19	2.10	1.91	1.50	1.46	1.32	1.89	1.61
	2	2.03	2.23	2.40	2.16	1.74	0.95	0.72	1.02	1.45	1.47
	1	2.30	2.47	2.39	2.12	1.63	0.73	0.77	1.09	1.47	1.50
S1, Intact	10	2.55	2.71	2.57	2.28	1.79	1.07	0.84	0.74	1.04	1.28
	9	2.66	3.08	2.86	2.54	2.38	2.02	2.46	2.65	2.46	2.75
	8	2.78	3.27	3.15	3.00	2.93	3.24	3.66	3.86	3.75	3.43
	7	2.56	3.11	3.20	3.24	3.19	3.41	3.97	3.89	3.68	3.26
	6	2.58	3.20	3.18	2.99	3.07	3.57	3.86	4.24	3.80	3.10
	5	2.02	2.31	2.33	2.32	2.32	2.44	2.61	2.99	3.22	3.16
	4	1.90	2.18	2.14	2.36	2.23	2.25	2.51	2.80	3.37	3.37
	3	1.87	2.04	2.06	2.10	2.27	2.20	2.44	2.80	3.26	3.16
	2	2.00	2.00	2.08	2.09	2.19	2.31	2.45	2.74	3.02	3.16
	1	1.95	1.92	1.93	1.99	2.06	2.09	2.22	2.50	3.03	2.91

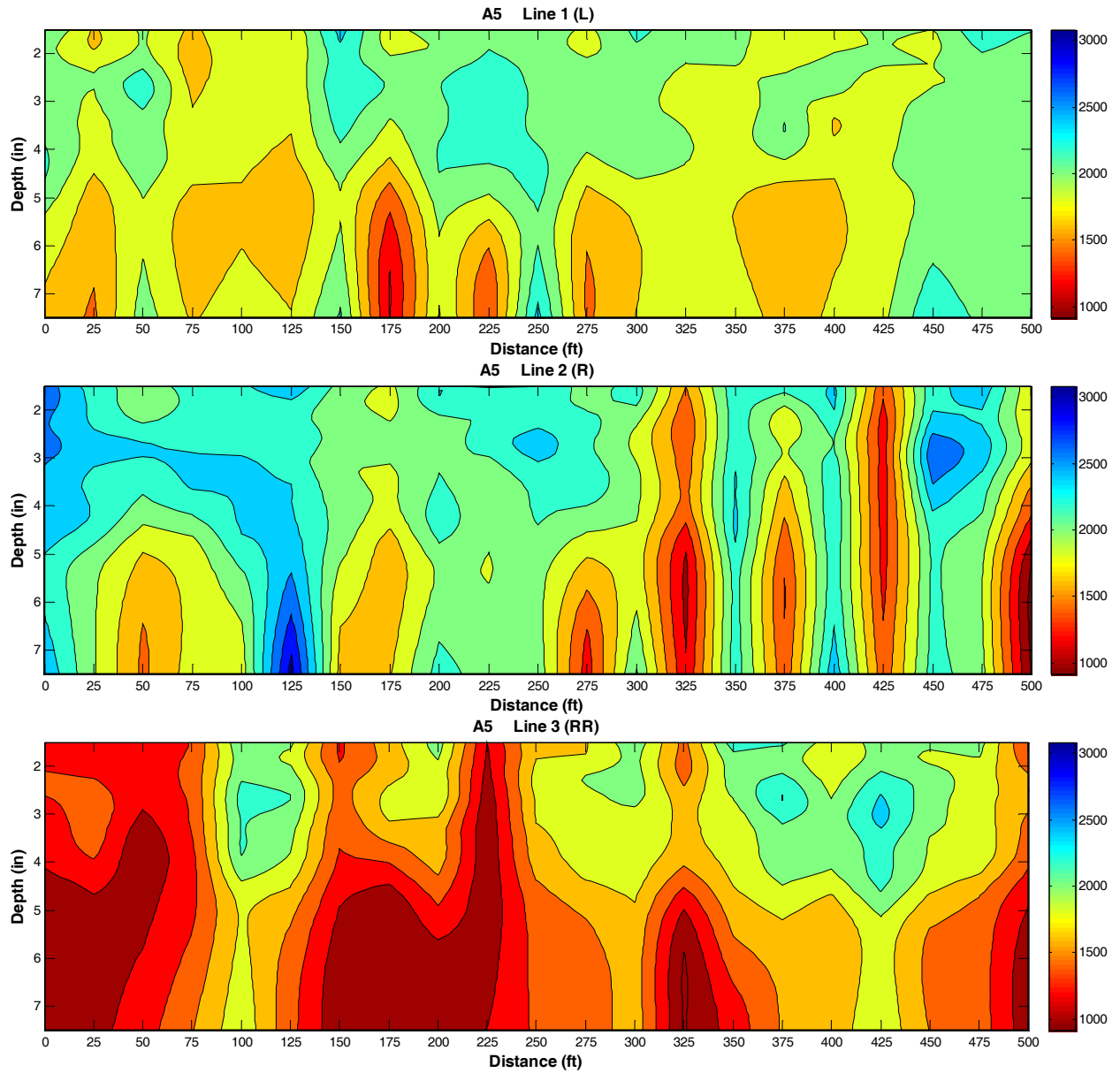# APPENDIX F

ADDITIONAL NDT RESULTS ON PORTLAND AND BOSTON INTERNATIONAL

AIRPORTS

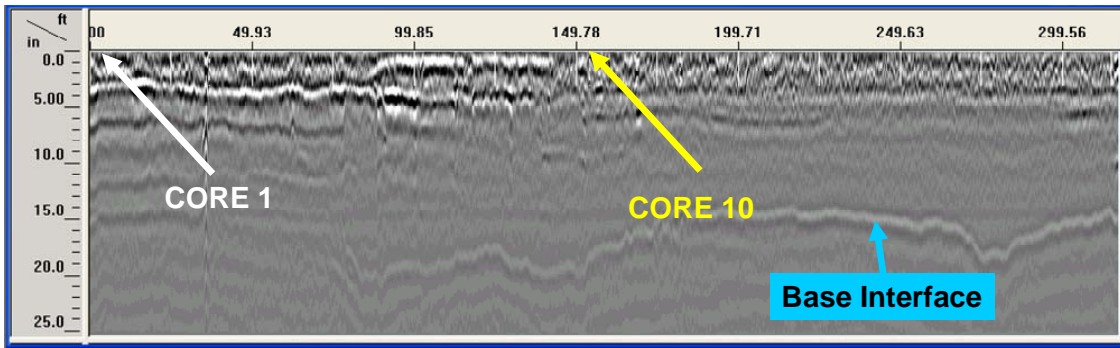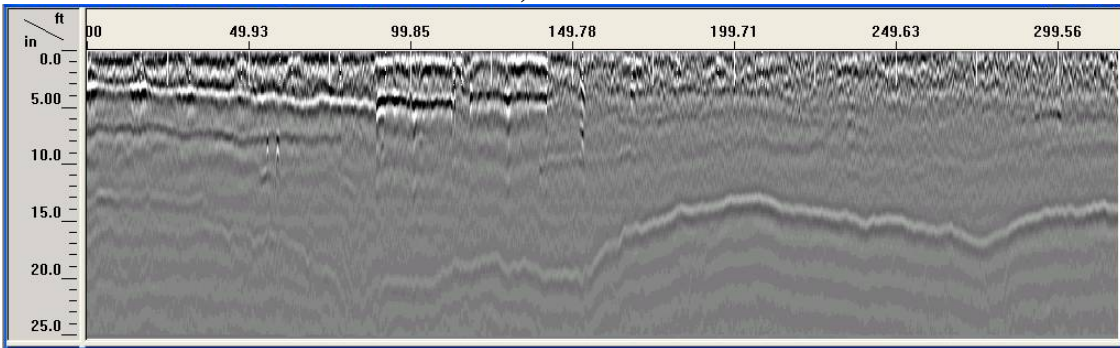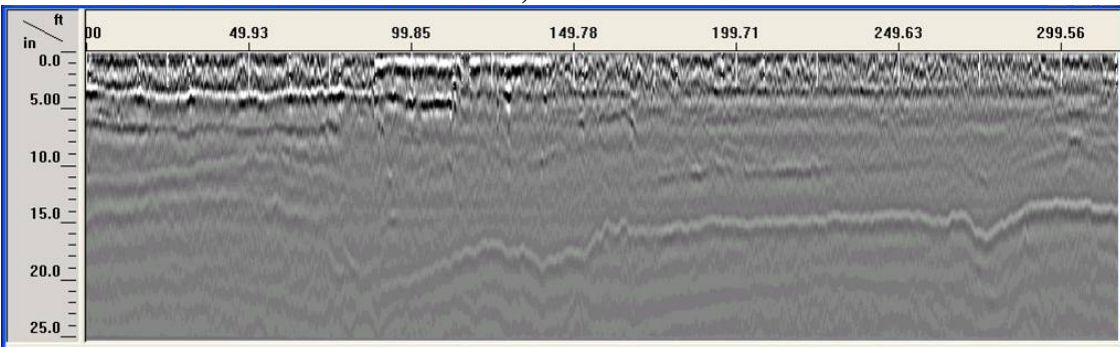**Figure F.1 – Dispersion Curves for Section A5**

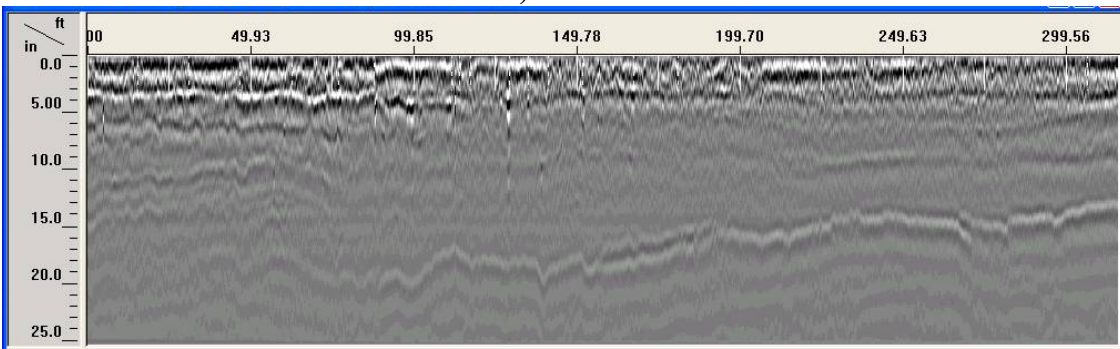**a) Line 1**

b) Line 2

c) Line 3

d) Line 4

Figure F.2 – Post-processed GPR Linescans on Section C6

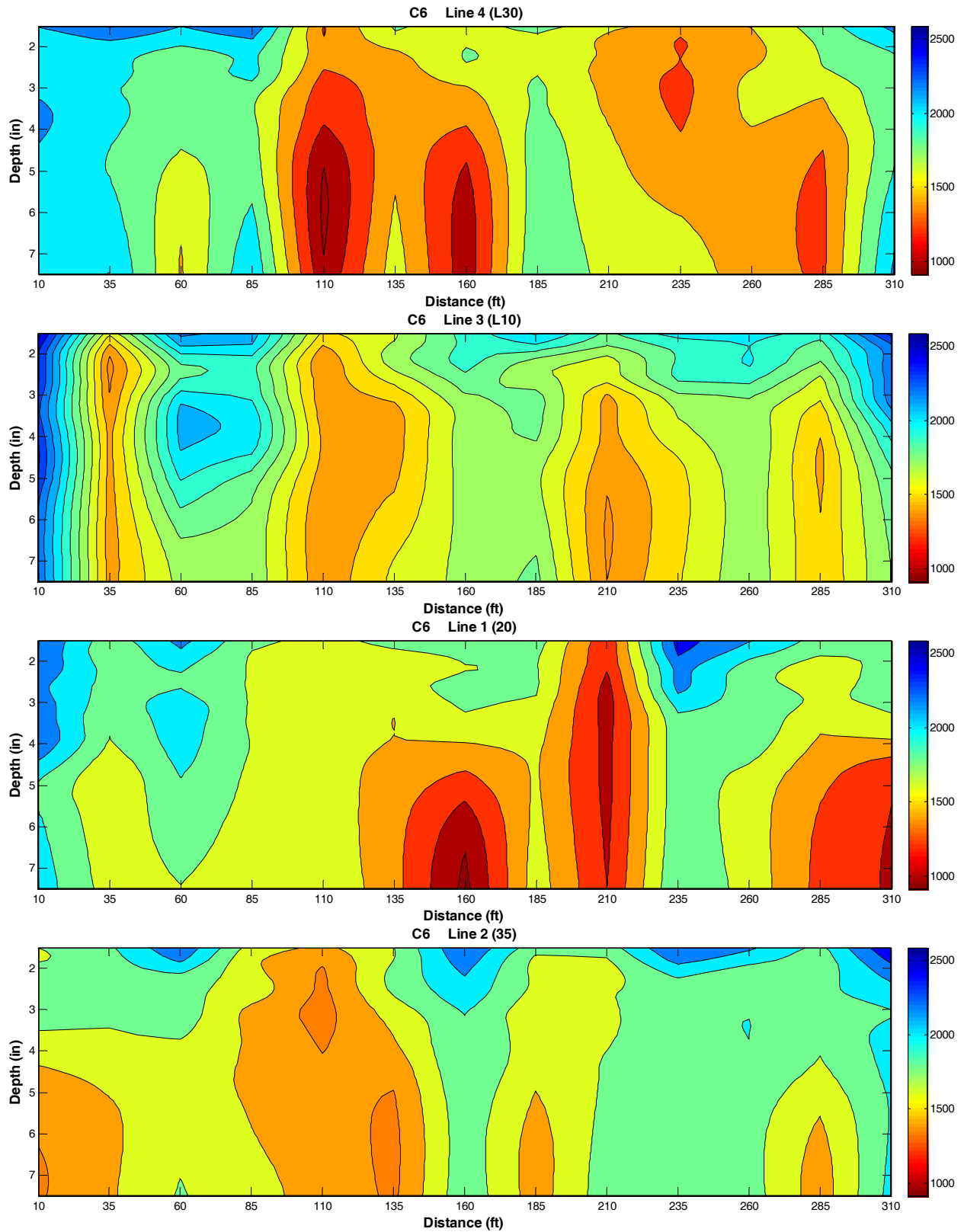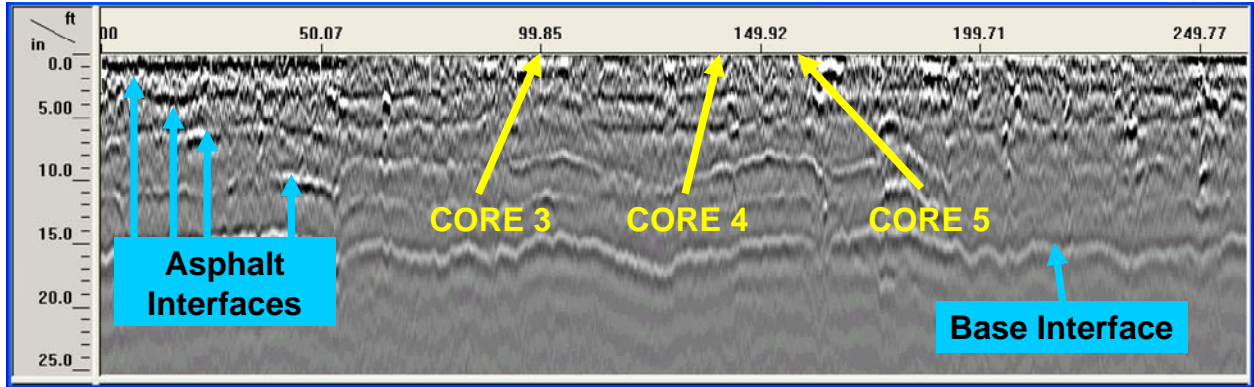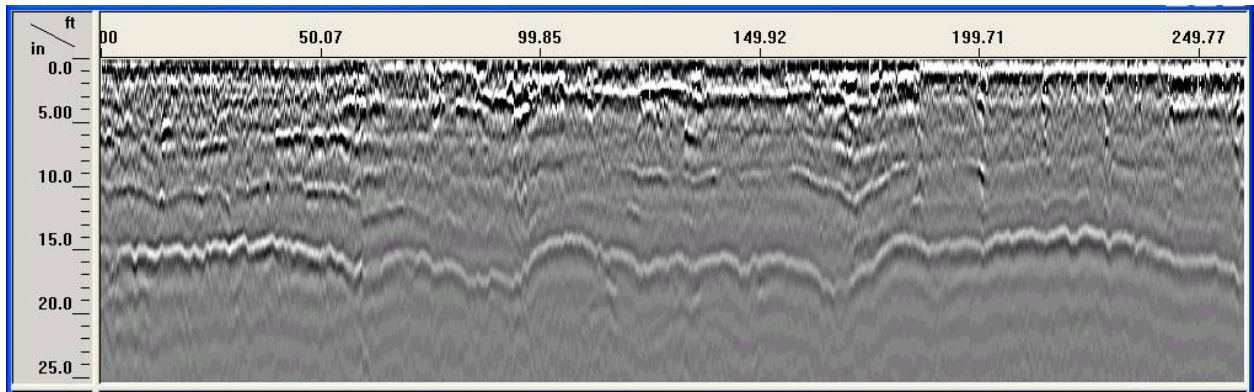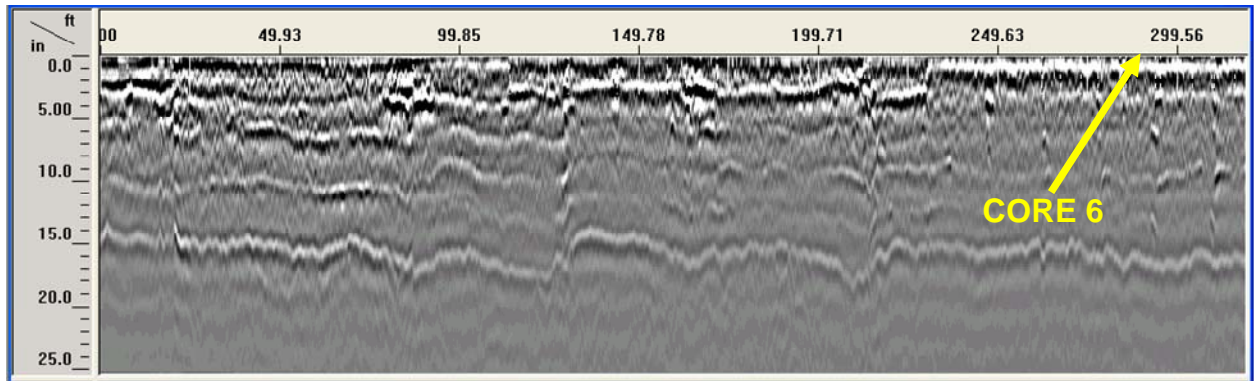**Figure F.3 – Dispersion Curves for Section C6**

a) Line 1

b) Line 2

c) Line 3

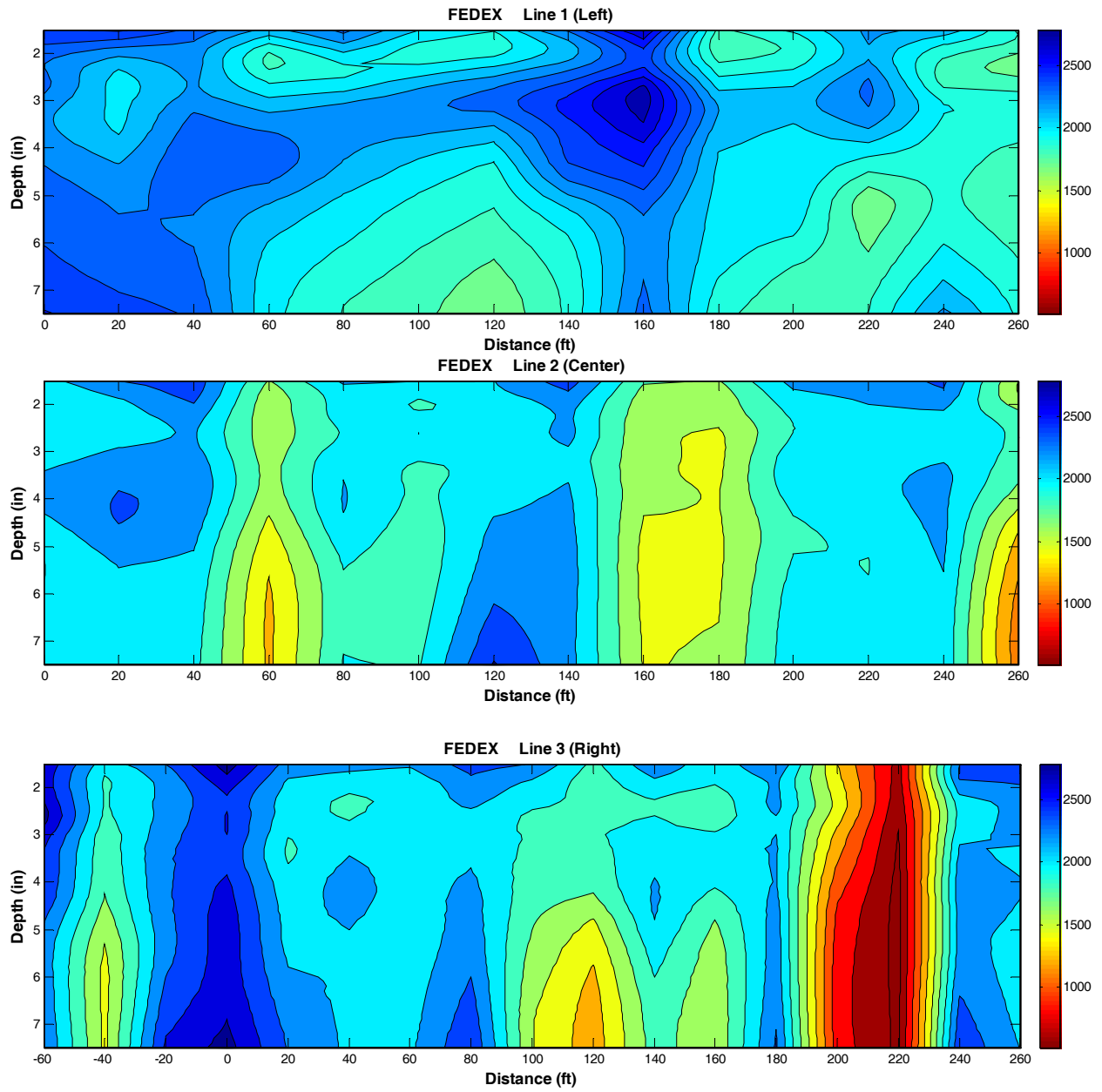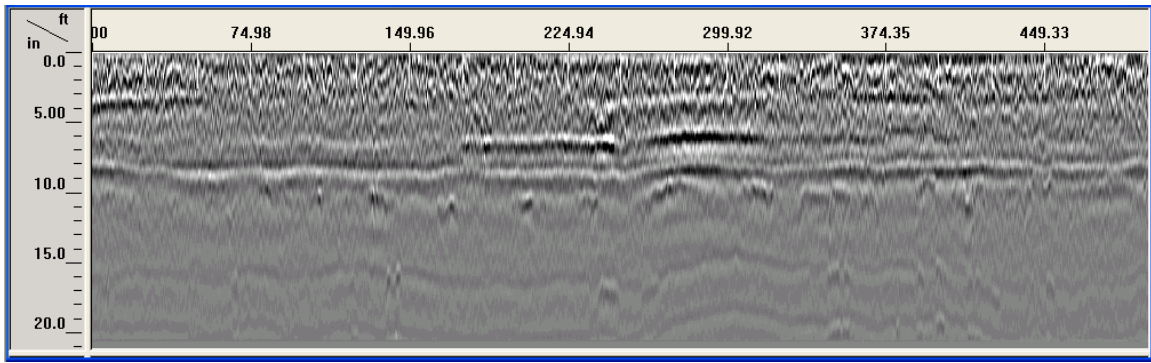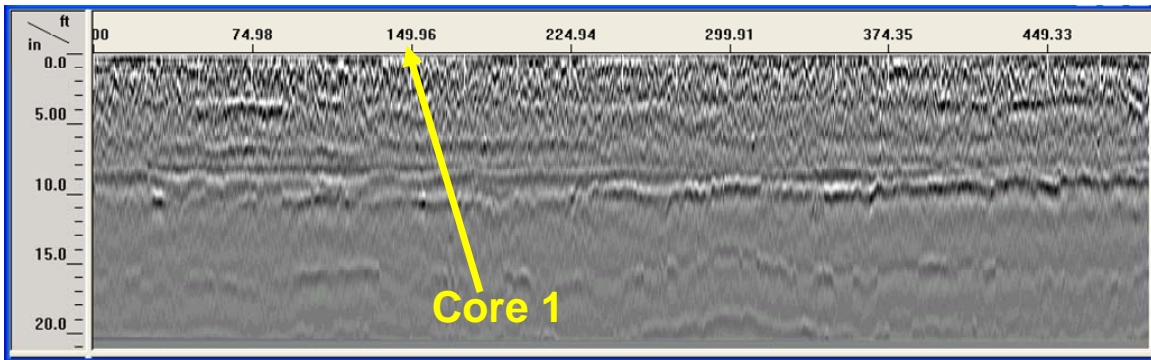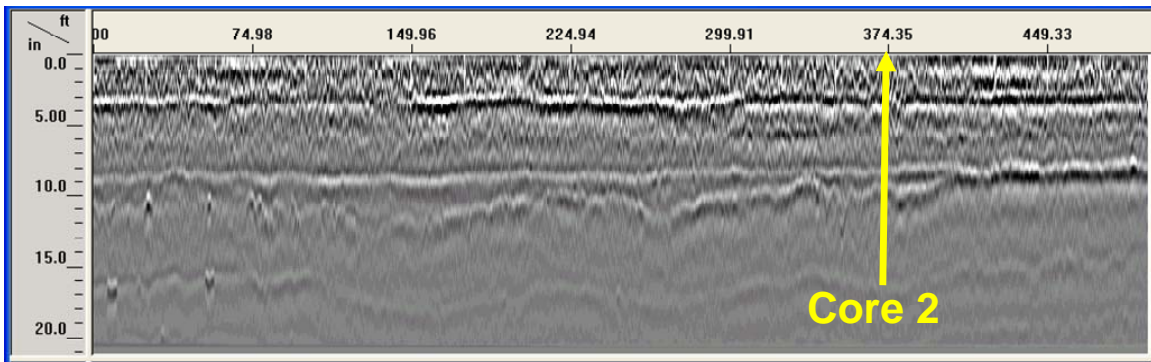**Figure F.4 – Post-processed GPR Linescans on South Ramp Section**

Figure F.5 – Dispersion Curves for South Ramp Section

a) Line 1

b) Line 2

c) Line 3

Figure F.6 – Post-processed GPR Linescans on Section 1 of E4
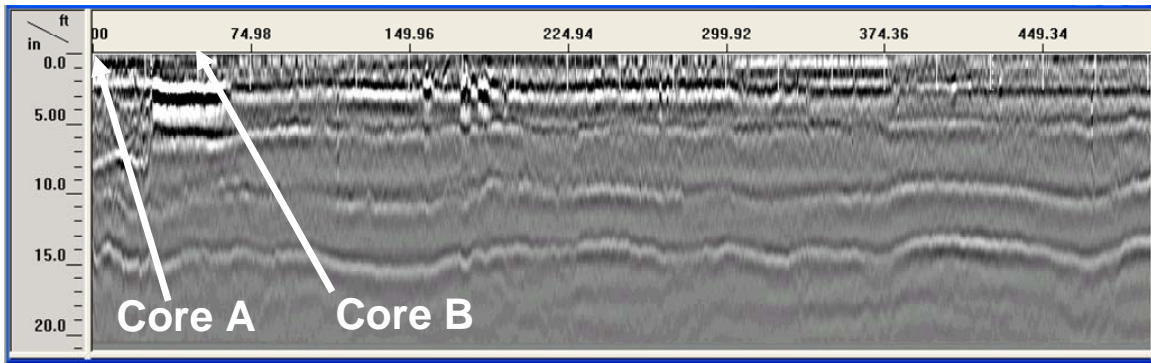
a) Line 1
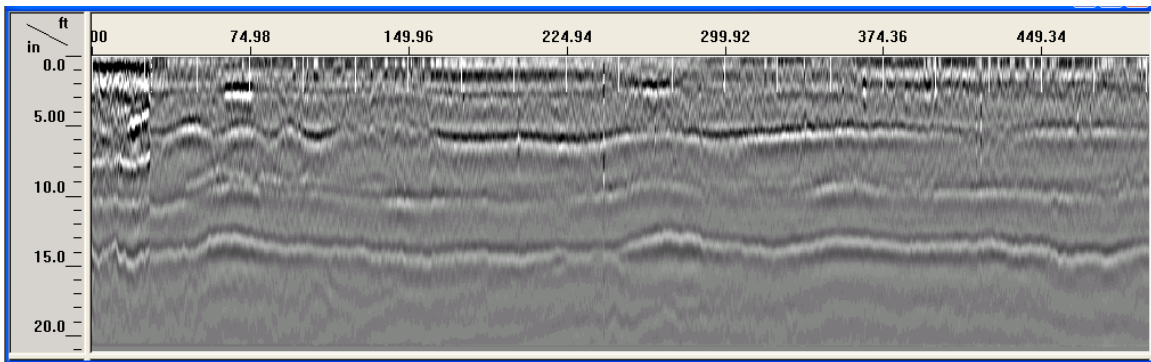
b) Line 2
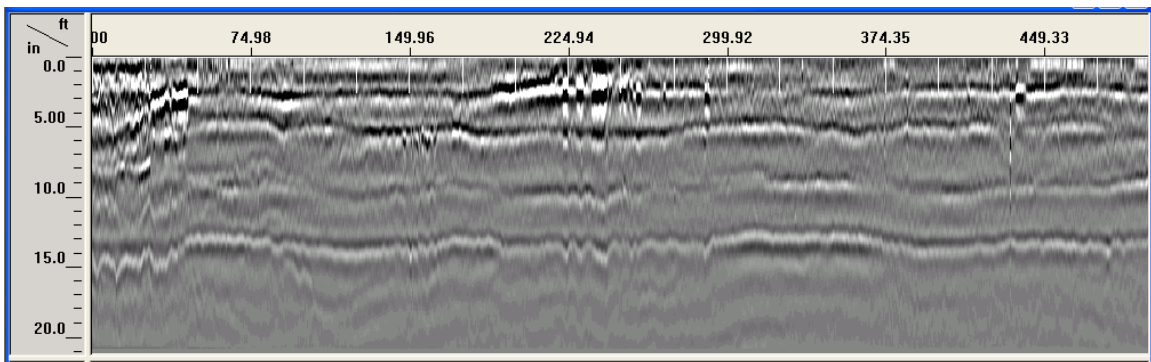
c) Line 3

Figure F.7 – Post-processed GPR Linescans on Section 2 of E4
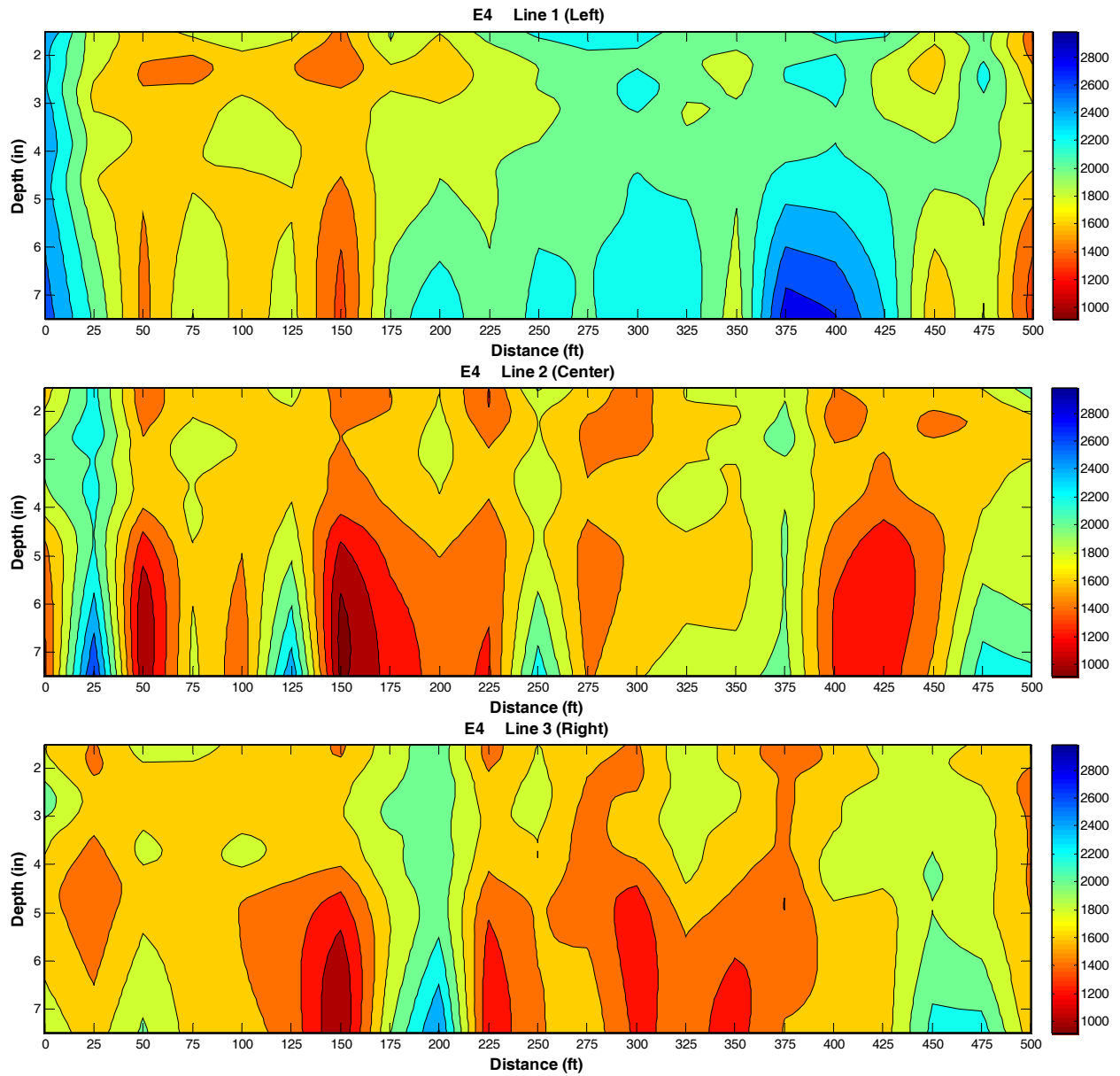
Figure F.8 – Dispersion Curves for Section 1 of E4
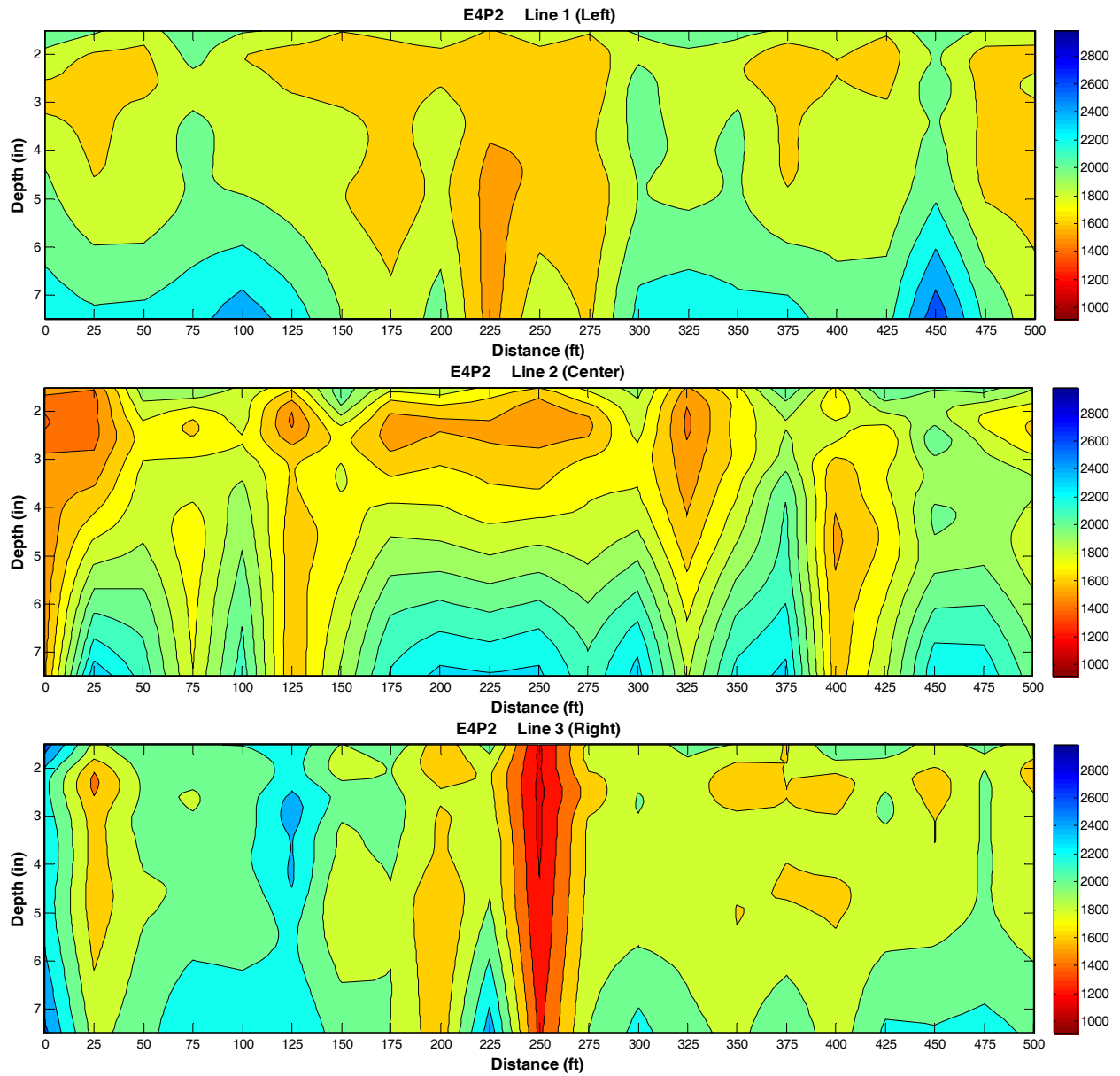
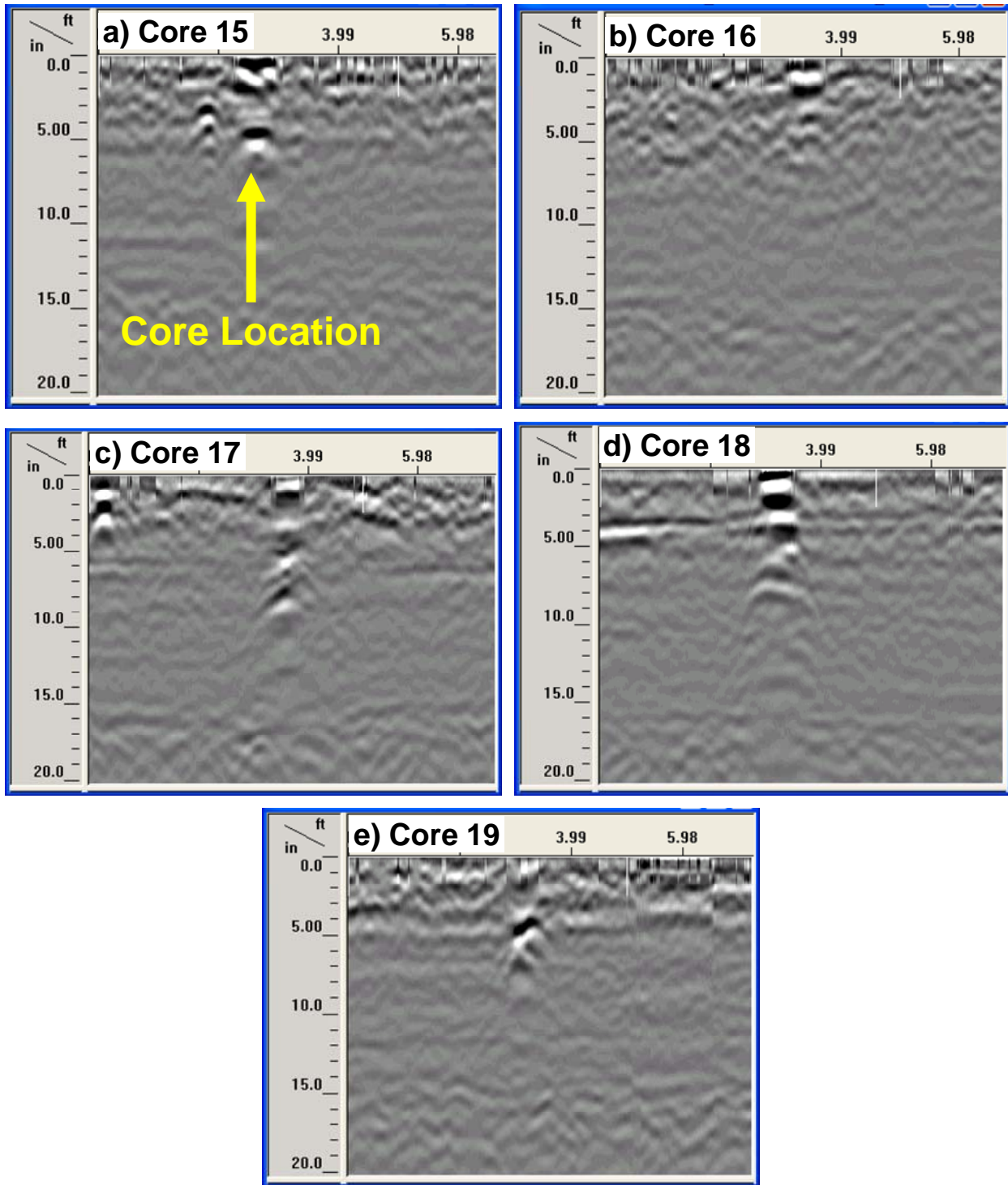**Figure F.9 – Dispersion Curves for Section 2 of E4**

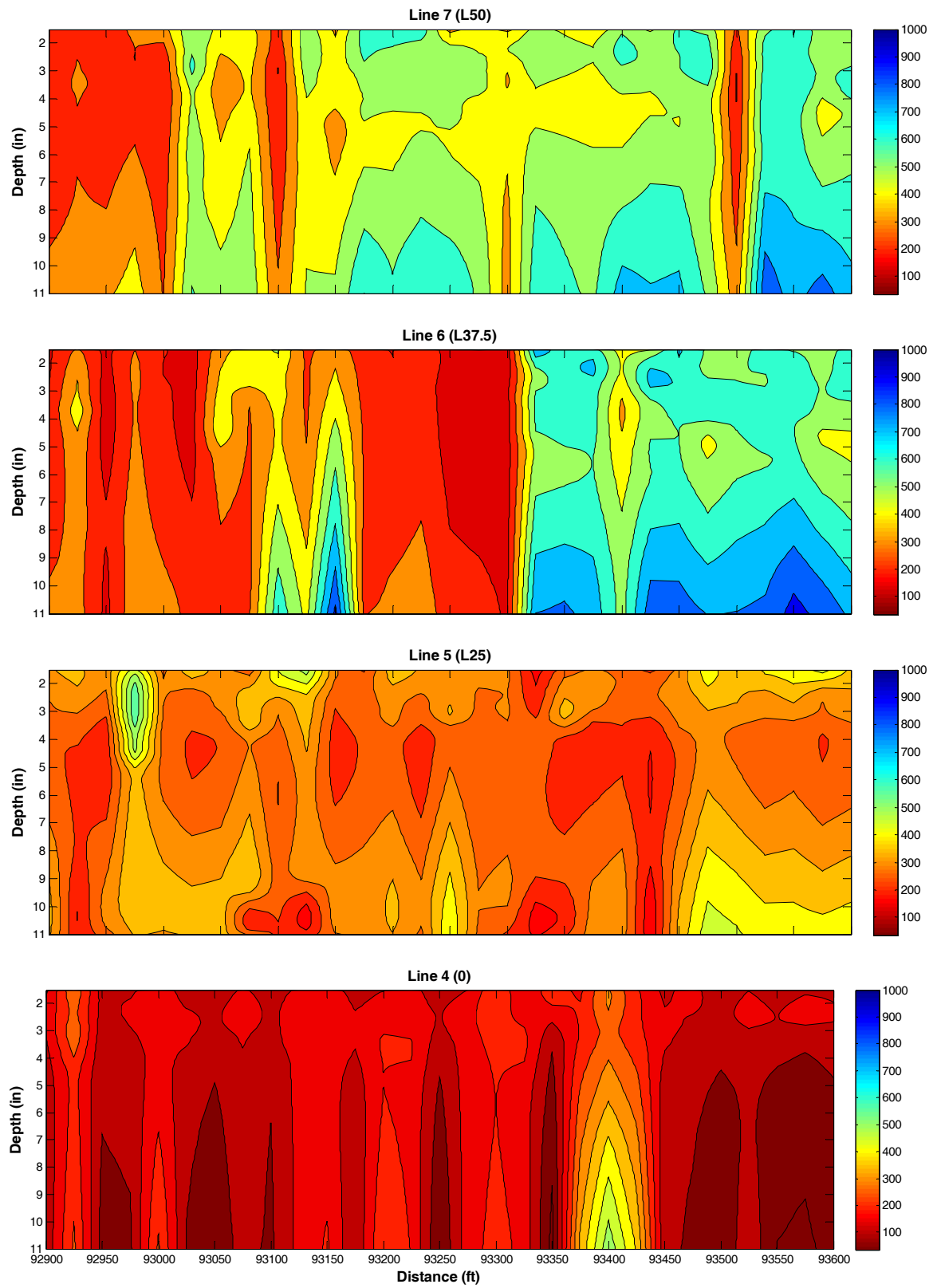**Figure F.10 – Post-processed GPR Linescans on Selected Cores of Section 1**
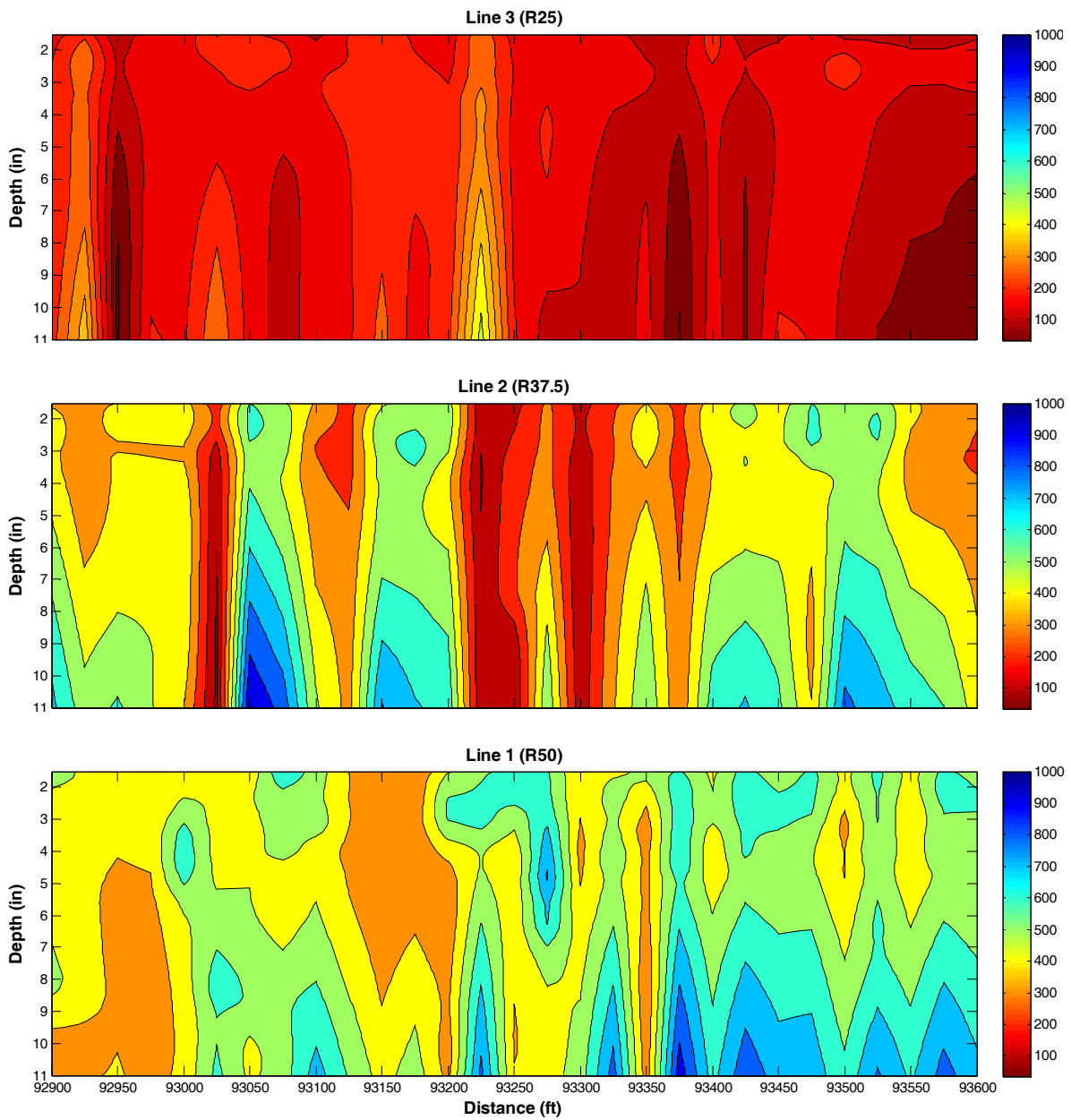
Figure F.11 – Dispersion Curves for Section 1

Figure F.11 Contd. – Dispersion Curves for Section 1

COMPLETE NDT RESULTS FOR DETECTABILITY STUDY

Table G.1 – Probability of Success of NDT Methods to Detect Different Levels and Sizes of Delamination

NDT Device	HMA Type	Area Size (ft)	Cool Weather Debonding Depth and Type				Hot Weather Debonding Depth and Type			
			Deep (5 in.)		Shallow (2.5 in.)		Deep (5 in.)		Shallow (2.5 in.)	
			Full	Partial	Full	Partial	Full	Partial	Full	Partial
PSPA	Fine Mix	4 by 9	43%	60%	88%	58%	48%	28%	93%	27%
		2 by 2	0%	17%	67%	33%	8%	33%	67%	33%
		1 by 1	0%	50%	0%	0%	0%	0%	0%	0%
		0.5 by 0.5	0%	0%	50%	0%	0%	50%	25%	0%
	Coarse Mix	4 by 9	18%	37%	90%	65%	3%	18%	98%	72%
		2 by 2	8%	17%	67%	0%	0%	33%	83%	33%
		1 by 1	25%	100%	50%	50%	0%	0%	75%	0%
		0.5 by 0.5	0%	100%	0%	0%	0%	0%	0%	0%
IR	Fine Mix	4 by 9	50%	72%	95%	30%	80%	85%	78%	20%
		2 by 2	0%	33%	92%	0%	0%	0%	83%	0%
		1 by 1	0%	0%	0%	0%	0%	0%	0%	0%
		0.5 by 0.5	0%	50%	0%	0%	0%	0%	0%	50%
	Coarse Mix	4 by 9	40%	52%	100%	48%	10%	42%	100%	40%
		2 by 2	58%	0%	8%	0%	92%	17%	50%	0%
		1 by 1	0%	50%	0%	0%	0%	50%	0%	0%
		0.5 by 0.5	0%	0%	0%	0%	0%	0%	0%	0%
FWD (Deflections)	Fine Mix	4 by 9	0%	13%	100%	72%	75%	59%	100%	0%
		2 by 2	0%	0%	0%	0%	0%	100%	100%	0%
		1 by 1	0%	0%	0%	0%	0%	100%	100%	100%
		0.5 by 0.5								
	Coarse Mix	4 by 9	0%	19%	100%	66%	0%	19%	100%	31%
		2 by 2	0%	0%	0%	0%	0%	0%	100%	0%
		1 by 1	0%	0%	0%	0%	0%	0%	100%	0%
		0.5 by 0.5								
FWD (Modulus)	Fine Mix	4 by 9	75%	41%	100%	38%	75%	59%	67%	0%
		2 by 2	0%	100%	50%	0%	0%	0%	0%	0%
		1 by 1	50%	0%	0%	0%	0%	0%	0%	100%
		0.5 by 0.5								
	Coarse Mix	4 by 9	17%	41%	100%	59%	0%	19%	100%	31%
		2 by 2	100%	100%	0%	100%	0%	0%	100%	0%
		1 by 1	0%	0%	50%	0%	0%	0%	100%	0%
		0.5 by 0.5								
GPR	Fine Mix	4 by 9					42%	36%	44%	34%
		2 by 2					0%	67%	92%	75%
		1 by 1					75%	0%	100%	50%
		0.5 by 0.5					50%	0%	50%	0%
	Coarse Mix	4 by 9					6%	9%	72%	23%
		2 by 2					33%	8%	8%	17%
		1 by 1					50%	0%	50%	0%
		0.5 by 0.5					25%	50%	25%	0%

REFERENCES

Acoustic Control Systems, www.acsys.ru/eng

Al Hakim, B., Al Nageim, H., Pountney, D., and Lesley, L. (1997). ''The development of an improved pavement backcalculation.'' Proceedings, 1st International Conference on Rehabilitation and Development of Civil Engineering Infrastructure Systems, Lebanon.

Al Hakim, B., Armitage, R., and Thom, N. H. (1998). ''Pavement assessment including bonding condition: case studies.'' Proceedings, 5th International Conference on Bearing Capacity of Roads and Airfields, University of Trondheim, Trondheim, Norway, 1, 439–448.

Al Hakim, B., Cheung, L. W., and Armitage, R., (2000). ''Use of FWD Data for Prediction of Bonding between Pavement Layers.'' International Journal of Pavement Engineering, 2000. Vol. 1(1), pp. 49-59.

Armitage, R. J., Kruntcheva, M. R., and Willett, M. R. (2000). ''Trials of the Portable Seismic Pavement Analyzer (PSPA).'' Report Prepared for Highways Agency, Pavement Engineering Group, Scott Wilson Pavement Engineering, Nottingham, U.K.

Carino, N.J., 2001, "The Impact-Echo Method: an Overview." Proceedings of the 2001 Structures Congress & Exposition, May 21-23, 2001,Washington, D.C., American Society of Civil Engineers, Reston, Virginia (2001), 18 p.

CTL Group. Impulse Response Testing. www.ctlgroup.com

Delatte, N., Chen, S. E. and Jackson, N. M. "UTW and SASW for General Aviation Airport Pavement Rehabilitation," 2002 Federal Aviation Administration Technology Transfer Conference, Atlantic City, N.J., May 7, 2002.

Ganji, V. (1998). ''Preliminary trials of the Portable Seismic Pavement Analyzer (PSPA).'' Job No. E298-1, Scott Wilson Pavement Engineering, Nottingham, U.K.

Garbacz, A. and Garboczi, E. J. "Ultrasonic Evaluation Methods Applicable to Polymer Concrete Composites." NISTIR 6975; 73 p. April 2003. National Institute of Standards and Technology, Gaithersburg, MD 20899.

GBG Australia. Non Destructive Techniques for Sub Surface Profiling of Pavement Structures.

Gomba, S.M. (2004) "Evaluation of interlayer bonding in hot mix asphalt pavements." Master Thesis. Rowan University, Glassboro, New Jersey.

Hammons, M., I., Von Quintus, H., Maser, K., and Nazarian, S. (2005) "Detection of stripping in hot mix asphalt." Applied Research Associates Project Number 16355, prepared for: Office of Materials and Research, Georgia Department of Transportation.

Kruntcheva, M. R., Collop, A. C., and Thom, N. H. (2000). ''The Portable Seismic Pavement Analyzer: laboratory trials.'' Project Report PGR 2000-02, University of Nottingham, U.K.

Kruntcheva, M., R., Collop, A., C. and Thom, N., H. (2004) "Feasibility of assessing bond condition of asphalt concrete layers with dynamic nondestructive testing." Journal of Transportation Engineering, Vol. 130, No. 4.

Kruntcheva, M. R., Collop, A. C., and Thom, N. H. (2005). "Effect of Bond Condition on Flexible Pavement Performance." Journal of Transportation Engineering, Volume 131, Issue 11, pp. 880-888, November 2005.

Lepert, P., Poilane, J. P., and Villard-Bats, M. (1992). "Evaluation of various field measurement techniques for the assessment of pavement interface condition." Proceedings, 7th International Conference on Asphalt Pavements, Vol. 3, 224–237.

Lin, J.M. and Sansalone, M.J., 1996, "Impact-Echo Studies of Interfacial Bond Quality in Concrete: Part I-Effects of Unbonded Fraction of Area," ACI Materials Journal, Vol. 93, No. 3, May-June, pp. 223- 232.

Maser K. R. (1996), "Condition assessment of transportation infrastructure using ground-penetrating radar", ASCE Journal of Infrastructure Systems, pp. 94-101

Maser K. R., Holland, T. J., and Roberts, R. (2002) "Nondestructive measurement of layer thickness on newly constructed asphalt pavement." Proceedings of the Pavement Evaluation Conference, Roanoke, VA.

Medina, R. and Garrido, M. Improving Impact-echo Method by Using Cross-spectral Density. Journal of Sound and Vibration, Volume 304, Issue 3-5, p. 769-778, July 2007.

Moropoulou, A., Avdelidis, N., P., Koui, M., and Kakaras, K. (2002) "Flaw detection and evaluation of airport pavements by means of infrared thermography." http://www.flirthermography.com/media/Detection_Evaluation_Airport_Paving.pdf

Nazarian, S., Baker, M. R., and Crain, K. (1993). ''Developing and Testing a Seismic Pavement Analyzer.'' Technical Report SHRP-H-375, Strategic Highway Research Program, Washington, D.C.

Nazarian, S., M. Baker, and K. Crain. 1997. "Assessing Quality of Concrete with Wave Propagation Techniques," Materials Journal, ACI, Farmington Hills, MI, Vol. 94 (4) 296-306

Sangiorgi, C., Collop, A., C. and Thom, N., H. (2003) "A nondestructive impulse hammer for evaluating the bond between asphalt layers in a road pavement." Non-Destructive Testing in Civil Engineering, International Symposium, Liverpool, UK.

Sansalone, M. and N. J Carino. 1986. "Impact-Echo: A Method for Flaw Detection in Concrete Using Transient Stress Waves," Report NBSIR 86-3452, Gaithersburg, MD.

Sebesta S., and Scullion, T. (2002), "Using infrared imaging and ground-penetrating radar to detect segregation in hot-mix overlays", Report No. 4126-1, Texas Transportation Institute.

Smith, S., S., Scullion, T. Development of Ground-Penetrating Radar Equipment for Detecting Pavement Condition for Preventive Maintenance. SHRP-H-672. Strategic Highway Research Program. National Research Council Washington, DC 1993.

Stroup-Gardiner M. and Brown E.R. (2000), "Segregation in hot-mix asphalt pavements", NCHRP Report 441, TRB, National Research Council, Washington, D.C.

Tsubokawa, Y., Mizukami, J., Esaki, T., and Hayano, K. (2007) "Study on infrared thermographic inspection of de-bonded layer of airport flexible pavement." FAA Worldwide Airport Technology Transfer Conference. Atlantic City, New Jersey.